This is to certify that the
dissertation entitled

DISLOCATION GENERATION AND MOTION IN B2 NIAL SINGLE CRYSTALS

presented by

BIMAN GHOSH

has been accepted towards fulfillment
of the requirements for the

Doctoral degree in Chemical Engineering and Materials Science

Major Professor's Signature

December 18, 2003

Date

# DISLOCATION GENERATION AND MOTION IN B2 NIAL SINGLE CRYSTALS

By

Biman Ghosh

A DISSERTATION

Submitted to
Michigan State University
in partial fulfillments of the requirements
for the degree of

DOCTOR OF PHILOSOPHY

Department of Chemical Engineering and Materials Science

2003

DISLOCATIO

In order t

dislocation beha

studied followin

electron microsc

dislocation subs

changes in the c

observed in all t

generated disloc

foil edge and fro

in the high pur

commercially pu

in contrast to th

uniform. The

explained in ter

thermal history

commercially p

*in-situ* straining.

In the high purit

## ABSTRACT

DISLOCATION GENERATION AND MOTION IN B2 NIAL SINGLE CRYSTALS

By

Biman Ghosh

In order to understand the effects of composition, orientation, and cooling rate on dislocation behavior in NiAl, high and commercial purity NiAl single crystals have been studied following thermal treatments, deformations, and *in-situ* straining in transmission electron microscopy. It was observed that the yield strength and post deformation dislocation substructure of the commercial purity alloy were impacted more by the changes in the cooling rate than the high purity alloy. Dislocation motion was readily observed in all the samples. The pre-existing dislocations were sessile, while the newly generated dislocations glided in slip bands. Dislocations were generated both from the foil edge and from the foil interior. Cross-slip of mobile dislocations was often observed in the high purity alloy whereas slip was found to be much more planar in the commercially pure alloy. Dislocations moved by rapid jumps in the high purity material, in contrast to the commercially pure material where movement was much slower and uniform. The differences in the mechanical properties and dislocation behaviors are explained in terms of static and dynamic strain aging. Despite the well-known effect of thermal history on the mechanical behavior of NiAl, variations in cooling rate of the commercially pure material did not appear to influence the dislocation behavior during *in-situ* straining. In all cases <001> and <110> dislocations were observed to be mobile. In the high purity material mobility of <111> dislocations was also observed.

Dedicated to my parents, Mrs. Anjali and Mr. Benoy Krishna Ghosh.

I would
without whose g
complete this w
Special r
assistance, and
Thomas Bieler,
suggestions and
Naval Research
gratefully ackno
I would
Evandale, OH
providing the N
Pelazolo and the
graduate studen
program.
I would
encouragement a
and wife, Surita
always there by

## ACKNOWLEDGEMENTS

I would like to thank everyone who stood by my side in this entire journey and without whose guidance, help, and support it was not possible for me to stay focused and complete this work.

Special mention to my mentor and advisor, Dr. Martin A. Crimp, for his guidance, assistance, and painstaking reviews to finish this dissertation. I would like to thank Dr. Thomas Bieler, Dr. Karen Klomparens, and Dr. David Grummon for their helpful suggestions and advice during this investigation. The financial support of the Office of Naval Research (Scientific Officer, Dr. George Yoder; Grant # 00014-94-1-0204) is gratefully acknowledged.

I would also like to thank Dr. Ram Darolia at General Electric Aircraft Engines, Evandale, OH and Dr. Vladimir Levit, University of Florida, Gainesville, FL for providing the NiAl single crystals used in this study. The technical assistance of Tom Pelazolo and the late Leo Zafransky is also acknowledged. Special thanks to my fellow graduate student, Boon-Chai Ng, for his assistance in running the image-simulation program.

I would like to thank my parents, Anjali and Benoy Krishna Ghosh, for their encouragement and support during this study. Lastly, I am grateful to my daughter, Bitan and wife, Surita for their help, support, and persistence in this long journey and to be always there by my side.

## TABLE OF CONTENTS

## LIST OF TABLES

## LIST OF FIGURES

Figure 16. Is
structure of co
tangles in (a) a
(c) an undeform

Figure 17. The
with $\bar{\mathbf{g}} = [011]$.

Figure 18. Hea
FC specimen; (a

Figure 19. Def
(a) brightfield a

Figure 20. Def
dislocations in (

Figure 21. Cor
of dislocations.
different operat
also seen to mo

Figure 22. Di
specimens: (a)

Figure 23. Ve
673 AC specir

Figure 24.
dislocations w
operative refle

Figure 25.
dislocations ir
condition appe
(d).

Figure 26. H
a) in different
beam heating.

Figure 27. Dis
dislocations in
direction in fig
present in the n
and (c). .....

Figure 28. It i
show such disl
very weak and
.....

Figure 29. Dis
for image simu

Figure 30. A
diffraction cond
diffraction cond

Figure 31. Dis
of events captur
a result of strai
edge. .....

Figure 31 (cont
and cross-past p
(e) and (f) reve
on dislocations.

Figure 31 (con
bands that prod
stay sessile thro

Figure 32. A r
exhibit tangles
few dipoles are

Figure 33. (a) F
edge of the foi
Images showing
trails indicating
between slip ba

Figure 34. Dis
The mobile disl
of the foil and s
slip-traces left in

Figure 35. I
commercially p
dislocation trail

Figure 36. Li
oriented NiAl: I

Figure 37. Pr
areas of the [0
straining. dislo
newly generate
ease (b) and (c)

Figure 38. Di
dislocations are
and seen at the
traces left in th
not present in (a

Figure 39. Se
oriented NiAl.
a slow and unif

Figure 40. Lo
[001] oriented N
sources takes pl

Figure 41. Co
the marked dire
surface. (b) A c
arrays of pre-ex
Loops and debri

Figure 42. Se
characterizing t
subsequent slip

Figure 43. Dis
Sequence of im
relative differen

Figure 44. Se
oriented NiAl.
dislocations. N
marked in figur
during exposure

Figure 45. Co
dislocations be
dislocations sh

Figure 46. Mul
sources in co
dynamically w
the applied stre
to expand agai
regretted and A

Figure 47. Pre-
mostly isolated
dipoles. (a) A
density compar
concentration o

Figure 48. Dis
cooled materia
dislocation gen
was mostly pla
part shows a

Figure 49. Disl
high purity [00
end-on dislocat
the plane of the
being captured

Figure 50. Disl
found to move

Figure 51. Hig
within the foil
past its neighbo

Figure 52. Slow
cooled [001] or
individual segm

Figure 53. (a)
oriented N Al
dislocatior ne

Figure 54. Di
high purit sl
mobile dis ca
and orthog na
in the plar of
the foil ed e w

Figure 55. Hig
morpholo sh
(b) Disloc tion
existing di loc
..... ....

Figure 56. Ev
(a) Pre-ex stin
generated isl
trails. (b) lip

Figure 57. Im
(a) Disloc ion
direction f m
deformatic n ax
dislocatior s inc

Figure 58. Wi
[110] orie ted
did not in bit
purity spe me

Figure 59. W
bands in th e hi

Figure 60. M
mobile dis oca
the foil. I isl
and becom in

Figure 61. D
dislocations w
contrast for fi
Burgers vector
slip-bands in
figures (a) and

Figure 62. M
invisibility, th
mobile disloca

[101] Burgers

the slip band r
existing disloc
figures (a) and

Figure 63. Pre
high purity fa

were observed
vector. .....

Figure 64. M
Dislocations, t
and were obser

Figure 65. Th
in the right sid
good contrast

invisible in (d)

Figure 66. Ima
bands. A sign
dislocation loo
bands are in e
mobility of [1

Figure 67. Dis
The dislocatio
suggesting mo

Figure 68. Im
bands. The m
in figure (d) s
dislocations or
figures (b) and

Figure 69. V
reheated to 67
of the same ma

.....

Figure 70. An
in figure 53 (a)

Figure 71. Loo
NiAl. Figure (
forming loops

Figure 72. Sch

Figure 73. Plo
elevated temp
activation ener
Microsoft Exc

The or

over the last fe

of gas turbine

presently used

further increas

above and or d

associated with

than stoichiom

Develo

blades and va

coupled with

development p

operating temp

NiAl possesse

conductivity, a

Althou

namely, poor d

resistance at el

a sharp ductile

temperature va

orientations, str

# 1.0 INTRODUCTION

The ordered intermetallic compound NiAl has received a great deal of attention over the last few years as a potential candidate material for application in the hot sections of gas turbine engines [1-13]. Nickel-based super alloys with $Ni_3Al$ precipitates are presently used in the hot sections of engines for aircraft-propulsion systems. However, further increases in engine performance and efficiency require operating temperatures above and/or densities below those offered by the present alloys. The major limitation associated with the present alloy system is the lower melting point and the higher density than stoichiometric NiAl intermetallics.

Development of the next generation of high-temperature, high-pressure turbine blades and vanes can only be accomplished by advanced materials and processing coupled with innovative component design. The objectives of alternate material development programs are to have efficient blade cooling flow while increasing the operating temperature in conjunction with the reduction of over all engine weight [14]. NiAl possesses requisite combination of properties such as low density, high thermal conductivity, and excellent oxidation resistance.

Although NiAl has many useful properties, it suffers from two major drawbacks, namely, poor ductility and toughness at ambient temperatures, and low strength and creep resistance at elevated temperatures, particularly above 1273 K [15, 16]. NiAl undergoes a sharp ductile to brittle transition between 673 K and 473 K, with the actual transition temperature varying strongly with processing history, alloy composition, single crystal orientations, strain rate etc. [17]. A considerable research effort has been devoted in the

past decade

mechanical pr

Therm

NiAl. Faste

room tempera

embrittles the

by static str

Microalloying

NiAl single c

mechanism fo

testing at amb

stress and incre

NiAl [23 -25].

thought to be t

from stoichiom

the mechanical

possible to ach

the above-men

enhanced ducti

may be possibl

Despite

mobility and

characterized.

past decade to understand and overcome these shortcomings and to improve the mechanical properties of NiAl.

Thermal history has been shown to influence the room temperature toughness of NiAl. Faster cooling through the temperature region of 673 K to 473 K increases the room temperature fracture toughness while slower cooling through the same region embrittles the material. These observations suggest that dislocation mobility is hindered by static strain aging where interstitial impurities pin the dislocations [18-20]. Microalloying with Fe, Ga or Mo increases the room temperature tensile elongation of NiAl single crystals [21, 22]. Gettering of interstitial elements is thought to be the mechanism for this improved ductility. Hydrostatic pre-stressing prior to mechanical testing at ambient temperature and pressure has also been shown to decrease the flow stress and increase the tensile ductility during subsequent deformation of polycrystalline NiAl [23 -25]. An increase in mobile dislocation density as a result of pre-stressing is thought to be the driver for this property enhancement. Crystal orientations, deviations from stoichiometry, and surface conditions also play very important roles in controlling the mechanical behavior of NiAl single crystals. Levit et al. [26] have shown that it is possible to achieve tensile elongation as high as 25% at room temperature by optimizing the above-mentioned parameters and activating a single operative slip system. This enhanced ductility indicates that sufficient dislocation mobility at ambient temperature may be possible under specific conditions.

Despite many past studies of dislocations and slip, the exact nature of dislocation mobility and generation in achieving extensive plasticity in NiAl is not well characterized. Although the interrelation between increase in ductility and dislocation

mobility is cl

regard has be

controlling th

comprehend t

NiAl.

In ord

and high purit

crystals have b

to induce varyi

were oriented

room tempera

observed by co

motion have

Dislocations g

characterized a

mobility is clearly suggested by many investigators, no systematic investigation in that regard has been carried out. In order to develop a clear understanding of the mechanisms controlling the mechanical behavior of B2 NiAl, the present study has been undertaken to comprehend the role played by dislocation generation and mobility on the ductility of NiAl.

In order to understand the role of impurities on dislocation behavior, commercial and high purity single crystals of NiAl have been used for the investigation. The single crystals have been cooled at different rates from a homogenization annealing temperature to induce varying degrees of static strain aging. Following heat-treatment, single crystals were oriented along different stress axes. Prior plastic deformation was carried out by room temperature compression. Both deformed and undeformed specimens were observed by conventional transmission electron microscopy. Dislocation generation and motion have been studied by *in-situ* straining transmission electron microscopy. Dislocations generated in the process of plastic deformation in single crystal NiAl are characterized as a function of composition, orientation and cooling rate.

NiAl h
its physical ch
wide composi
memory effec
as the present
behavior of N
all those prop
properties, rel
the mechanica
and environm
particular emp
ductility. Rev
investigate the

2.1 Physical Pr

NiAl i

ratio of 1.5.
structure cons
(Figure 1). Th
1673 K) and s
NiAl is highly
possesses a hig

# 2.0 **BACKGROUND**

NiAl has often been a choice for basic scientific studies in ordered alloys due to its physical characteristics such as a simple crystal structure, a highly ordered lattice, a wide compositional range of stability, a variable defect structure and a reversible shape memory effect. It is important to review the physical and mechanical properties of NiAl, as the present study is intended to look into the micro-mechanisms of the mechanical behavior of NiAl single crystals. Since Miracle [6] and Noebe et al. [7] have described all those properties in great details in recent reviews, only an overview of different properties, relevant to the dislocation behavior in NiAl, is presented here. A review of the mechanical properties and elevated temperature properties such as diffusion, creep and environmental resistance of NiAl follow review of the physical properties. A particular emphasis is given to dislocations and slip systems and their implications on ductility. Review of strain aging in NiAl is included as the present study also aims to investigate the strain aging behavior of high and commercially pure NiAl single crystals.

## 2.1 Physical Properties

NiAl is an ordered β-phase electron compound with a valence electron to atom ratio of 1.5. The primitive cubic B2 (CsCl prototype, space group $\bar{P}$m3m) crystal structure consists of two interpenetrating simple cubic sub-lattices of Ni and Al atoms (Figure 1). The B2 structure is stable for large deviations from stoichiometry (~20 at% at 1673 K) and significant long-range order is observed up to the melting temperature [27]. NiAl is highly ordered and even quenching @ $10^8$ K/s cannot suppress the order. NiAl possesses a high degree of thermodynamic stability with a negative heat of formation of

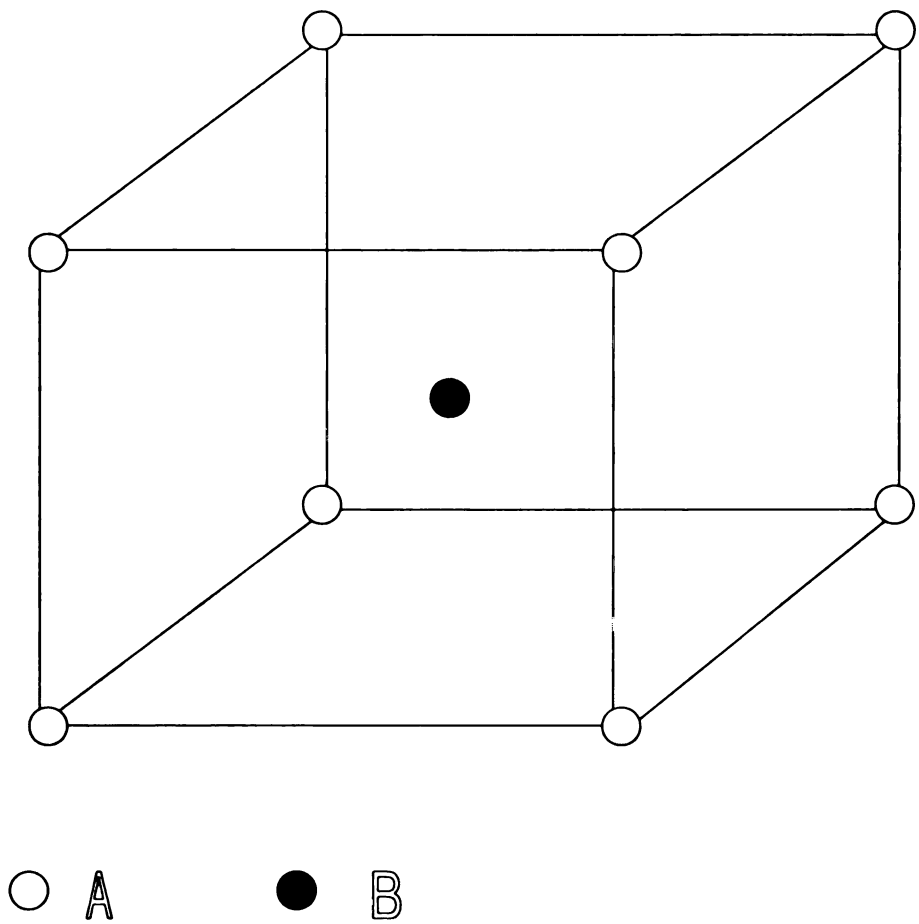


Figure 1. B2 structure, also known as the ordered bcc lattice. Two types of atoms (A and B) occupy the corner positions or body center position respectively.

72.2 kJ g-aton
covalent is th
significant bu
direction [6, 7
B2 N
application, ha
the phase dia
congruently at
materials. Th
and improved
stoichiometry
temperature, s
0.2887 nm. Th
density advan
depending on t
The ele
cm (typical of
electron scatte
NiAl is about
alloys. Stoich
thermal condu
larger than that
[1].

72.2 kJ/g-atom [28]. Bonding in NiAl is a mixture of covalent and metallic type, where covalent is the dominant feature of bonding. High NiAl bond strength results from significant build up of directional d-bonding charge along the nearest neighbor NiAl direction [6, 7].

B2 NiAl, a potential candidate material for high temperature structural application, has some specific advantages over conventional Ni-base superalloys. From the phase diagram (Figure 2) [29] it is evident that stoichiomentric NiAl melts congruently at 1911 K, which is at least 300 K more than that for conventional Ni-base materials. The higher melting point offers advantages of higher operating temperature and improved creep resistance. The solidus melting point depends strongly on stoichiometry and drops sharply with deviations from stoichiometry. At room temperature, stoichiometric NiAl has a density of 5.95 $g/cm^3$, with a lattice constant of 0.2887 nm. The density is at least 3 $g/cm^3$ lesser than the nickel-base super-alloys. This density advantage could result as much as a 40% weight saving in an aircraft engine, depending on the rotary motion of the turbine components [1].

The electrical resistivity of stoichiometric NiAl at room temperature is 8-10 $\mu\Omega$-cm (typical of metals) and increases on both sides of stoichiometry due to increased electron scattering by constitutional defects [30]. The thermal expansion coefficient of NiAl is about 30% lower than pure Ni, but is very similar to that of nickel-base super-alloys. Stoichiometry has little influence on coefficient of thermal expansion. The thermal conductivity of NiAl single crystal is 70-80 W/m-K, which is almost eight times larger than that of conventional nickel base super-alloys and about one-third of aluminum [1].

Figure 2. Pha
the Ni-Al alloy

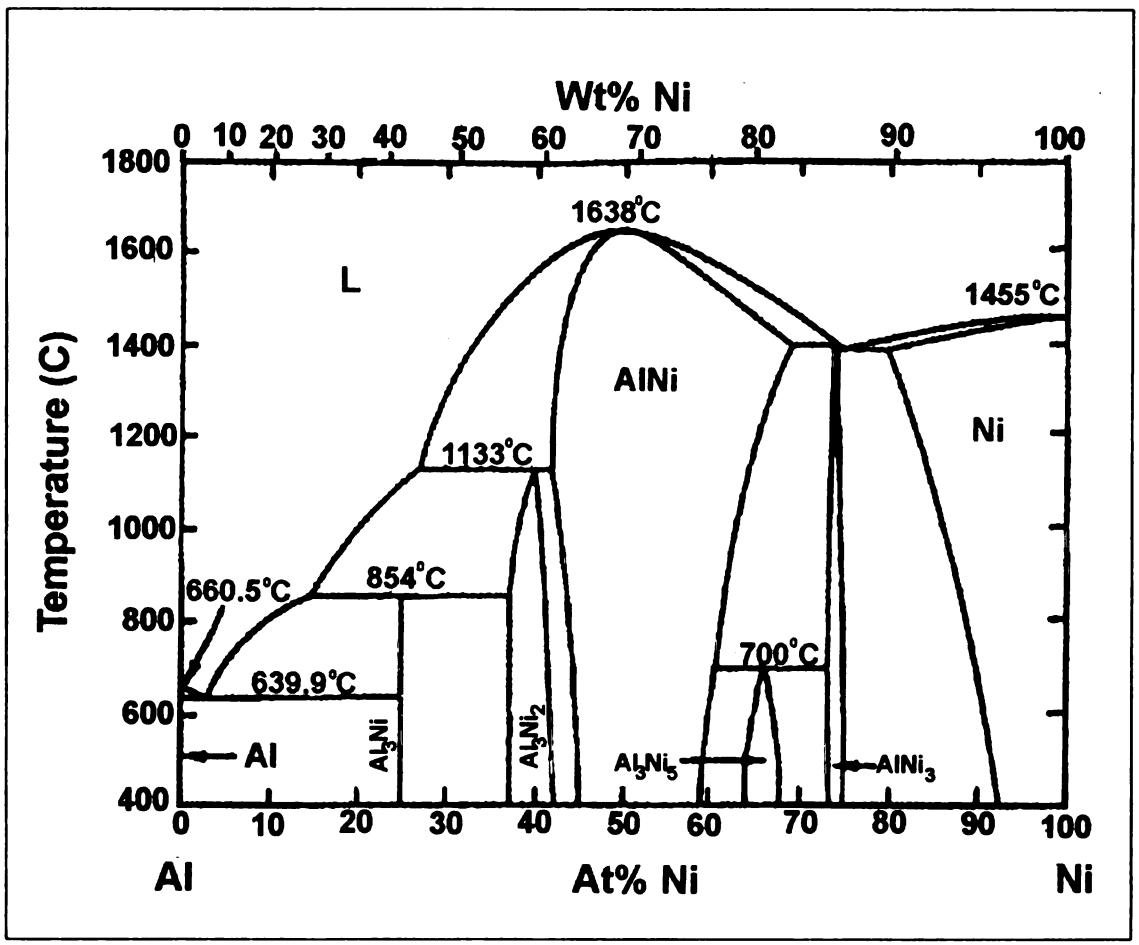


Figure 2. Phase diagram illustrating the phase stability as a function of temperature for the Ni-Al alloy system [29].

The n

Thus, when

density is ex

takes place f

Al and Ni ato

X $10^{-20}$ J [6].

and the stoich

and gray for

the sharp cha

NiAl

on orientation

this is measu

constants. 'A

than strongly

temperature (

52% Al and A

The Yo

as a function o

where E and G

the Young's m

and <111> or

strength is also

The nickel atom is heavier and smaller in size in comparison to the Al atom. Thus, when Ni is substituted for Al, a reduction in lattice parameter and increase in density is expected. On the contrary, a decrease in both lattice parameter and density takes place for Al-rich alloys (Figure 3) [7]. The maximum interaction energy between Al and Ni atoms is observed at the stoichiometric composition and is of the order of -11.5 X $10^{-20}$ J [6]. The visible appearance of NiAl is heavily dependent on the alloy chemistry and the stoichiometric bright blue color changes to yellow or bronze for Ni-rich alloys and gray for Al-rich alloys; interband transitions associated with Fermi surface results in the sharp change in color [7].

NiAl is crystallographically anisotropic and the elastic properties depend strongly on orientation. Stoichiometric NiAl possesses an elastic anisotropy factor (A) of ~3.3; this is measured by Zener's parameter, $A = \frac{2C_{44}}{C_{11} - C_{12}}$, where C is the elastic stiffness constants. 'A' for NiAl is comparable with Cu (~3.21) and Ag (~3.01) and much lower than strongly anisotropic material such as β-brass (~8.49). 'A' is weakly dependent on temperature (~2.94 at 873 K) and strongly dependent on composition (A = 2.56 for Ni-52% Al and A = 5.67 for Ni-45% Al) [31].

The Young's modulus (E) and shear modulus (G) of NiAl have been determined as a function of temperature [7]:

$$E = 199.8 - 0.04\,(T) \text{ and } G = 76.6 - 0.0.17(T),$$

where E and G is in GPa and T is in K. The single crystal orientation strongly influences the Young's modulus, with values of 96 GPa, 187 GPa and 275 GPa for <011>, <100>, and <111> orientations respectively for nearly stoichiometric NiAl [31]. The yield strength is also strongly dependent on alloy chemistry and shows a minimum at the

Lattice Parameter (nm)

Figure 3. Latt

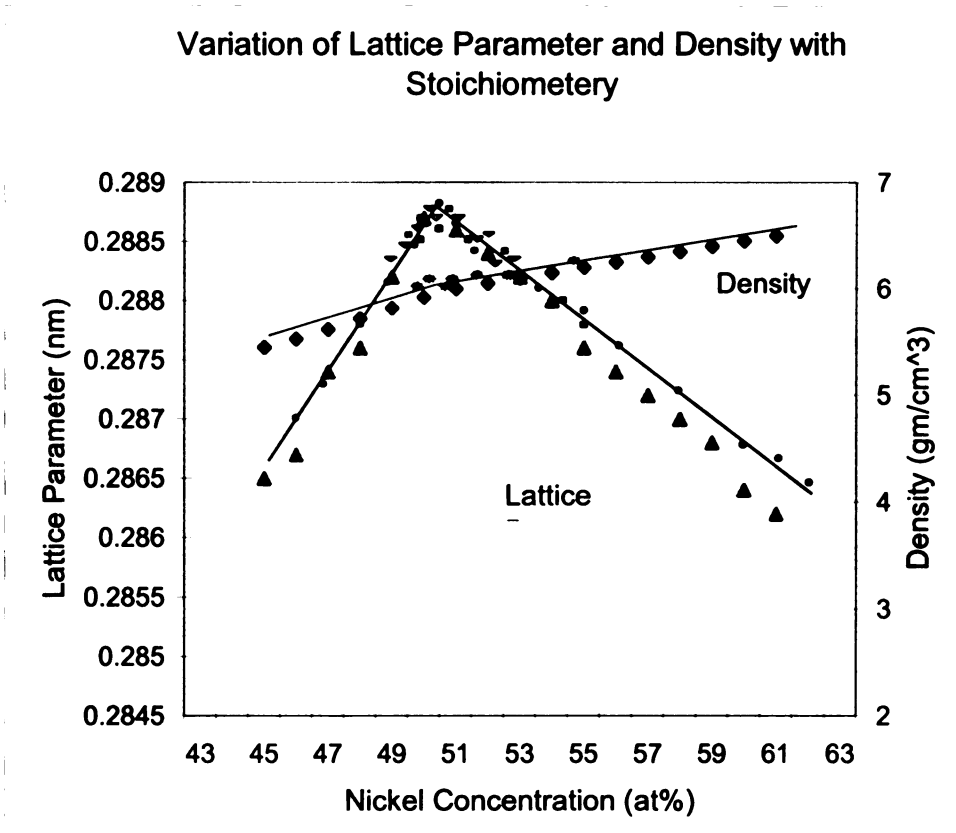


Figure 3. Lattice parameter and density of NiAl vary as a function of stoichiometry [7].

stoichiometri

independent

Ni-Al is fou

susceptibility

weakly relate

2.2 Mechanic

All of

strongly by th

(point defects

the focus of

crystalline def

ductility, fract

2.2.1 Crystal

Depen

line, and sur

mechanical pr

2.2.1.1 Point

NiAl

have triple d

[35]; α and

defect free la

defects, two

stoichiometric composition [32-34]. Poisson's ratio (ν) have been found to be almost independent of temperature, T:

$$\nu = 0.307 + 2.15X10^{-5}\,T\ [6].$$

Ni-Al is found to be non-magnetic or Pauli paramagnetic, with a low magnetic susceptibility of $\sim 2X10^{-2}$ to $6X10^{-2}$ emu/gm; magnetic susceptibility of NiAl is very weakly related with temperature and composition [7].

2.2 Mechanical Properties

All of the mechanical properties of NiAl are structure-sensitive and influenced strongly by the defect structure, whether it is localized to the proximity of a few atoms (point defects) or extends through the microscopic regions (lattice defects). Considering the focus of the present study on the mechanical behavior of NiAl, a review of the crystalline defects in NiAl will be presented first, which will be followed by slip systems, ductility, fracture, and strain-aging.

2.2.1 Crystal Defects

Depending on the scale of presence, the crystalline defects are classified as point, line, and surface or planar defects. These three defects and their influence on the mechanical properties of NiAl will be reviewed in the following sub-sections.

2.2.1.1 Point Defects

NiAl exhibits both constitutional defects and vacancies. NiAl is considered to have triple defect structure i.e. when A atom occupy the β site, the α site remain vacant [35]; α and β are the sites normally occupied by the A and B atoms respectively in a defect free lattice. The term triple defect refers to the simultaneous presence of three defects, two vacancies on α site and one A atom on β site at the stoichiometric

composition.

stoichiometry

Al atoms on

are formed in

and strong t

constitutional

minimize the

vacancy form

symmetric wi

Beside

thermal vacan

stoichiometei

temperatures,

density of qu

energy and sli

thermal vacan

modulus [40]

produced by

[41]. Therm

rapid quenchi

annealing at

composition. Usually the Al sites are fully occupied. With deviations from stoichiometry Al atoms never reside on Ni sublattice. Any excess Ni atom substitutes on Al atoms on the Al sublattice on the Ni rich side. Vacant sites or constitutional defects are formed in the Ni sublattice with excess Al [7]. Because of the high ordering energy and strong tendency to avoid the same defect species in the nearest neighbor site, constitutional defects in NiAl exhibit somewhat ordered structures that also help to minimize the strain energy associated with the introduction of a defect [36]. The ease of vacancy formation differs in the two sub-lattices and as a result vacancy formation is not symmetric with stoichiometry [37].

Besides constitutional vacancies it is possible to quench a high concentration of thermal vacancies that leads to strengthening in NiAl [38]. Near the melting point of stoichiometeic alloy, 2% of thermal defects may exist. After quenching from moderate temperatures, 0.5 - 1% of such vacancies can be retained [39]. The presence of a high density of quenched-in vacancies might be a consequence of relatively low formation energy and slightly higher migration energy for vacancies in NiAl. These supersaturated thermal vacancies increase the yield strength without significantly affecting the elastic modulus [40]. Vacancies offer a much greater resistance to dislocation motion than that produced by substitutional atoms, and the increase in hardness can be as high as 20% [41]. Thermal vacancies are susceptible to agglomeration and form faceted voids after rapid quenching from the melt [38, 42]. Dislocation loops and helices are formed during annealing at lower temperature by thermally induced vacancies [33, 41-43].

2.2.1.2 Line I

The s

of any materi

in wrong nea

order of the l

NiAl. All of

vectors occur

into partials.

structure take

energy and th

screw orient

configuration

extra energy i

screw orienta

Non-e

decompositio

proposed that

form an $a<0$

$a<110>\{110\}$

a 20% decre

sufficiently lo

A sma

on $\{110\}$ slip

2.2.1.2 Line Defects

The study of dislocations is important in understanding the mechanical behavior of any material. The large ordering energy in NiAl does not favor slip vectors that result in wrong nearest neighbor atoms. Three basic translation vectors that do not disrupt the order of the lattice are $a$<011>, $a$ <100> and $a$ <111> where $a$ is the lattice constant of NiAl. All of these dislocations have been observed in NiAl, although non-<001> slip vectors occur under specific circumstances [6, 7]. The dislocation cores partly dissociate into partials, and with increase in planar fault energy a transition to undissociated structure takes place [44]. Dislocations with <001> Burgers vectors have the lowest line energy and the edge orientation of <001> dislocation has slightly lower energy than the screw orientation (Figure 4) [41]. $a$<001> dislocations within 25° of the screw configuration are elastically unstable on {110} and {001} planes [6, 45]. Thus, some extra energy is required to force an elastically stable $a$<001> mixed dislocations into the screw orientation.

Non-edge $a$<110> dislocations on {110} planes have sufficiently low energy that decomposition into two $a$<001> dislocations is not expected [6]. However, it has been proposed that an $a$<110> edge dislocation lying on an {110} plane may decompose to form an $a$<001> edge dislocation and an $a$<001> screw dislocation. [40]. An $a$<110>{110} edge dislocation can dissociate into two $a/2$<111> dislocations resulting in a 20% decrease in energy and require the antiphase boundary (APB) energy to be sufficiently low [6, 46].

A small amount of elastic instability is associated with $a$<111> edge dislocations on {110} slip planes but not on {112} planes [45, 47]. These $a$<111> dislocations may

Figure 4. Di
Dislocation lin

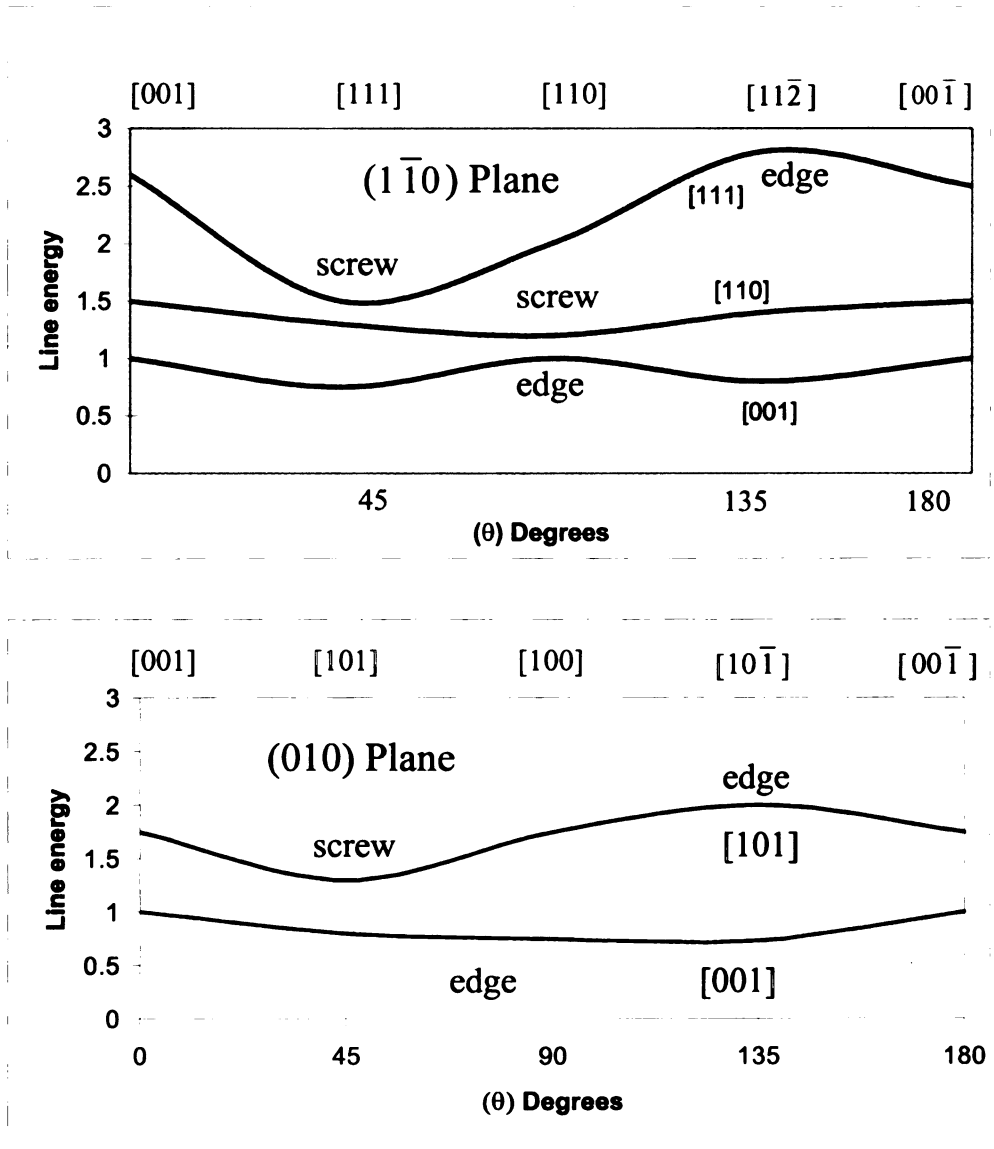


Figure 4. Dislocation line energy in stoichiometric NiAl at room temperature. Dislocation line directions are measured from [001] direction [41].

dissociate in

appropriate l

loops are ob

character and

2.2.1.3 Planar

In ger

to differentia

energies exist

crystals, it is

faults likely t

alloys (53 - 5

by clustering

{001} planes

in NiAl [45, 4

2.2.2 Slip Beh

The de

on the orienta

hard and soft

vectors have

deformation is

systems [7].

slip vector do

dissociate into $a$<001> + $a$<110> dislocations or three $a$<001> dislocations of appropriate line direction on the {110} planes [6]. Several types of sessile dislocation loops are observed after room temperature deformation [7]; these loops are edge in character and lie in {001} planes with $a$<001> Burgers vectors [7, 43, 48].

2.2.1.3 Planar Defects

In general, stoichiometric NiAl does not exhibit any planar defects. The inability to differentiate splitting in superlattice dislocations strongly suggests that high fault energies exist in NiAl. Based on theoretical analyses of possible planar faults in B2 crystals, it is revealed that $a/2$<111>APBs on {110} and {112} planes are the only stable faults likely to occur in NiAl [49]. Deviation from stoichiometry in slow-cooled Al rich alloys (53 - 54 at%) gives rise to planar faults. These planar faults are suggested to form by clustering of point defects, which are either vacant Ni sites or excess Al atoms on {001} planes [50]. In general, deformation induced planar faults have not been observed in NiAl [45, 47].

2.2.2 Slip Behavior

The deformation and slip behavior of NiAl single crystals is strongly dependent on the orientation of the single crystal. The literatures generally classify orientation as hard and soft. Orientations close to <001> are considered 'hard' because <001> slip vectors have zero or near zero resolved shear stress and the stress necessary for deformation is several times greater than for any other orientation to operate alternate slip systems [7]. 'Soft' orientations include all non<001> directions of loading, where <001> slip vector dominates.

NiAl

orientations

dislocation g

the primary s

[32, 45, 50].

the operatio

orthogonal

slip on {110

dislocations

Wasilewski e

deformed bet

than for <001

Defor

and {110} pla

K [47, 55, 5

<110> and <

(~77 K), the

At higher ten

deformation

combination

Sampl

hard oriented

<111> slip o

NiAl exhibits two significantly different types of slip behavior [50-63]. For 'soft' orientations <001> slip vectors dominate and do not depend on temperature. Considering dislocation glide in non<001> oriented single crystals, <001>{110} and <001>{001} are the primary slip systems and have been confirmed by various TEM and slip trace studies [32, 45, 50]. In the temperature range of 300 – 1273 K, Ball and Smallman [52] found the operation of <001>{110} slip in soft orientations and observed cross-slip on orthogonal {110} planes. Although the critical resolved shear stress values for <001> slip on {110} or {001} are similar, relative mobility calculations revealed that <001> dislocations preferentially glide on {110} planes to {001} planes [52, 59, 60]. Wasilewski et al. [32] observed cube slip <010>{100} in <110> oriented single crystals deformed between 473 and 973 K; <001>{001} slip occurred at slightly higher stresses than for <001>{110} slip [52, 59].

Deformation of hard oriented single crystals take place by <111> slip on {112} and {110} planes between 77 K and 300 K [45] and between room temperature and 600 K [47, 55, 56]. Depending on the deformation temperature, a combination of <111>, <110> and <001> slip vector dominates for hard orientations. At very low temperatures (~77 K), the observed slip direction is <111> on {110}, {112} or {123} planes [45, 53]. At higher temperatures (>600 K), <111> dislocations become thermally unstable and deformation has been reported to be the result of motion of <001>, <110>, or a combination of glide and climb of <001> and <110> dislocations [51, 54-56, 61].

Sample geometry plays an important role in determining deformation behavior of hard oriented single crystals. Both kinking and uniform deformation takes place by <111> slip on {112} and {110} planes during deformation of hard oriented single

crystals [7].

confirmed as

2.4 and 3) in

56]. This w

ratio of the c

promoted the

ratio [63].

Defor

dislocations

independent

According to

five independ

In NiAl, no

could give ri

arbitrary stra

Although <1

no tensile du

ambient temp

cleavage has

by alloying a

almost exclu

observed in

have very litt

crystals [7]. However, kinking has never been reported in any tension test and is confirmed as an artifact of an unstable testing geometry (length to diameter ratio between 2.4 and 3) in compression tests, which proceeds by movement of <001> dislocations [54, 56]. This was supported by the presence of only <111> dislocations when the aspect ratio of the compression specimen was kept ~2 [7, 45]. Also, alloying additions of Cr promoted the activation of <111> slip over deformation by kinking for a constant aspect ratio [63].

Deformation of polycrystalline NiAl generally occurs by the operation of <001> dislocations as in the case of soft oriented single crystals [57, 58]. Only three independent slip systems are available as a result of this predominantly <001> slip. According to Von Mises criterion for plastic deformation of polycrystalline materials, five independent slip systems are required to accommodate any arbitrary shape change. In NiAl, no extra independent slip system is provided by cross-slip [52]. <111> slip could give rise to five independent slip systems, which is sufficient to produce an arbitrary strain and extensive crack free deformation without change in volume. Although <111> slip satisfies the requirements for generalized polycrystalline plasticity, no tensile ductility has been reported in Mn or Cr containing polycrystalline NiAl at ambient temperature; a change in fracture mode from intergranular to transgranular cleavage has been observed with <111> slip [7]. Attempts to alter the slip vector of NiAl by alloying addition had not been successful as majority of the investigations reveal almost exclusively <001> dislocations. In extruded alloys <110> dislocations are observed in {011} planes, which are considered as a product of dislocation reactions and have very little potential to increase plasticity [7].

2.2.3 Yield S

It ha

strongly on t

room temper

extended ov

stress decrea

single crysta

orientations [

polycrystals a

hard oriented

and 300 K ar

hard and sof

diffusion start

Like (

(Figure 5) [7

reaches the n

significantly h

between 300 a

NiAl increase

of different te

[7, 57, 66].

segregation an

~0.036 nm in

2.2.3 Yield Strength

It has been established that the yield stress ($\sigma_y$) of polycrystalline NiAl depends strongly on the temperature of deformation below room temperature but at or close to room temperature an athermal regime is observed [64]. These athermal plateaus are extended over 300 K, and generally occur between room temperature and 800 K. Yield stress decreases slowly with increasing temperature beyond this plateau temperature. For single crystals, the yield stress is much higher in hard orientation, than any other orientations [7]. Soft oriented single crystals exhibit similar temperature dependence like polycrystals and the yield stress decreases continuously with increasing temperature. For hard oriented single crystals, yield stress is a strong function of temperature between 77 and 300 K and deformation takes place by <110> and <001> slip; above 900 K, both hard and soft oriented single crystals and polycrystals behave similarly as the bulk diffusion starts to dominate [7].

Like other properties of NiAl, the yield strength depends heavily on stoichiometry (Figure 5) [7]. The flow stress and hardness reaches the minimum and the ductility reaches the maximum value at stoichiometric composition. The flow stress increases significantly by deviating from stoichimetry. The yield stress is moderately constant between 300 and 600 K and decreases sharply above 600 K [64, 65]. The flow stress of NiAl increases highly in the presence of solutes. Table I and figure 6 describe the effects of different ternary additions on solid solution strengthening of NiAl at room temperature [7, 57, 66]. B and Zr give a much higher hardening rate because of grain boundary segregation and second phase particle formations. The calculated interstitial site radius is ~0.036 nm in NiAl and it is predicted that smaller atoms like B and C are more probable

Figure 5. Y

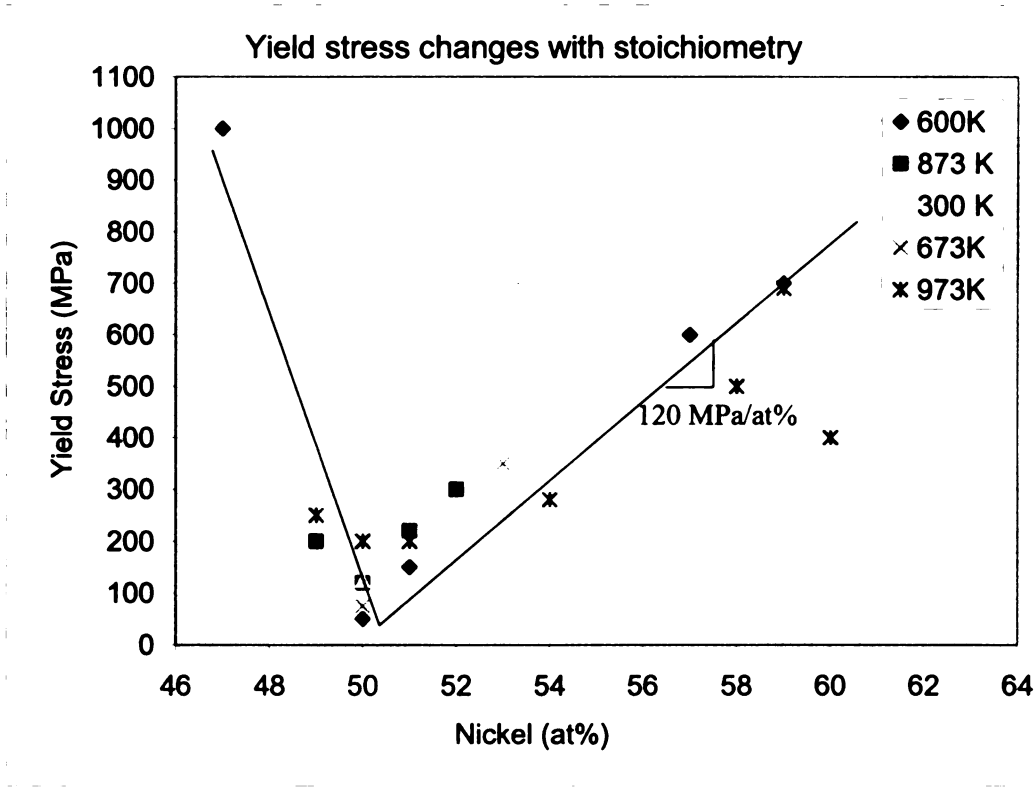


Figure 5. Yield stress of NiAl varies strongly as a function of stoichiometry [7].

TABLE I. Solid Solution Strengthening in NiAl [7]

| Element | Concentration | Atomic Radii (nm) | $\frac{\Delta\sigma_y}{\Delta C}$ (MPa/at%) | Goldschmidt radii, nm |
|---|---|---|---|---|
| Boron | 0.04 | 0.117 | 4500 | 0.093 |
| Zirconium | 0.05 | 0.216 | 4000 | 0.157 |
| Carbon | 0.11 | 0.0091 | >1700 | 0.084 |
| Chromium | 1.00 | 0.185 | 258 | 0.125 |
| Beryllium | 0.24 | 0.140 | 100 | 0.111 |

Change in Hardening rate (MPa / at%)

Figure 6. R

single cryst

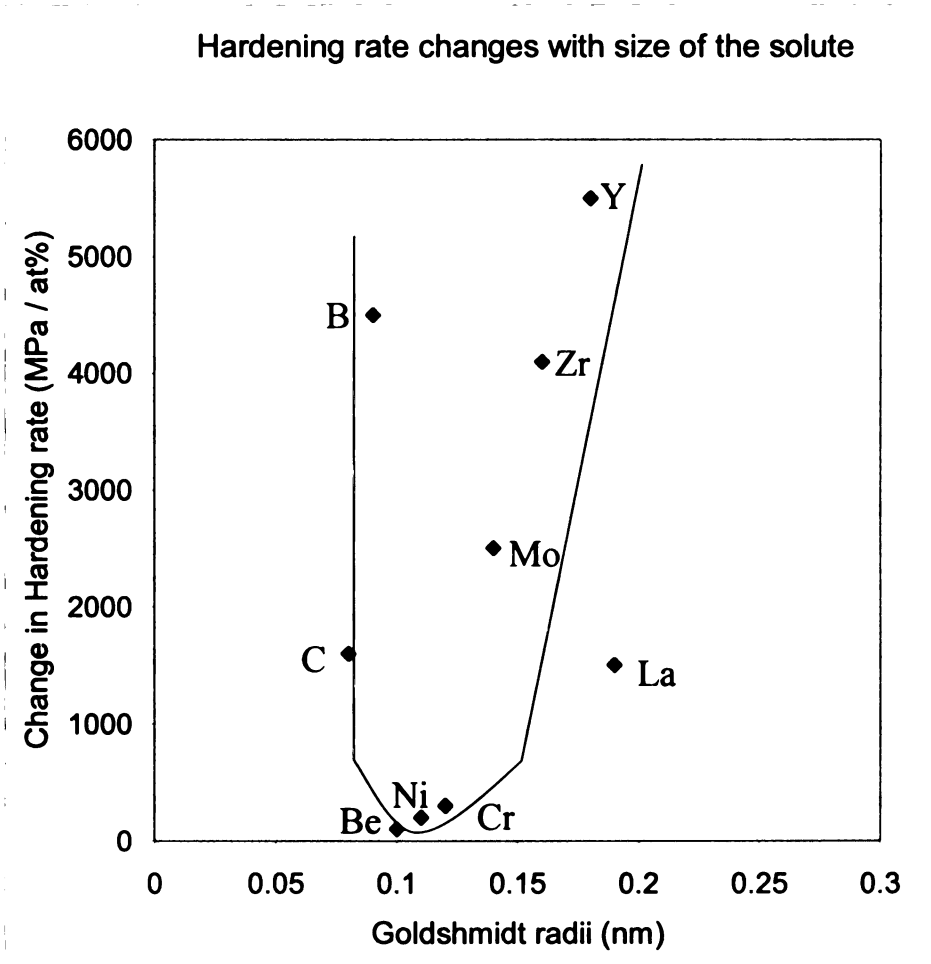


Figure 6. Relationship between hardening rate and size of the solute elements in NiAl single crystals [7].

to occupy t

stoichiomet

Ni or Al-ri

vacancies in

considered t

The y

grain size ca

The yield str

conversely g

alloys. Ho

increasing te

For p

or below 50

altered at ele

strain rate se

T < 1350 K)

per second to

2.2.4 Ductilit

The r

material is it

limited (< 2.

K. Soft or

temperatures

to occupy the interstitial sites [66]. Discontinuous yielding has been reported in off-stoichiometric alloys. Serrated stress strain curves or presence of yield points for either Ni or Al-rich alloys are considered as discontinuous yielding; while the presence of vacancies in Al-rich alloys are responsible for serrations, dynamic recrystallization is considered to be the driving mechanism in Ni-rich alloys [67, 68].

The yield stress is affected by the grain size in a complex manner. Decreasing the grain size can decrease or increase the yield stress or it may not be impacted at all [7]. The yield stress is almost independent of grain size for nearly stoichiometric NiAl alloys; conversely grain-size influences the yield stress significantly for non-stoichiometric alloys. However, this influence of deviation from stoichiometry decreases with increasing temperature and becomes negligible above 800 K [7].

For polycrystalline NiAl alloys, yield stress is marginally affected by strain rate at or below 500 K, moderately influenced at intermediate temperatures, and significantly altered at elevated temperatures [57]. Rozner and Wasilewski [69] observed the largest strain rate sensitivity of cube oriented single crystals at intermediate temperatures ($750 < T < 1350$ K); the increase in flow stress was ~ 30% for a change in strain rate from $10^{-4}$ per second to $10^{-3}$ per second.

2.2.4 Ductility

The most serious limitation associated with the application of NiAl as a structural material is its lack of room temperature ductility. Until the work of Levit et al. [26] limited (< 2.5%) tensile ductility was reported for soft oriented single crystals below 500 K. Soft oriented NiAl single crystals undergo a brittle to ductile transition at temperatures ~473 K (about $0.25T_m$) [1]. Different factors such as insufficient

dislocation

slip contrib

single cryst

As a result

crystals may

Roo

stoichiometr

less than 1°

yield strengt

Micr

crystals sign

be achieved

Fe; Ga or M

in ductility

effect in in

interstitial e

this tremen

understood.

Hard

temperature

crystals belo

of $a$<111> d

crystals occu

dislocation sources, lack of dislocation mobility, low fracture stress, and heterogeneous slip contribute to this limited ductility at relatively low temperature [11]. As-grown single crystals contain mostly edge dislocations, which typically lie on cube planes [40]. As a result of low concentration of mobile dislocations on {110} slip planes, NiAl single crystals may be dislocation source limited [40, 70].

Room temperature plasticity of NiAl is heavily dependent on the alloy stoichiometry. The ductility is maximum at stoichiometric composition and deviations of less than 1% from stoichiometry results in brittleness and a corresponding increase in yield strength [7].

Micro-alloying additions have been shown to improve the ductility of NiAl single crystals significantly. Darolia et al. [1, 21, 22] observed that a tensile strain of 6% could be achieved for soft oriented single crystals by doping with approximately 1000 ppm of Fe; Ga or Mo exhibit similar effect but not as pronounced as Fe (Figure 7). This increase in ductility shows that alloying with more than 0.5% of these elements has no further effect in increasing the ductility and in fact the benefit might be lost. Gettering of interstitial elements or slip homogenization is thought to be the governing mechanism for this tremendous increase in ductility, although the exact mechanism is yet to be understood.

Hard oriented single crystals are brittle and often fail without yielding at room temperature [55]; limited tensile ductility is observed for hard oriented NiAl single crystals below 600 K [17]. The little observed uniform deformation occurs by the glide of $a$<111> dislocations [45, 55]. The ductile brittle transition for hard oriented single crystals occurs at ~600 K [7]. Above that temperature, glide of $a$ <110> dislocations

Figure 7
microall

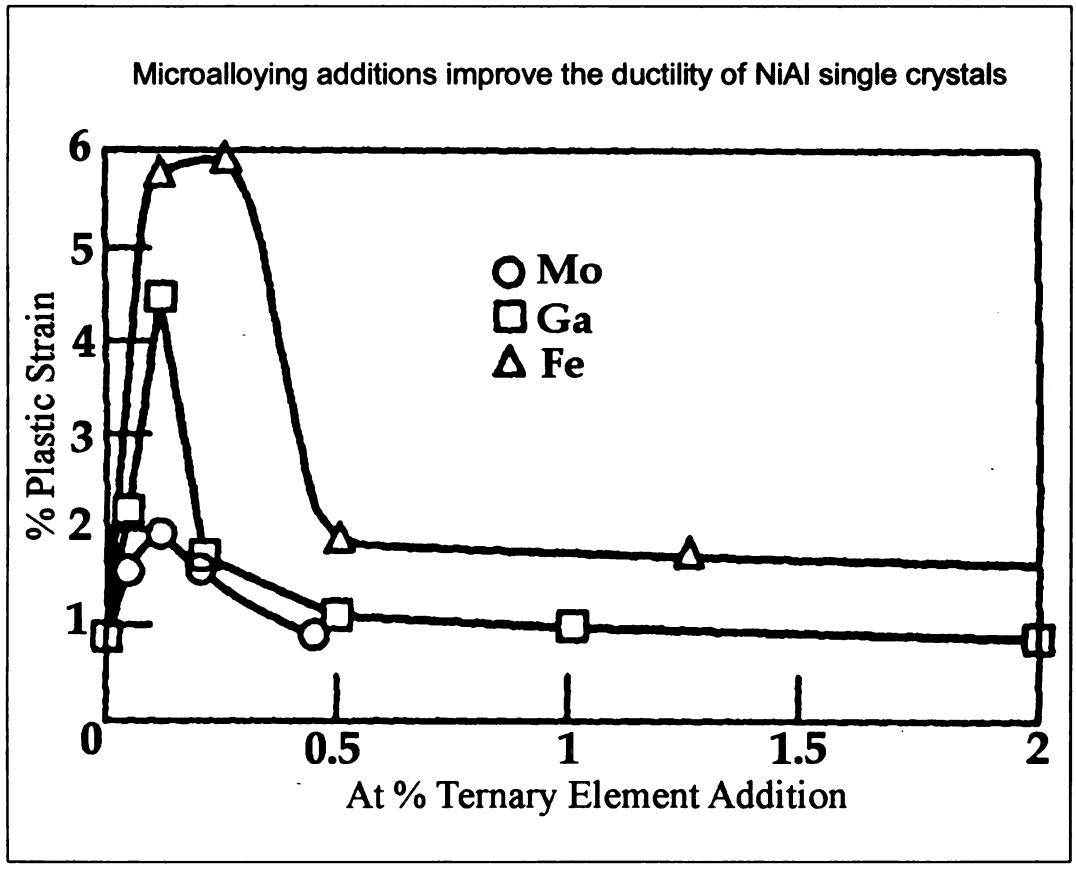


Figure 7. Room temperature ductility of <110> oriented NiAl single crystal with microalloying additions [1].

takes place

strain) [55]

sufficient t

predominan

rotation [6.

Simi

ductility at

limited by t

71]. Hydros

atmospheric

increase in

attributed to

inclusions or

2.2.5 Fractur

Fract

It is importa

complete un

2.2.5.1 Fract

In ge

growth. Sto

irrespective

of lower (3

Polycrystallir

takes place, which leaves $a$<001> debris after a small amount of deformation (~1.5% strain) [55]. Further deformation results in a rotation of the deformation axis that is sufficient to activate $a$<001> glide dislocations; glide of $a$<001> dislocations become predominant after no more than ~6% strain, due to deformation induced crystal axis rotation [6, 55].

Similar to soft oriented single crystals, polycrystalline NiAl exhibits limited ductility at room temperature [65, 66, 69, 71]. The ductility of polycrystalline NiAl is limited by the incompatibility of shape changes of neighboring grains [55, 65, 66, 69, 71]. Hydrostatic pressurization between 300 and 1400 MPa prior to mechanical testing at atmospheric pressure (0.1 MPa) decreases the flow stress by approximately 40% with an increase in tensile ductility [23-25]. This change in mechanical behavior has been attributed to increased dislocation generation at areas of local shear stress such as inclusions or other material heterogeneities.

2.2.5 Fracture Behavior

Fracture behavior of any material is a critical index for its toughness and ductility. It is important to review the fracture mode and fracture toughness of NiAl to develop a complete understanding of the mechanical properties.

2.2.5.1 Fracture Mode

In general, room temperature fracture in NiAl occurs without any stable crack growth. Stoichiometric NiAl single crystals typically fail by cleavage on {110} planes irrespective of orientation [11, 64, 66, 71, 72]. This cleavage behavior is a consequence of lower (30%) cleavage energy on {110} planes than on {001} planes [73]. Polycrystalline materials primarily fail by intergranular fracture at low temperatures [65,

66, 74]. T

temperature

grain size.

alloys or al

room tempe

2.2.5.2 Fract

NiAl

extensive ro

fracture tou

room tempe

shows limi

toughness

toughness v

The

polycrystal

orientation

temperatur

crystals wi

toughness

value of ~1

The

materials a

increase in

66, 74]. Transgranular cleavage takes place at and above 673 K [65]. At ambient temperatures, the tendency towards transgranular fracture increases with increasing the grain size, strain rate and deviations from stoichiometry [6, 75]. Non-stoichiometric alloys or alloys with ternary or quaternary additions, which are not known to exhibit room temperature ductility, fail in a predominantly transgranular mode [75].

2.2.5.2 Fracture Toughness

NiAl displays extreme brittleness at ambient temperatures. In absence of extensive room temperature tensile elongation, ductility of NiAl is often measured by fracture toughness tests, which also represent the internal resistance to cracking. The room temperature fracture toughness of polycrystalline NiAl lies between 4 - 6 MPa and shows limited dependence on grain size and stoichiometry [76-78]. This fracture toughness value is similar to many ceramic materials such as $Al_2O_3$ with fracture toughness values in the range of 5 - 6 MPa$\sqrt{m}$ [7].

The fracture toughness values of NiAl single crystals are similar to single phase polycrystalline material and have been observed to vary significantly with crystal orientation and temperature. The plane strain fracture toughness ($K_{IC}$) at room temperature has been determined to be 4.5 MPa$\sqrt{m}$, 5.1 MPa$\sqrt{m}$ and 8 MPa$\sqrt{m}$ for single crystals with <110>, <111>, and <001> stress axes respectively [6, 78, 79]. Fracture toughness generally increases with increasing temperature and above 500 K toughness value of ~15 MPa$\sqrt{m}$ has been reported for soft oriented single crystals [6].

The $K_{IC}$ increases between 573 and 673 K to about 10 MPa$\sqrt{m}$ for as-cast materials and to about 50 MPa$\sqrt{m}$ for zone-refined materials [76]. This signifies an increase in fracture toughness with alloy purity at elevated temperature, although room

temperatur

material.

2.2.6 Strain

NiA

that the fra

controlled

elongation o

temperature

crystals are

disappears v

crystals at 6

in substanti

by slow coo

susceptible

NiA

of the mobi

such as occ

and plateau

present in t

[81] observ

Silicon enh

as diffusivi

compressio

temperature fracture toughness for the zone-melted material remains as low as original material.

2.2.6 Strain Aging

NiAl is has a high susceptibility to strain aging. Hack et al. [18 - 20] observed that the fracture resistance of NiAl single crystals could be significantly improved by controlled heat treatments. Furnace-cooled NiAl single crystals exhibit a tensile elongation of 1% and a fracture toughness of 2.4 MPa$\sqrt{m}$ at room temperature. The room temperature tensile ductility and $K_{IC}$ increase to 7% and 17 MPa$\sqrt{m}$ respectively if the crystals are re-heated to 673 K and air-cooled. The beneficial effect of fast cooling disappears when the crystals are furnace-cooled from 673 K. Creep bending of single crystals at 673 K and subsequent annealing at 473 K followed by furnace cooling results in substantial toughness [18]. These observations indicate that static strain aging occurs by slow cooling, whereas dislocations generated by high temperature deformation are not susceptible to strain aging.

NiAl exhibits severe strain aging as interstitial atoms tend to segregate to the core of the mobile dislocations. Many of the conspicuous features of strain aging phenomena such as occurrence of yield points, discontinuous yielding, low strain rate sensitivities and plateaus in the temperature dependence of yield stress, and work-hardening rates are present in the deformation of single crystal and polycrystalline NiAl [80]. Weaver et al. [81] observed serrated flow in the presence of C (>150 ppm) and Si (>1500 ppm). Silicon enhances the serrations in the stress-strain plots by increasing the activity as well as diffusivity of carbon in NiAl. Brzeski et al. [20] observed serrated yielding during compression testing between 373 K and 473 K, in contrast to smooth yielding at room

temperatur

between 70

and O are t

typical of it

dynamic str

is the main

help to rem

Yield point

hydrostatic

annealing of

2.3 Diffusion

In al

considered a

cycle consist

mechanism

activation en

The diffusion

increase in

concentration

gradually dec

90]. The rap

NiAl and dr

activation ene

temperature. In a separate study, Brzeski et al. [82] have also observed serrated flow between 703 K and 873 K. Calculated activation energies for the process suggests that C and O are the probable agents for this serrated yielding behavior. These serrations are typical of interactions between dislocations and interstitial solutes, commonly known as dynamic strain aging. Weaver et al. [83] have shown that carbon, not oxygen or nitrogen, is the main interstitial element responsible for strain aging. Alloying with Ti and Mo help to remove the yield point totally for their strong affinity towards carbon [81, 84, 85]. Yield points could be suppressed by faster cooling from higher temperatures, and by hydrostatic pre-stressing [83, 86]. Recovery of yield points is observed by subsequent annealing of pre-stressed material at 700 K [87].

2.3 Diffusion

In absence of divacancy mechanism, next nearest-neighbor vacancy jumps is considered as the important diffusion mechanisms in NiAl; in addition to that a six jump cycle consisting only of nearest-neighbor vacancy jumps is also proposed as an operative mechanism [88, 89]. A minimum in the diffusion co-efficient and maximum in the activation energy is observed near stoichiometric composition (Figure 8 a and 8 b) [7]. The diffusion coefficient increases significantly with deviations from stoichiometry. This increase in diffusivity with increase in Al is caused by the presence of a high concentration of constitutional vacancies and thermal vacancies. The activation energy gradually decreases to the Ni-rich side and drops sharply for Al-rich compositions [89, 90]. The rapid decrease in activation energy is a result of faster diffusion of Al in Al-rich NiAl and driven by the energy of motion of constitutional vacancies. The higher activation energy on the Ni-rich side consists of both the energies to create and to move

Activation Energy (kJ/mol)

Figure 8. D
species in N

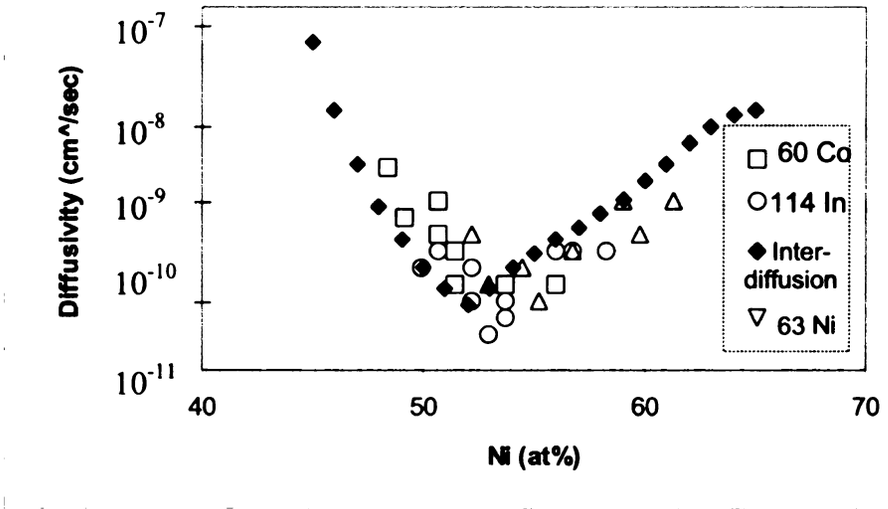


(a)

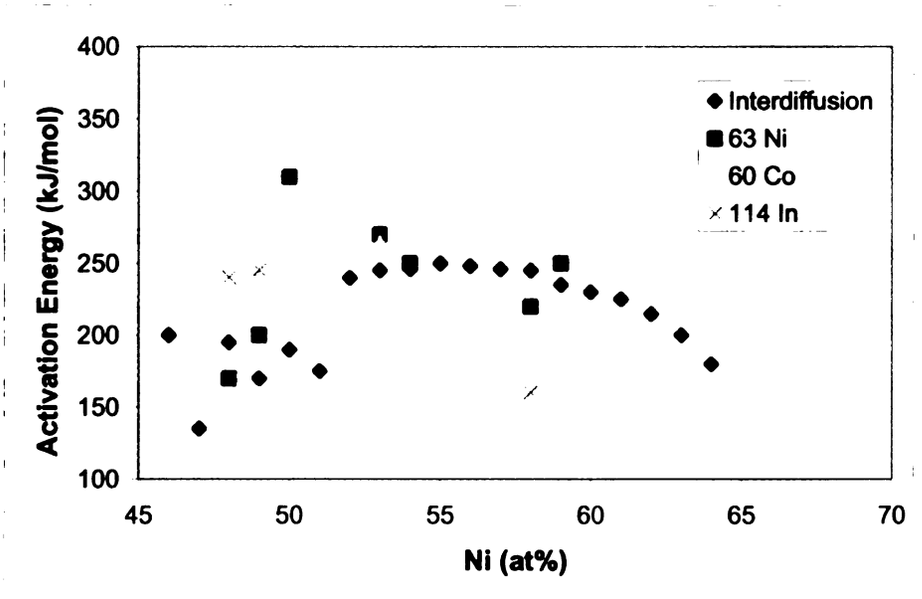


(b)

Figure 8. Diffusion coefficients (a) and activation energy (b) for diffusion of various species in NiAl as a function of stoichiometry [7]

vacancies.

and 265 k.

activation

(140 kJ mo

suggest tha

[90], which

2.4 Creep

The

creep rate is

creep-rate (

activation en

where K is

antiphase b

temperature

suggested t

activation e

activation en

The

stoichiometr

by a short p

NiAl is not

single phase

vacancies. Figure 8 b shows that the average activation energy lies in the range of 185 and 265 kJ/mol and does not vary widely with composition. These observations of activation energy do not conform to the independent energy calculation for formation (140 kJ/mol) and migration of vacancies (~160 kJ/mol) [7]. The sum of these two values suggest that the activation energy for diffusion in NiAl should be closer to 300 kJ/mol [90], which implies short-circuit diffusion that was not captured in the earlier models.

2.4 Creep

The creep properties of NiAl are not strongly dependent on stoichiometry and the creep rate is uniform in the composition range of 45 and 52% Al [7]. The steady state creep-rate ($\dot{\varepsilon}$) is expressed [6] as a function of applied stress ($\sigma$), stress exponent (m) and activation energy ($\Delta Q_C$) of creep:

$$\dot{\varepsilon} = K\sigma^m \left[\exp(-\Delta Q_C / RT)\right]$$

where K is a constant associated with microstructural effects and stacking fault or antiphase boundary energies, R is the universal gas constant and T is the absolute temperature. The activation energy for the creep of near stoichiometric NiAl has been suggested to be a function of stress, temperature and composition and the average activation energy for creep in NiAl is ~314 kJ/mol [7]. This is in close agreement with activation energy measured in some diffusion experiments [89, 90].

The steady state or secondary creep region is observed between 1000 to 1300 K in stoichiometric NiAl single crystals and non-stoichiometric polycrystals that is preceded by a short period of normal primary creep [6, 51]. Information about tertiary creep in NiAl is not conclusive. Two-phase alloys of NiAl are reported to be stronger than the single phase NiAl alloys in creep and stress rupture [1, 91].

Str

much infer

carbon (~1

creep stren

precipitatio

decrease th

Mic

commonly

developed n

($10^{-7}$ $cm^{-2}$) v

{001} and {

pencil glide

a<001> disl

deformation

dislocations

1100 K, wh

and 1300 K;

2.5 Environ

NiAl

based high

$Al_2O_3$ scale

resistance of

the steady st

Stress-rupture values of binary NiAl along an <110> axis and of polycrystals are much inferior to those of Ni-based superalloys [6]. External factors, like addition of carbon (~420 ppm), significantly decrease the activation energy of creep and thus the creep strength [92]. The creep rate above ~1000 K is significantly affected by precipitation of vacancy/impurity complexes [93]; substitutional additions like iron decrease the steady state strain rate [94].

Microstructural features such as dislocation tangles, dipoles, and loops are commonly observed in creep-deformed materials [51, 95, 96]. Above 1200 K well developed networks and subgrain formation takes place and the dislocation density is low ($10^{-7}cm^{-2}$) within the subgrains [94, 95]. Extensive cross-slip is evidenced between {001} and {110} slip planes [95, 96]. Deformation in 'soft' single crystals takes place by pencil glide of $a$<001> screw dislocations between 748 K and 1048 K; presence of $a$<001> dislocation loops are supposed to be a result of double cross-slip [6, 96]. Creep deformation in hard orientated single crystals occurs by the motion of $a$<110> dislocations [51]. Diffusion of Al plays a major role in the climb of dislocations below 1100 K, while deformation of NiAl is controlled by dislocation climb between 1100 K and 1300 K; viscous glide or solute drag becomes operative above 1500 K [6].

## 2.5 Environmental Resistance

NiAl is highly resistant to oxidation and this property is utilized to develop NiAl-based high temperature coatings for Ni-base superalloys [7]. Formation of protective $Al_2O_3$ scale and growth of the oxide films at high temperature gives rise to oxidation resistance of NiAl. There is a transient growth stage during build-up of the scale before the steady state region sets in under isothermal conditions. Transition oxides like NiO

and NiAl$_2$(

rate of Al$_2$(

and the typ

oxidation i

when the al

NiA

difference

spallation [

and thus th

conditions.

previously r

[7]. Rare e

alloys [99].

This

NiAl at roo

rather a lack

strain-aged

deformation

concentratio

reinforces th

and $NiAl_2O_4$ form during the transient stage and at lower temperatures when the growth rate of $Al_2O_3$ is slow [97]. The growth rate of the $Al_2O_3$ scales follows a parabolic curve and the type of the scale ($\theta$-$Al_2O_3$ or $\alpha$-$Al_2O_3$) depends on the temperature [7]. Rate of oxidation is a function of alloy chemistry and the rate reduces by an order of magnitude when the aluminum concentration is increased from 42 to 50 wt% [98].

NiAl performs satisfactorily for the cooling portion of cyclic oxidation when difference in thermal contraction coefficients of metals and oxides results to scale spallation [7]. The spalling induced damage increases with increasing number of cycles and thus the lifetime is shorter during cyclic oxidation in comparison to isothermal conditions. Continued cyclic oxidation results in Al depletion and as a consequence previously mentioned transition oxides (NiO and $NiAl_2O_4$) form leading to shorter lives [7]. Rare earth elements are reported to improve the oxidation resistance of NiAl based alloys [99].

## SUMMARY

This background information suggests that the limitation in plastic deformation in NiAl at room temperature is not necessarily a consequence of a lack of dislocations, but rather a lack of mobile dislocations. Dislocations may be pinned by interstitial atoms in strain-aged single crystals, resulting in insufficient mobile dislocations for plastic deformation. Observation of extensive elongation in high purity single crystals (lower concentrations of impurities than in commercially/conventionally pure materials) further reinforces this concept. Similarly, improved ductility in micro-alloyed single crystals

may reflec

decrease in

Stu

are the m

found to sl

these two s

on {110} p

energy cons

satisfy Von

materials.

resulted in i

be too high

Desp

ductility enh

this relation

*in-situ* tens

separately c

found that

dislocation

polycrystall

mobile in a

observed th

systems. In

may reflect gettering of interstitials. In pre-stressed polycrystalline materials, the decrease in flow stress results directly from an increase in mobile dislocation density.

Studies of dislocations and slip systems in NiAl suggest that <100> dislocations are the most commonly observed dislocations. These <100> dislocations have been found to slip on {110} and {001} planes [6,7]. The critical resolved shear stresses of these two slip systems are also similar. Sometimes <110> dislocations are also observed on {110} planes when dissociation into two <001> dislocations is not expected due to energy considerations. <111> slip has received considerable attention for its capability to satisfy Von Mises criterion requiring five independent slip systems in polycrystalline materials. But irrespective of the method of generation, <111> dislocations have never resulted in increased plasticity. The critical resolved shear stress for <111> slip may also be too high to cause yielding prior to fracture.

Despite the fact that the interrelationship between dislocation mobility and ductility enhancement is clearly suggested in some studies, no systematic investigation on this relationship has been carried out. In order to study the dislocation mobility in NiAl, *in-situ* tensile deformation and hardness indentation studies have been carried out separately on polycrystalline and single crystal materials. Baker et al. [100, 101] have found that slip in NiAl is wavy and the ease of cross-slip leads to the formation of dislocation cell structures at higher strains during *in-situ* tensile deformation of polycrystalline NiAl. Morris et al. [102] have observed that only <001> dislocations are mobile in a variety of single crystals. In binary NiAl and NiAl-Hf alloys they have observed that a majority (70%) of the dislocations correspond to <100>{110} slip systems. In NiAl-Fe alloys, only 30% of observed dislocations are <100> type and the

majority (

<111> disl

found to be

Ho

purity and

which disl

affects the

ductility or

yet to be ful

The

in order to

would be

degrees of

of single

compositio

majority (65%) are <111> type dislocations. In contrast to <100> mobile dislocations, <111> dislocations, which are activated near crack tips as a consequence of straining, are found to be immobile.

However, none of these studies have directly observed the influence of alloy purity and strain aging on dislocation generation and mobility in NiAl. It is not clear which dislocations are susceptible to strain aging or in what manner the strain aging affects the ability to generate mobile dislocations. The role of pre-stressing in achieving ductility or generating mobile dislocations that are immune to subsequent strain aging is yet to be fully understood.

The present study would use two different purity levels of the NiAl single crystals in order to understand the role of impurities on dislocation behavior. The single crystals would be cooled with different rates from elevated temperatures to induce different degrees of strain aging. Also, different stress axes would be used to assess the influence of single crystal orientation. Dislocations would be characterized as a function of composition, orientation and cooling rate.

Thc

(TEM) an

understand

crystals. Th

commercial

influence o

the use of

different de

the cooling

Hig

while conv

Engines.

differences

single crys

Ca

single cry

surface. T

crystal.

carbon re

were grou

was 80 pp

# 3.0 EXPERIMENTAL PROCEDURE

The present study, which uses conventional transmission electron microscopy (TEM) and *in-situ* TEM approaches, has been undertaken to achieve a better understanding of the dislocation processes critical in enhancing plasticity in NiAl single crystals. The effect of interstitial impurities was studied by comparing the deformation of commercially/conventionally pure (CP) and high purity (HP) single crystals. The influence of single crystal orientation on deformation processes was investigated through the use of differently oriented single crystals. The effect of cooling rate in imparting different degrees of strain aging was characterized by adopting different cooling rates in the cooling cycle.

High purity single crystals were provided by Dr. V. I. Levit, University of Florida, while conventionally pure single crystals were provided by Dr. R. Daroila, G. E. Aircraft Engines. Chemical analyses* of the as-received single crystals revealed significant differences in the carbon concentrations between high and conventional purity NiAl single crystals (Table II).

Carbon concentration varied to a large degree within the same sample in the CP single crystals. A concentration as high as 272 ppm was recorded on a sample near the surface. This may not be a true representative of the bulk carbon content of the single crystal. Probably the EDM fluid used for cutting the chemical analysis sample left carbon residue on the surface. Later on, all the surfaces in contact with the EDM fluid were ground before performing the chemical analysis, and the resulting average value was 80 ppm. No appreciable differences in silicon or oxygen levels were found between

| Single |
| --- |
| Commerc |
| High |

*Analysis

Cleveland,

LS) was us

DR) was us

Table II. Impurity Concentration of the NiAl Single Crystals

| Single Crystals | Si (Wt%) | O (ppm) | C (ppm) |
|---|---|---|---|
| Commercial Purity | <0.001 | 380 | 79 - 272 |
| High Purity | <0.001 | 160 | 32 |

*Analysis was carried out at National Scientific Laboratory, (1-800-497-6752), Cleveland, Ohio. For carbon analysis, a Leco carbon/sulfur determinator (Model CS-444 LS) was used, while a Leco nitrogen/oxygen simultaneous determinator (Model TC-436 DR) was used for oxygen.

the comm

3.1. Therm

Singl

a high-spe

commercia

Centorr va

alumina cr

requiremen

during anne

mechanical

following th

within the f

were 0.1 K

cooling (FC

A f

reheated to

(Lindberg).

samples we

cooling rat

within the

with Hack

The therma

the commercially pure and the high purity single crystals.

3.1. Thermal Treatments

Single crystals were cut into rectangular pieces of 6.5 mm X 6.5 mm X 20 mm using a high-speed diamond-blade wafering saw. To homogenize the single crystals, both commercially pure and high purity NiAl single crystals were annealed at 1600 K in a Centorr vacuum furnace for 48 hours. The single crystals were placed in a recrystallized alumina crucible for heat treatment. The rate of heating was adjusted with the vacuum requirements of the furnace used for the homogenization anneal. The final pressure during annealing was $10^{-6}$ mm of Hg. In order to study the influence of cooling rate on mechanical behavior, different cooling rates were imposed on the single crystals following the homogenization anneal treatment. Accelerated cooling was accomplished within the furnace using flowing argon. The imposed cooling rates on the single crystals were 0.1 K/s and 1 K/s and are subsequently referred in the text as slow or furnace cooling (FC) and fast or air-cooling (AC) respectively.

A few selected samples of commercially pure material were subsequently reheated to elevated temperatures (473 K and 673 K) in a resistance type muffle furnace (Lindberg). The samples were contained in an alumina crucible with a covered lid. The samples were cooled inside the furnace (FC) and out of the furnace (AC) to vary the cooling rate. For air-cooling, the samples were placed outside of the furnace but still within the alumina crucible. The heat treatment schedules were adopted in accordance with Hack et al. [18, 19] to have embrittled (FC) and toughened (AC) single crystals. The thermal treatment process is schematically illustrated in figure 9.


Figure 9.
Hack et al.

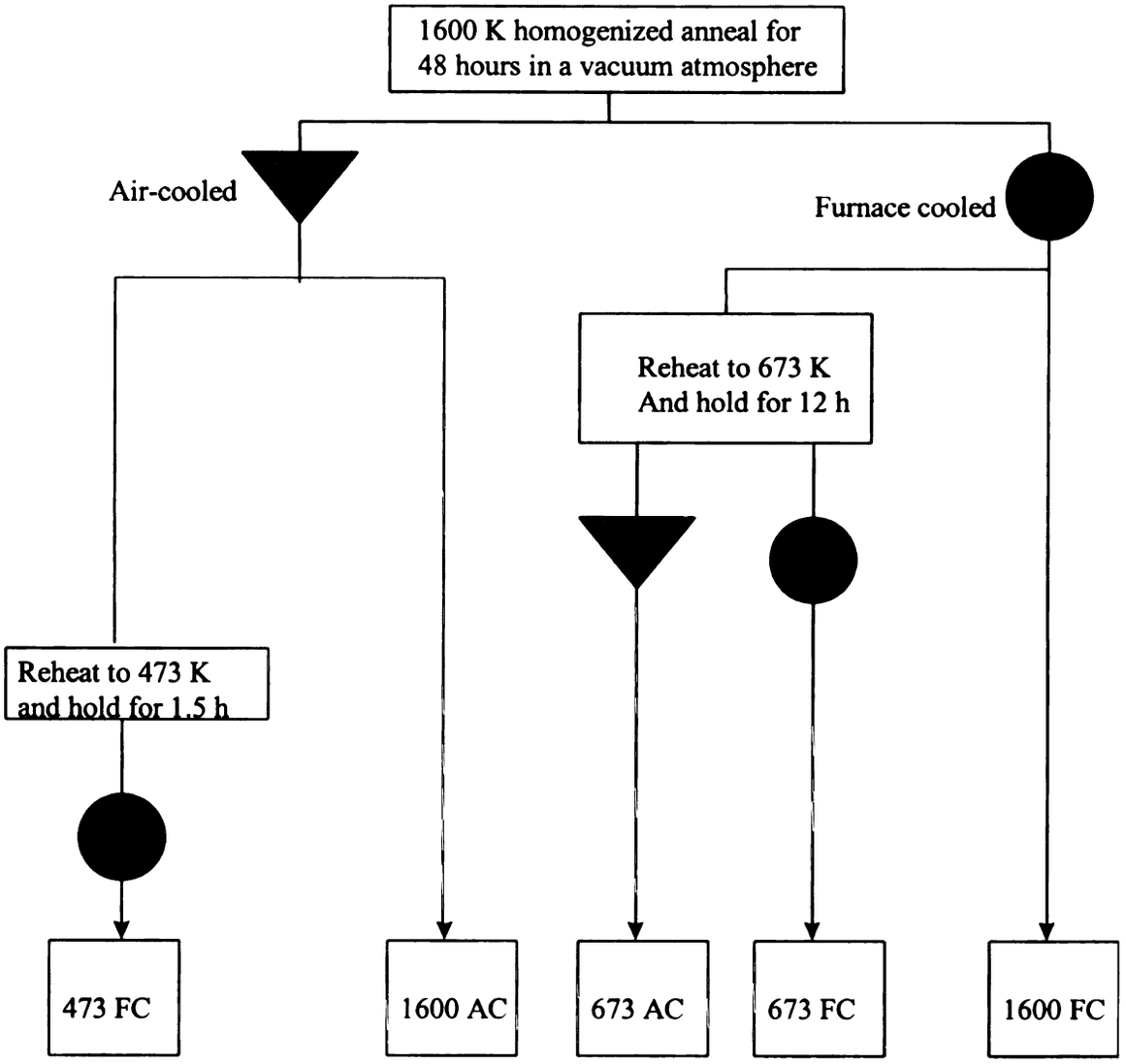


Figure 9. Schematic representation of the thermal treatment process in accordance with Hack et al. [18, 19]

3.2 Compr

Sel

were subje

were groun

0.3 μm Al

electrolytic

was contai

crystal bar

liquid nitr

continuousl

found to be

Orie

diffraction t

of 40 kV an

<001>, and

3.3 Compre

The

temperature

load-cell. C

during initi

loading or b

to an appro

approximate

3.2 Compression Sample Preparation

Selected specimens from both commercially pure and high purity single crystals were subjected to compressive deformation after thermal treatments. Single crystal bars were ground through 600 grit using SiC grinding paper and further hand polished using 0.3 μm $Al_2O_3$ polishing media. These bars were then electropolished at 243 K using an electrolytic solution of one part of nitric acid and two parts of methanol. The solution was contained in a stainless steel beaker, which was used as the cathode, and the single crystal bar was used as the anode. The temperature of the bath was maintained by adding liquid nitrogen periodically on the top of the electrolyte, which was being stirred continuously by a magnetic stirrer. The applied potential for optimum polishing was found to be 12 V.

Orientations of the single crystals were determined by back-reflection Laue X-ray diffraction technique using a Seifert X-ray device operated with an acceleration voltage of 40 kV and tube current of 30 mA. Single crystals were oriented to 'soft' <110>, 'hard' <001>, and some arbitrary orientations within the stereographic triangle (figure 10).

3.3 Compression Deformation

The polished and oriented specimens were then deformed in compression at room temperature using an Instron (Model # 4206, Serial # 630) load-frame with a 100 kN load-cell. One-inch diameter steel compression pads were used and precaution was taken during initial contact of the compression pads with the sample to avoid asymmetric loading or buckling. The applied crosshead speed was 0.06 mm/min, which corresponds to an approximate strain rate of 4.4 X $10^{-5}$ /sec. The specimens were deformed to approximately 2.5% plastic strain to induce dislocation generation and slip.

001

Figu

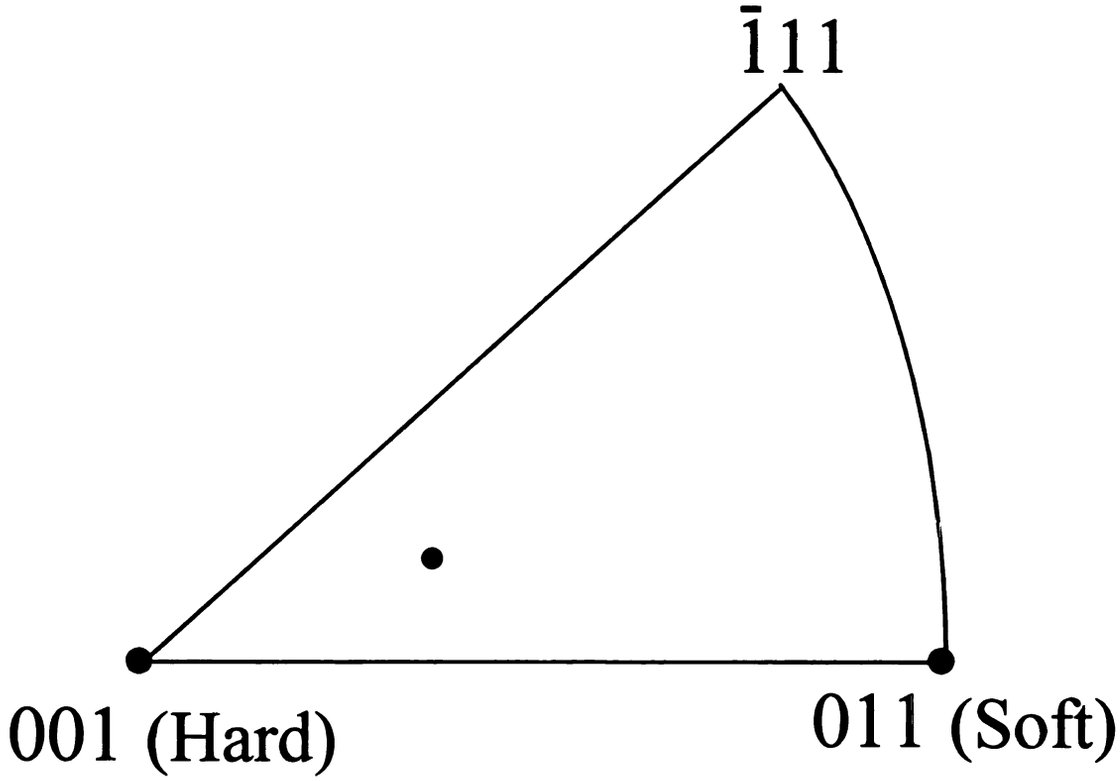


Figure 10. Orientation of the specimen within the stereographic triangle

3.4 TEM

A

technique

operated a

normal w

cutting 3

parallel to

abrasive p

adjustable

The

jet polisher

methanol v

A. The pu

3 in course

foils as th

thinning op

storing for

Tra

H-800 (Se

200 kV. I

dislocation

In order to

primary sp

## 3.4 TEM Sample Preparation

At this point the bars were cut into 3 mm diameter rods by spark-erosion technique using a Materials Science NW MK 2 Electro Discharge Machine (EDM) operated at 200 V. The rods were cut using a tube in an inclined way i.e. the slip plane normal was made parallel to the cylinder axis. Thin foil specimens were prepared by cutting 3 mm diameter discs from the rod by wire-EDM. The slices were sectioned parallel to the slip plane. The discs were then thinned by hand grinding using SiC abrasive papers to a thickness of approximately 200 μm. A steel grinding-ring with adjustable depth was used as an aid for thin sample grinding.

The specimens were subsequently electropolished at 243 K using a Struers Twin jet polisher (Tenupol 3) in a solution of freshly prepared one part nitric acid and two parts methanol with an applied potential of 12 V and a resulting current of approximately 0.15 A. The pump speed was controlled during electropolishing by gradual decrease from 7 to 3 in course of the polishing. This precaution was taken to minimize any damage to the foils as the foils became thinner. The specimens were cleaned thoroughly after the thinning operation by fast dipping and rinsing in methanol at least three times before then storing for microscopic observation.

Transmission electron microscopic observations were carried out using a Hitachi H-800 (Serial number 800-17-02) microscope operated with an accelerating voltage of 200 kV. Dislocations were observed using brightfield and weak-beam imaging. Initial dislocation Burgers vectors were determined using the $\mathbf{g}\cdot\mathbf{b} = 0$ and $\mathbf{g}\cdot\mathbf{b} \times \mathbf{u} = 0$ criteria. In order to perform a complete contrast analysis, all of the available *g*-vectors from the primary spots of three poles, commonly {001}, {110} and {111} were utilized. Two

beam co

reflection

dislocatio

3.5 Image

D

dislocatio

condition

weakest c

further cor

and true

determinin

using the c

The

essentially

and these s

Following

the unknow

vectors tak

and their c

crystallogr

micrograph

Kikuchi lir

vector **g** fo

beam conditions were set up with regular lattice spots excluding any superlattice reflections and thus avoiding any further complications in interpretation of broad dislocation images with large extinction distance.

3.5 Image Simulation

Due to high elastic anisotropy of NiAl, all of the planes around an edge or screw dislocation are distorted; it was not always easy to achieve perfect invisibility even under conditions of $\mathbf{g}\cdot\mathbf{b} = 0$ and $\mathbf{g}\cdot\mathbf{b} \times \mathbf{u} = 0$. Thus, the invisibility criterion often used as the weakest contrast rather than complete invisibility of the dislocations. The situation gets further complicated as most of the dislocations are neither pure edge nor pure screw type and true invisibility is very difficult to achieve experimentally. Ambiguity in determining the Burgers vectors of the dislocations was resolved by image simulation using the computer program developed by Head et al. [103].

The computer program is based on the dynamical theory of image contrast and essentially an image matching technique. A series of dislocation images are generated and these simulated images are matched with the experimental image of any dislocation. Following is the method of identifying the dislocations. Experimental micrographs of the unknown dislocations are taken under different diffracting conditions i.e. different 'g' vectors taken in different electron beam directions. For accurate simulation, micrographs and their corresponding diffracting patterns need to be collected in such a way that the crystallography of the defect and of the foil, as well as the diffracting conditions for each micrograph, can be specified as completely as possible. It is important to recognize the Kikuchi line patterns for the low index reflections. Important data includes diffracting vector **g** for each micrograph, the beam direction **B**, the dislocation line direction **u**, the

foil norm

Methods

Ir

images a

observed

micrograp

with diffi

such com

part of his

3.6 *In-situ*

TE

machining

tensile spe

wide slice

correspond

optimized

of less tha

was found

Th

kept little

long and t

Then the 2

electrode i

foil normal **F**, foil thickness **t**, and a value of the deviation from the Bragg condition, **w**. Methods of determining the above parameters are followed from Head et al. [103].

Informed guesses are then made about the unknown dislocations and theoretical images are computed under the same diffracting conditions as the experimentally observed image. The defect is identified when the theoretical and experimental micrographs match consistently under different imaging conditions. Dislocation images with different topological characteristics or distinguishable features are most suitable for such comparison. This part of the work was carried out in conjunction with B-C. Ng as a part of his Master's thesis [104].

3.6 *In-situ* Tensile Straining

TEM tensile samples for *in-situ* straining were fabricated by electro discharge machining to conform to a Hitachi H-5001 T tensile stage. A schematic diagram of these tensile specimens is shown in Figure 11. At first a 1 mm thick, 15 mm long and 5 mm wide slice was cut by wire-EDM, making sure that the tensile axis of the specimen corresponds to the specific orientation of the single crystal. The initial thickness was optimized for subsequent handling and machining. It was found that a starting thickness of less than 1 mm was not able to sustain handling and some non-uniformity in thickness was found from one end of the sample to the other after grinding.

The starting thickness for subsequent preparation and mechanical grinding was kept little more than 1 mm. The gage lengths of the samples were approximately 3 mm long and the gage-area was first created by Electro Discharge Machine profile cutting. Then the 2 mm diameter loading holes were created by using a copper wire-rod as the electrode in the EDM.

Tensile

Figur

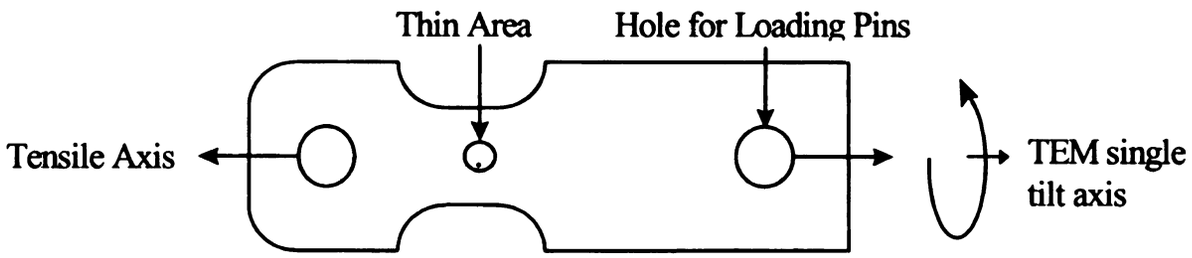


Figure 11. Schematic of the 15 mm long and 5 mm wide *in-situ* tensile specimen

T

rounded

specimen

using Si

grinding.

samples.

of any s

mentioned

El

tensile sp

methanol

mentioned

generating

were scra

Tenupol

during loa

of the sp

methanol

observati

*In*

The driv

observati

until any

The sharp edges at one end of the specimen (the left-hand side of figure 14) were rounded by hand grinding to fit in the tensile stage of the microscope. The tensile specimens were subsequently hand ground to a final thickness of approximately 150 μm using SiC abrasive paper. Masking tape and double-sided tapes were used to assist grinding. The tape was wrapped on the fingers before grinding to prevent slippage of the samples. The specimens were subjected to a quick electropolish to minimize the effects of any surface flaw or contamination due to grinding using the same conditions mentioned in section 3.2.

Electron transparent thin areas were then created within the gage length of the tensile specimens by careful twin-jet electropolishing in a freshly prepared solution of methanol and nitric acid (2:1) following the same steps, equipment and conditions mentioned in section 3.4. Sometimes the specimens slipped during electropolishing generating a hole that was not located centrally within the gage length. These specimens were scrapped. As the gripping of the tensile specimens within the sample holder of the Tenupol twin-jet polisher is essentially by mechanical contact, precautions were taken during locking the two male-female parts of the sample holder to keep only the gage area of the specimens exposed to the electrolyte. The specimens were thoroughly rinsed in methanol (as mentioned in section 3.4) following electropolishing prior to TEM observation.

*In-situ* straining experiments were carried out in the same Hitachi H-800 TEM. The drive for azimuthal rotation was utilized for tensile straining. The whole area of observation was mapped prior to any straining. The straining was started very slowly until any noticeable dislocation motion was observed. Dislocation activity and the

mobile d

wide-ang

HS-U28(

straining

due to in

areas of t

Sc

length an

failure of

Ur

diffracting

during *in-*

not possib

carried ou

motion.

dislocatio

bottom o

direction

plane of t

3.7 *In-sit*

In

dislocati

could on

mobile dislocations generated by *in-situ* straining were recorded dynamically using a wide-angle CCD camera (Gatan 673-0200) and a VHS videocassette recorder (Mitsubishi HS-U28), while static images were recorded with the TEM plate camera. Further tensile straining was continued until the mobile dislocations were observed to cease their motion due to interaction with pile up of dislocations. Mobility of dislocations in the thicker areas of the specimen was also difficult to follow and record.

Sometimes cracks opened up from the thinning hole in the middle part of the gage length and the specimens failed during straining. Attempts were made to avoid the failure of the strained samples for subsequent static observation.

Unfortunately the TEM tensile stage has only one tilt axis available to vary diffracting conditions, making it impossible to obtain variety of diffracting conditions during *in-situ* straining. Thus, complete characterization of the mobile dislocations was not possible. However, limited analysis of dislocation line directions and slip planes was carried out based on slip trace analysis of the observed slip lines following dislocation motion. Dislocation motion was evidenced with slip trails left in the wake of the dislocations. These trails are the consequence of the dislocations disturbing the top and bottom of the surface oxide layer on the foils as they pass. Inference on the line directions of dislocations was based primarily on the dislocations lying normal to the plane of the foil.

3.7 *In-situ* Tensile Deformation of Disc Samples

In order to determine the Burgers vectors and line directions of the mobile dislocations, it was necessary to utilize a wide variety of diffracting conditions, which could only be accomplished by using a double-tilt specimen holder. Those specimen

holders a

requirem

the gage

TEM. A

to mecha

the EDX

paramete

use a diar

kept at su

the sampl

W

specimen

specimens

control th

as avoidir

almost im

interest of

damage to

Fi

help of lo

microscop

tilt specim

this way t

holders are designed to accommodate 3 mm diameter disc specimens only. To meet the requirements of the double-tilt specimen holders, several attempts were made to extract the gage-length section of the 15 mm long specimens after tensile deformation in the TEM. At first, tube EDM was used to cut a 3 mm diameter disc from the gage area. Due to mechanical vibration involved in cyclic pulse, the thin areas fractured and were lost in the EDM bath during spark erosion. All kinds of manipulation with the operating parameters could not retain the electron-transparent part within the disc. Next attempt to use a diamond core-drill was also unsuccessful, as the mechanical vibrations could not be kept at such a low level so that the thin section remained adhered with the main-body of the sample.

When all those attempts to remove the deformed thin areas from the tensile specimen failed, an alternate approach was taken to deform a 3-mm disc specimen. Disc specimens were prepared and glued to the tensile stage. Difficulty was experienced to control the amount of glue to ensure enough mechanical strength during straining, as well as avoiding masking the electron-transparent section by the glue. In addition, it was almost impossible to unglue the deformed specimens without damaging the areas of interest of the test-piece. Use of solvents, like acetone, to dissolve the glue also caused damage to the foil.

Finally, 3-mm disc specimens were prepared and mechanically clamped with the help of loading screws in the tensile holder and strained in tension within the electron microscope. The same samples were subsequently observed in the TEM using the double tilt specimen holder keeping in conformance with the positioning in the tensile stage. In this way the mobile dislocations were easily characterized in relation to the dislocations

generat

availabl

criteria t

generated during tensile deformation. Thus, a full range of reflecting conditions were available and complete contrast analysis was performed using $\mathbf{g} \cdot \mathbf{b} = 0$ and $\mathbf{g} \cdot \mathbf{b} \times \mathbf{u} = 0$ criteria to determine the line directions and Burger's vectors of the mobile dislocations.

The me
obtaine
fracture
crystals
are pres
Ni-Al si
T
single c
crystal
induced
tempera
followe
and disl
T
statically
CCTV c
Some re
presente
example
complete

# 4.0 **EXPERIMENTAL RESULTS**

The results of the experiments outlined previously are presented in this section. The mechanical behavior of the single crystals is presented first. Yield stress properties, obtained by compression tests of the commercially pure materials, are compared with the fracture toughness properties determined by Hack et al. [18, 19] for similar single crystals. Then the results of post-deformation or static transmission electron microscopy are presented before going into the details of *in-situ* transmission electron microscopy of Ni-Al single crystals.

The evolution of dislocation substructures in commercially pure undeformed single crystals is presented as a function of thermal treatments. Undeformed single crystal results are followed by results from deformed specimens. The deformation induced dislocation sub-structures are presented in relationship to the reheating temperature and variation in cooling rate. Commercial purity single crystals results are followed by the results from the high purity materials where the mechanical properties and dislocation sub-structures derived from compressive deformation are presented.

This post mortem study is followed by *in-situ* tensile deformation, where statically captured images for dynamic movement of dislocations are presented. A CCTV camera was used to record the dislocation motion at the onset of deformation. Some representative clippings (with a span of 64 minutes) from these recordings are presented in the form of digital video disk (DVD) and included in the Appendix. A few examples of dislocation image simulations are included also for the sake of achieving completeness in dislocation characterization. The last part of the results includes the *in-*

*situ* de

crystal

using a

4.1 Mec

4.1.1 C

values a

values o

[18, 19].

indicate t

in fractur

in a con

intermed

attributec

Discussio

history, t

4.1.2 Co

T

NiAl sin

temperatu

especially

yield stre

lower cor

*situ* deformation of 3-mm disc specimens in a single-tilt holder from high purity single crystals and observation of the same post deformation dislocation substructures in TEM using a double tilt specimen holder.

## 4.1 Mechanical Behavior

### 4.1.1 Compression deformation of commercially pure single crystals

The results of the compression tests are presented in Table III. The yield stress values at different thermal treatment conditions are compared with the fracture toughness values of similarly treated commercially pure NiAl single crystals obtained by Hack et al. [18, 19]. Figure 12 shows the trends of these two mechanical properties. The results indicate that slower cooling rates increase the yield stress with a corresponding decrease in fracture toughness. Conversely, faster cooling rates decrease the yield stress and result in a concurrent increase in fracture toughness. Reheating the single crystals to an intermediate temperature revealed significant impact on the final properties. This may be attributed to the so-called strain aging effect that will be discussed at greater length in the Discussion chapter (5.0). It is also observed that, irrespective of the previous thermal history, the final cooling rate strongly influences the mechanical properties.

### 4.1.2 Compression deformation of high purity single crystals

Table IV lists the yield-stress values for furnace-cooled and air-cooled high purity NiAl single crystal samples. These single crystals were not treated at intermediate temperatures like commercial purity materials as the influence of thermal conditions especially cooling rate was not that significant in altering the tensile properties. The yield stress values, determined by compression tests for high purity single crystals, are lower compared to similarly treated commercially pure material.

Table

| Spec |
| --- |
| 473 |
| 1600 |
| 673 |
| 673 |
| 1600 |

*Ad

Table III. Comparison of yield stress obtained by compression test of commercially pure NiAl single crystals with fracture toughness. *

| Specimen | Thermal History | Yield Stress (MPa) | Fracture Toughness MPa$\sqrt{m}$* |
|---|---|---|---|
| 473 FC | 1600 K homogenization anneal and fast-cooled. Reheated to 473 K and slow-cooled. | 400+/-12 | 2.8 |
| 1600 AC | 1600 K homogenization anneal and fast-cooled. | 200+/-8 | 15.6 |
| 673 AC | 1600 K homogenization anneal and slow-cooled. Reheated to 673 K and fast-cooled. | 153+/-5 | 16.7 |
| 673 FC | 1600 K homogenization anneal and slow-cooled. Reheated to 673 K and slow-cooled. | 361+/-6 | 5.8 |
| 1600 FC | 1600 K homogenization anneal and slow-cooled. | 450+/-10 | 2.4 |

*Adapted from Hack et al. [18, 19]

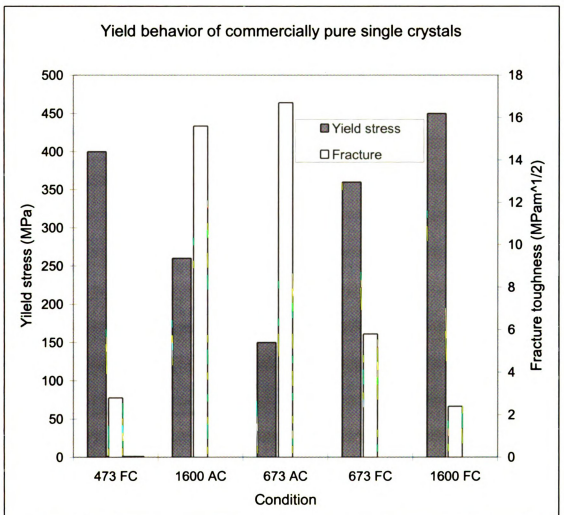


Figure 12. Change of yield stress and fracture toughness (Per Hack et al. [18, 19]) with thermal history. The inverse relationship of yield stress and fracture toughness may be noted.

Table IV. Yield stress properties obtained by compression test of high purity NiAl single crystals

| Specimen | Thermal History | Yield Stress (MPa) |
|---|---|---|
| 1600 AC | 1600 K homogenization anneal and fast-cooled. | 142+/-10 |
| 673 AC | 1600 K homogenization anneal and slow-cooled. Reheated to 673K and air-cooled. | 135+/-7 |
| 673 FC | 1600 K homogenization anneal and slow-cooled. Reheated to 673K and slow-cooled. | 274+/-9 |
| 1600 FC | 1600 K homogenization anneal and slow-cooled. | 287+/-5 |

4.2. Slip Trace Analysis

Slip lines were observed using optical microscopy and the active slip planes were determined by slip trace analysis following the method described by Barret [105]. Figure 13 shows an example of slip lines developed on two perpendicular faces of a deformed single crystal. The angles $\alpha$ and $\beta$ were measured on the micrographs taken from the front and right faces of the rectangular compression specimen as shown in Figure 14. Then the angles, $\alpha$ and $\beta$, were plotted on the stereographic projection of the front face in the way as shown in figure 15. The two points define the slip plane, which causes the slip trace on the single crystal. The slip plane and its pole (90° from the plane) are shown on the stereographic projection. Slip was observed on {001} planes for all of the commercially pure specimens. The majority of the high purity specimens also exhibited traces from {001} planes and in some cases {110} planes. There were a few cases when limited cross-slip was observed and {112} was determined as the cross-slip plane.

4.3 Static/Post-deformation TEM Observations

4.3.1 Undeformed commercially pure single crystals

Undeformed specimens exhibited isolated and widely spaced dislocations throughout the structure, with few dislocation loops and tangles. Many observed areas had essentially no dislocations. For undeformed materials, both slow cooled and fast cooled specimens had similar dislocation densities as is evident from figure 16 for 473 FC, 673 FC and 673 AC samples respectively.

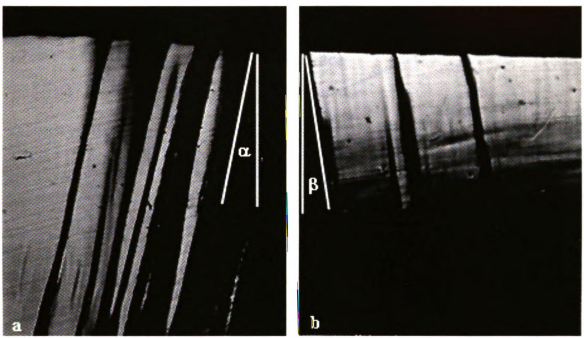


Figure 13. Two faces of a deformed specimen showing slip traces with measured angles $\alpha$ and $\beta$ on (a) front and (b) right faces respectively.

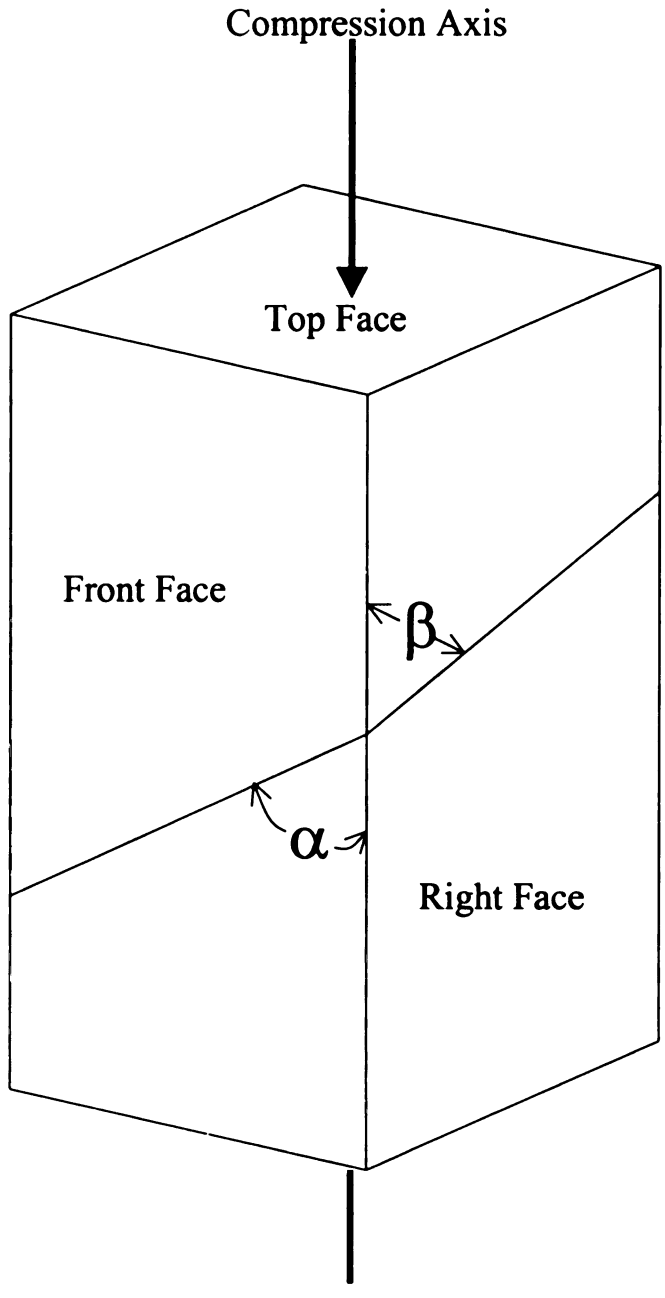


Figure 14. Schematic representation of compression sample showing the measurement of α and β used in determining the slip plane.

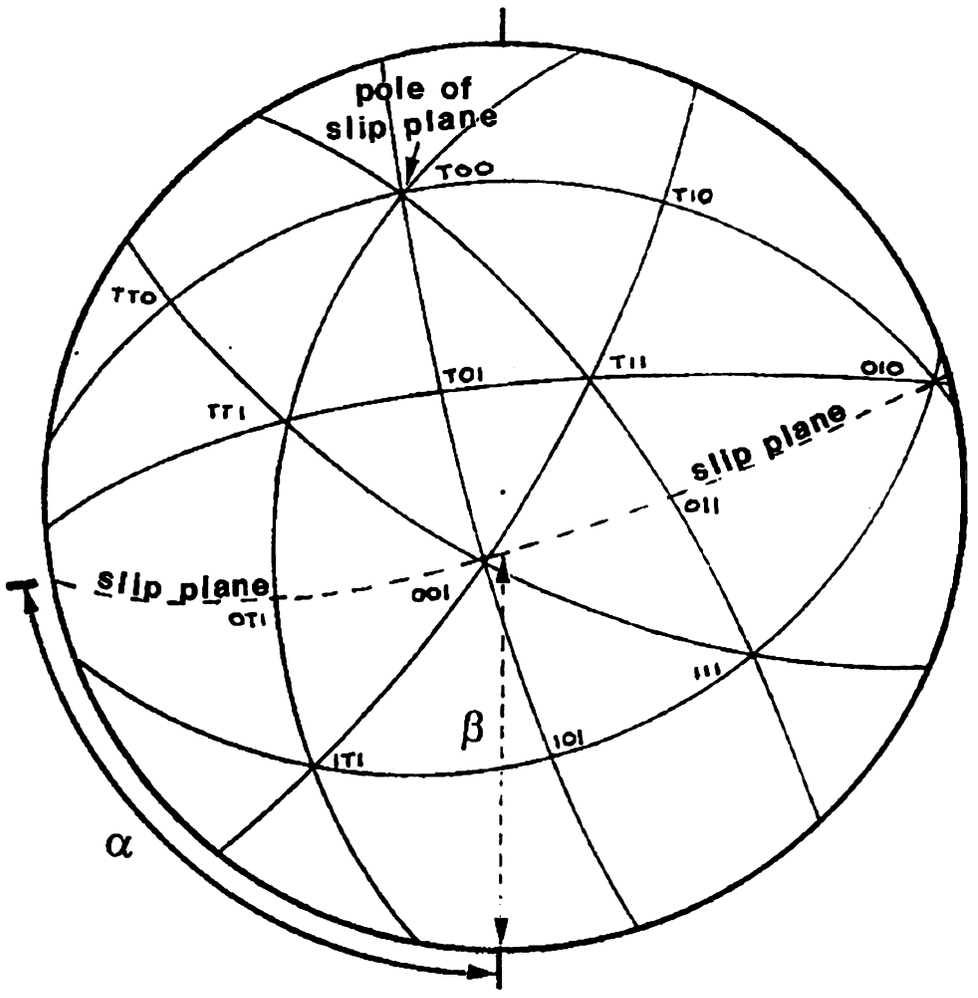


Figure 15. Stereographic projection of the single crystal compression sample shown in figure 13 displaying the plotting of angles α and β used to determine the slip plane.

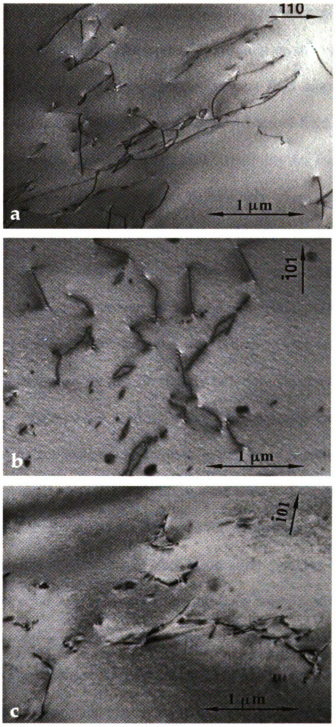


Figure 16. Isolated, widely spaced, single dislocations are observed throughout the structure of commercially pure NiAl single crystals with few dislocation loops and tangles in (a) an undeformed 473 FC specimen. (b) an undeformed 673 FC specimen and (c) an undeformed 673 AC specimen respectively.

Dislocations were characterized using the invisibility criteria; $\mathbf{g}\cdot\mathbf{b} = 0$ for screw dislocations and $\mathbf{g}\cdot\mathbf{b}\times\mathbf{u} = 0$ for edge dislocations. Depending on the values of **g**, these factors can assume a zero value signifying no displacement field around a dislocation line. A dislocation becomes invisible if there is no displacement field surrounding the dislocation. These criteria hold good with complete invisibility for isotropic materials only. The factor, $\mathbf{g}\cdot\mathbf{b}\times\mathbf{u}$ for edge dislocations, can be zero only where the line direction **u** is parallel to the diffraction vector **g**. However, NiAl is a highly anisotropic material and dislocations are often mixed in character. Thus, dislocation lines may not go completely out of contrast in many situations, even after satisfying the invisibility criterion.

The evolution of the dislocation structure was studied and the Burgers vectors of the dislocations were analyzed using this invisibility criterion. In absence of complete invisibility, the weakest contrast was used as an approximation for the out-of-contrast conditions. A series of reflections were used to set up two beam conditions with regular lattice spots. Two such reflections for invisibility were used to determine the Burgers vector **b**, which is essentially the zone axis of the two reflecting planes.

Figure 17 illustrates an example of such dislocation analyses for slow cooled undeformed 673 FC specimens. Two types of dislocations were identified as types 'a' and 'b'. Type 'a' dislocations, which remained in good contrast for the [011] reflection and visible with weak contrast for the [200] and [110] reflections respectively, were determined to have the [001] slip direction. Similarly, 'b' type dislocations observed to be in weak contrast for the [200] and [111] reflections, were determined to have the $[0\bar{1}1]$ slip direction.

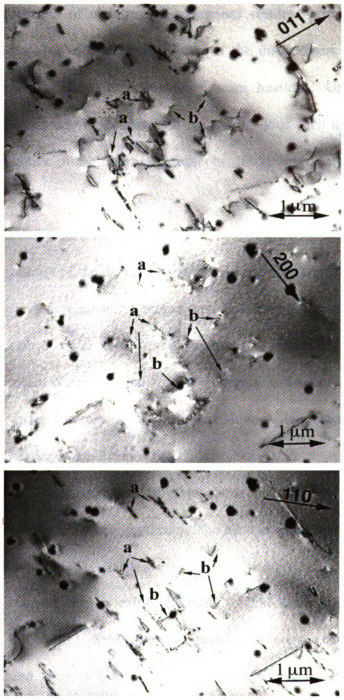


Figure 17. The same area of undeformed commercially pure 673 FC specimen is shown with different tilts giving $\bar{g}$ = [011], [200] and [110]; 'a' denotes [001] and 'b' denotes $[0\bar{1}1]$ slip directions.

All thermal treatments of undeformed specimens resulted primarily in <001> dislocations with a few <110> dislocations. Some of the dislocations in undeformed specimens were observed to move as a result of beam heating. Unlike deformed materials, no tangle of dislocation was observed and mobility of such dislocations was not constrained. Irrespective of the thermal treatments, {001} was analyzed as the slip plane in all cases.

4.3.2 Deformed commercially pure single crystals

The gross morphology of the dislocation structures differed significantly between deformed and undeformed specimens. Compression deformation resulted dislocation tangles, which were not observed in undeformed specimens. Dislocations were also seen to move as a result of beam heating which results in strains in the foil due to different thermal expansion in different areas of the foil. In slow-cooled deformed materials dislocation movement under beam heating conditions ceased as soon as the mobile dislocations interacted with the pre-existing dislocation tangles, which were already pinned by solute atoms during slow cooling through the elevated temperature region.

4.3.2.1 Slow cooled (FC) samples

Slow cooled samples, which exhibited higher yield stress than fast cooled samples, were found to exhibit dislocation structures that were heavily tangled in comparison to fast cooled samples from either the homogenization anneal temperature (1600 K) or any intermediate reheating temperature (473 K/673 K). Figures 18 - 20 presents typical dislocation structures obtained through slow cooling of 473 FC, 673 FC and 1600 FC samples that exhibited higher yield stress ($\geq$ 400 MPa) values.

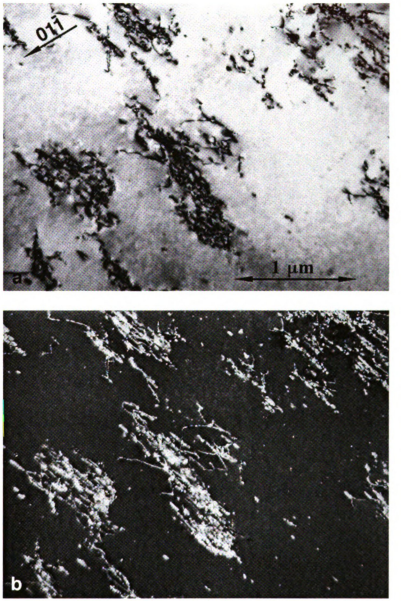


Figure 18. Heavily tangled dislocation morphology in deformed commercially pure 473 FC specimen; (a) brightfield image and (b) weak beam image.

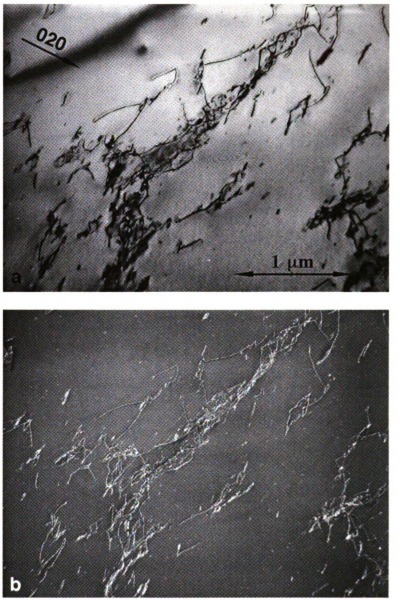


Figure 19. Deformed commercially pure 673 FC specimens reveal tangled dislocations; (a) brightfield and (b) weak beam image

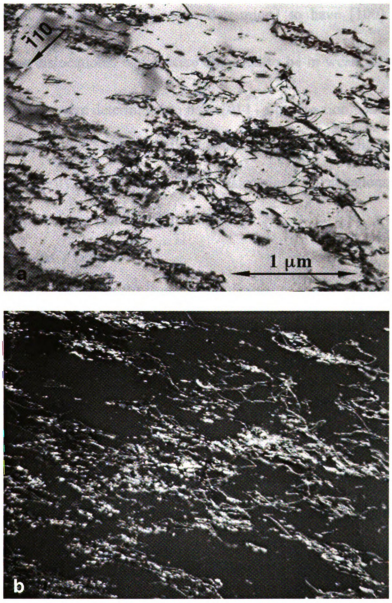


Figure 20. Deformed commercially pure 1600 FC specimens display heavily tangled dislocations in (a) brightfield and (b) weak beam image.

Figure 21 illustrates an example of dislocation analyses for slow cooled 673 K samples. Two different types of dislocations were identified as type 'a' and 'b'. Type 'a' dislocations, which remained in good contrast in (a), went in extinction for (b) and visible with residual contrast in (c), were determined to have [100] slip direction. Similarly, 'b' type dislocations, which were observed to be in weak contrast for $[\bar{2}00]$ and $[\bar{2}11]$ reflections, were determined to have $[01\bar{1}]$ slip direction. All other deformed slow cooled samples from 473 K and 1600 K were found to have both <001> and <110> dislocations, the majority of which were <001> dislocations. Dislocations were observed to move under beam heating conditions in some cases.

4.3.2.2 Fast cooled (AC) samples

A significantly different dislocation substructure was observed for deformed fast-cooled samples (AC), cooled either from 1600 K or from 673 K. Analyses of the dislocation structures are shown in figures 22 and 23 respectively. Specimens that have undergone slow cooling tend to develop dislocation tangles, while fast cooled specimens exhibited dislocations with wider separations and were sparsely entangled. In contrast to slow cooled samples, dislocations were seen to move more freely for fast cooled specimens under beam heating conditions; this may be attributed to the less intense interaction of the mobile dislocations and dislocation tangles.

Figure 24 illustrates an example of dislocation analyses for fast-cooled 673 AC specimens that possess lower yield strength than the slow cooled specimens. In this case two different types of dislocations were observed and identified as types 'a' and 'b'. Type 'a' dislocations displayed weak contrast in $[0\bar{1}0]$ and in $[0\bar{1}1]$ reflections and were

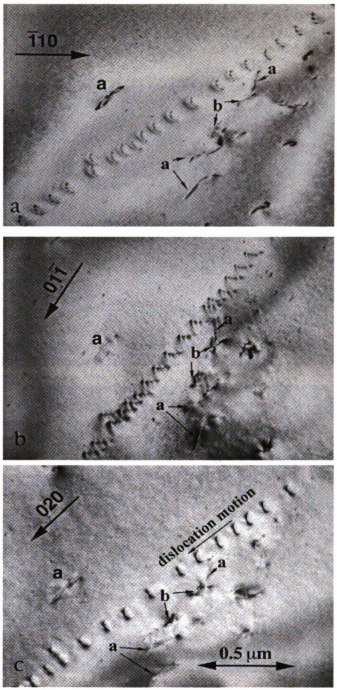


Figure 21. Commercially pure 673 FC specimen reveals presence of two different types of dislocations, **a** with **b** = [100] and **b** with **b** = [011]. The same area is shown with different operative reflections; $\bar{g}$ = (a) [$\bar{1}$10], (b) [011] and (c) [020]. Dislocations were also seen to move in (c).

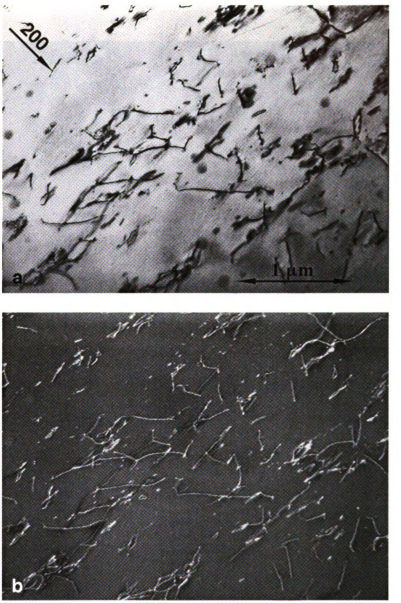


*Figure 22.* Dislocation structures observed in deformed commercially pure 1600 AC specimens; (a) brightfield image and (b) weak beam image.

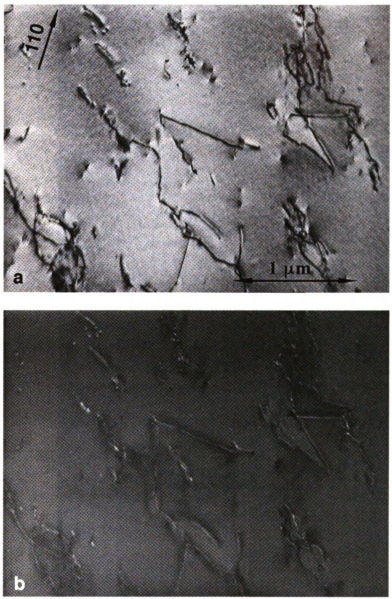


**Figure 23.** Very few dislocation tangles were observed in deformed commercially pure 673 AC specimens; (a) bright field image and (b) weak beam image.

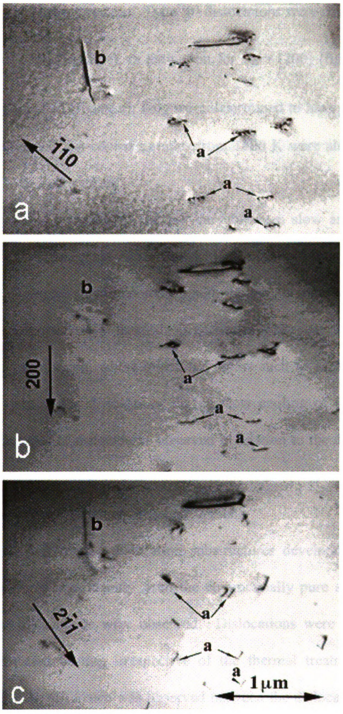


Figure 24. Commercially pure deformed 673 AC specimen shows 'a' and 'b' dislocations with **b** = $[\bar{1}00]$ and $[01\bar{1}]$ respectively. The same region with different operative reflections are shown in (a) $[1\bar{1}0]$, (b) [200] and (c) $[2\bar{1}\bar{1}]$.

determined to have the [$\bar{1}$00] slip direction. Type 'b' dislocations were observed to be in sharp contrast for $\bar{g}$ = [$\bar{1}$ $\bar{1}$ 0] (figure a), in extinction for $\bar{g}$ = [200] (figure b), and in residual contrast for $\bar{g}$ = [2$\bar{1}$ $\bar{1}$] (figure c); they were determined to have the [01$\bar{1}$] slip direction. Similarly, deformed fast-cooled samples from 1600 K were also analyzed to have both <001> and <110> dislocations.

Although the types of dislocations did not vary between slow and fast cooled samples, the differences in the gross morphology of the dislocations of deformed specimens are striking. Samples slowly cooled through the temperature window of 673 K to room temperature display heavily tangled dislocations. This observation suggests the possibility of static strain aging, where interstitial atoms such as carbon had ample time to diffuse to the core of the dislocations during slow cooling of the specimens. Table V summarizes the types of dislocations observed in relation to the thermal history of the specimens and their yield stress values.

4.3.3 Compression deformation of high purity single crystals

Post compression deformation dislocation substructures developed in the high purity single crystals differed significantly from the commercially pure single crystals. Only limited tangles of dislocations were observed. Dislocations were seen to move under the influence of beam heating irrespective of the thermal treatments prior to deformation. No discernible difference was observed between the dislocation behaviors of the specimens depending on the final cooling rate. Dislocations generated during deformation of high purity single crystals were analyzed in the same way as for commercially pure single crystals.

Table V. Burgers vectors analyses for deformed specimens in relation to their thermal histories and yield stress in commercial purity materials

| Specimens | Yield Stress (MPa) | Burgers vector b | |
|---|---|---|---|
| 473 FC | 400 | Primarily <001> | Scattered <011> |
| 1600 AC | 200 | Primarily <001> | Scattered <011> |
| 673 AC | 153 | Primarily <001> | Scattered <011> |
| 673 FC | 361 | Primarily <001> | Scattered <011> |
| 1600 FC | 450 | Primarily <001> | Scattered <011> |

Figures 25 and 26 present dislocation structures obtained through fast and slow cooling of 1600 AC and 1600 FC samples respectively. In both cases dislocations were observed to move under the influence of the beam and were characterized in reference to immobile dislocations. Figures 25 (a-d) reveals the mobile dislocations to be [001] type for fast cooled samples. A similar situation was observed for slow cooled samples, where mobile dislocations were determined to be of the [001] type, as shown in figures 26 (a-d). Dislocations lying in the plane of the foil were also found to be [001] type.

Dislocation analyses from samples subjected to intermediate reheating temperature of 673 K are presented as figures 27 and 28 respectively. Figure 27 (a-c) show $[\bar{1}01]$ dislocations for 673 AC or fast cooled samples. Although presence of <111> mobile dislocations is unlikely in NiAl, figure 28 (a-d) reveals [111] as the mobile dislocations in the 673 FC or slow-cooled samples. Overall the gross morphology of the dislocations differed significantly between the deformed microstructures of high and commercial purity single crystals, but there is not much influence of the cooling rate on the dislocation morphology in high purity single crystals. In undeformed high purity single crystals there were a few widely spaced isolated dislocations present; consequently no images are presented due to lack of value added information.

4.4 Image Simulation

As mentioned in the literature review section, due to high elastic anisotropy of NiAl it is almost impossible to obtain perfect invisibility of dislocations in NiAl single crystals. Therefore, the contrast analysis was complemented with image simulation. This section of the results describes a typical image simulation for a dislocation in a undeformed 673 AC specimen.

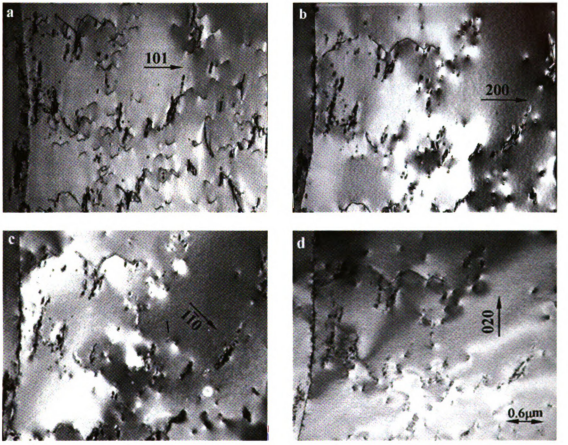


Figure 25. Dislocation analyses in high purity 1600 AC specimen shows [001] dislocations in different reflections. Dislocations that are mobile under beam heating condition appear with good contrast in figure (a) and out of contrast in figures (b), (c) and (d).

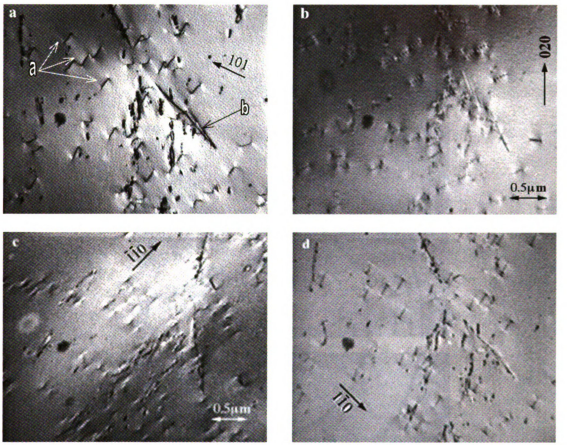


Figure 26. High purity 1600 FC specimen shows [001] mobile dislocations (marked as **a**) in different reflections. Type **b** dislocations, which are not moving due to the effect of beam heating, also seem to have similar Burgers vectors.

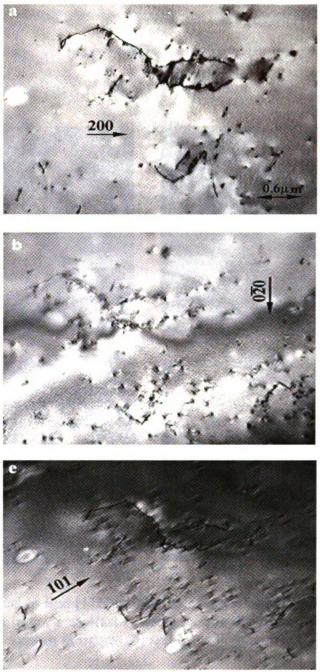


Figure 27. Dislocation characterization in high purity 673 AC specimens shows [1 0 1] dislocations in different reflections. Dislocations, which are almost parallel to the beam direction in figure (a), are characterized with reference to several immobile dislocations present in the microstructure. Such mobile dislocations are out of contrast in figures (b) and (c).

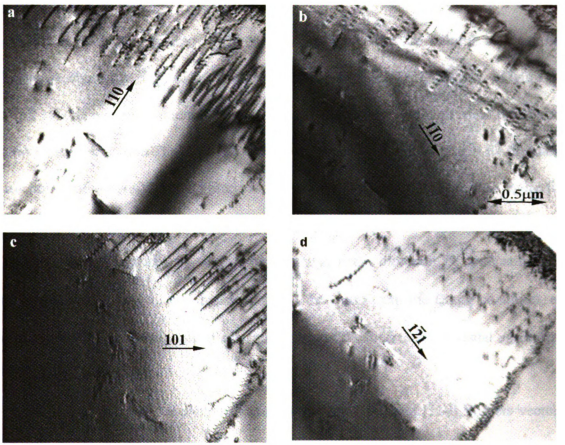


Figure 28. It is not usual to find [111] mobile dislocations in NiAl. Figures (a) and (c) show such dislocations in good contrast whereas mobile dislocations are observed with very weak and residual contrast in figures (b) and (d) in high purity 673 FC specimens.

An image of dislocations in the 673 AC undeformed commercially pure specimen is shown as figure 29. The dislocation marked 'A' is representative of most of the dislocations present in the micrograph. For better comparison with the computed image, several experimental images of the same dislocation were captured using three non-coplanar diffracting vectors.

Dislocation images from different diffracting vectors are helpful in obtaining information about all components of the displacement field of the defect. Figure 30 shows a set of seven experimental images of the dislocation 'A' with different diffraction vectors (**a-g**) tabulated in Table VI. Four sets of computer generated images for the same diffraction conditions and known Burgers vectors are also shown in the same figure for comparison. Important parameters to obtain those simulated images are also listed in Table IV; these parameters are diffracting vector **g**, beam direction **B**, dislocation line direction **u**, foil normal **F**, foil thickness **t**, and deviation from the Bragg condition, $\omega$. The object was to generate a set of computed images and find the best visual agreement with the experimental set.

It is evident from the computed images that the [100] and [110] Burgers vectors are not in agreement with the experimental image, especially when the dislocation in (c) goes close to invisibility or at its weakest contrast. The Burgers vector of [001] might be a possibility, but the computed image fails to match with the experimental image (d) for contrast. Based on the fact, these three Burgers vectors for dislocation 'A' may be ruled out. Further comparison of the remaining computed and experimental images confirms this conclusion. Moreover, visual agreement between experimental and simulated images suggests that the most likely Burgers vector for dislocation 'A' is [101].

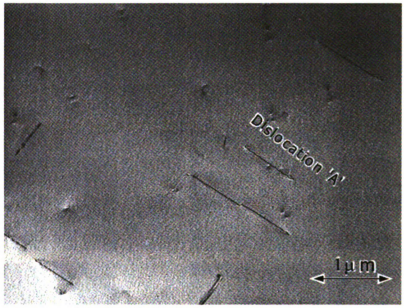


Figure 29. Dislocation 'A' in an undeformed commercially pure 673 AC specimen used for image simulation and generation of computed image.

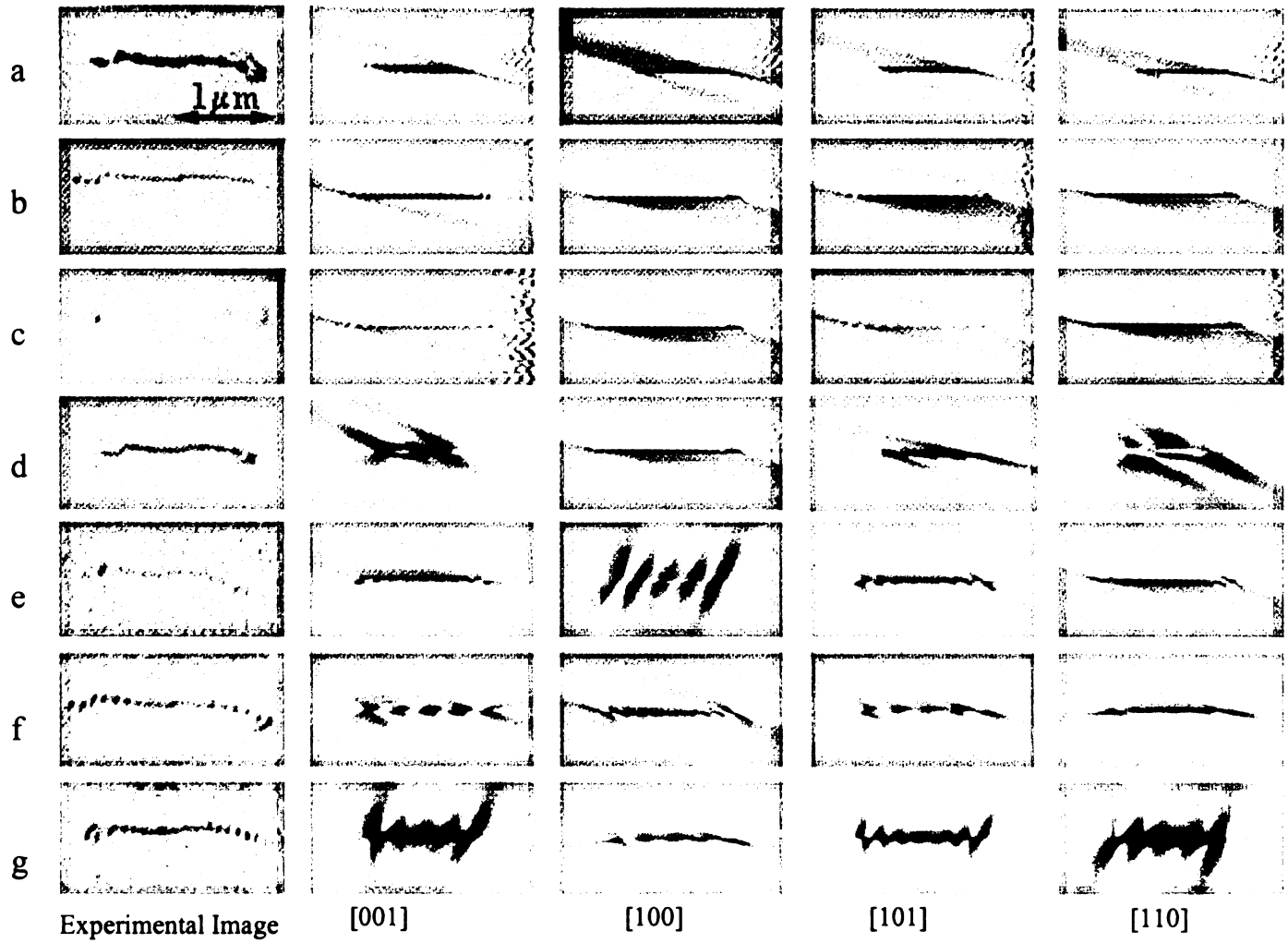


Figure 30. A set of experiment images (a) - (g) of dislocation 'A' taken with the diffraction conditions given in Table VI and four sets of computed images for the same diffraction conditions corresponding to the Burgers vectors shown.

Table VI. Parameters used to simulate dislocation 'A'

| g | a | b | c | d | e | f | g |
|---|---|---|---|---|---|---|---|
| | $\bar{2}\,0\,0$ | $1\,1\,0$ | $0\,2\,0$ | $\bar{2}\,0\,0$ | $0\,1\,\bar{1}$ | $\bar{1}\,1\,0$ | $0\,\bar{1}\,1$ |
| **u** | $\bar{5}\,23\,6$ | $\bar{5}\,23\,6$ | $\bar{5}\,23\,6$ | $\bar{5}\,23\,6$ | $\bar{5}\,23\,6$ | $\bar{5}\,23\,6$ | $\bar{5}\,23\,6$ |
| **B** | $0\,1\,6$ | $\bar{2}\,2\,15$ | $\bar{4}\,0\,19$ | $0\,9\,11$ | $\bar{1}\,3\,3$ | $\bar{1}5\,1\,5$ | $\bar{4}\,9\,9$ |
| **F** | $\bar{1}\,1\,2$ | $\bar{1}\,1\,2$ | $\bar{1}\,1\,2$ | $\bar{1}\,1\,2$ | $\bar{1}\,1\,2$ | $\bar{1}\,1\,2$ | $\bar{1}\,1\,2$ |
| ω | 0.8 | 0.85 | 0.6 | 0.4 | 0.7 | 0.6 | 0.26 |
| **t** | 1.3 | 3.5 | 4 | 1.3 | 3 | 3 | 2.16 |

where,

**g** = diffracting vector

**u** = dislocation line direction

**B** = direction of electron beam

**F**= foil normal

ω = deviation from Bragg condition and this is the dimensionless deviation parameter

**t** = foil thickness in extinction distances

Other parameters used for the simulation include the following:

Elastic constants: **C 11** = 2.03 **C 12** = 1.34 **C 44** = 1.16

and

Anomalous absorption coefficient: **ANO** = 0.07

## 4.5 *In-situ* Transmission Electron Microscopy

To study the dislocation motion in both high and commercially pure NiAl single crystals, 15 mm long micro-tensile specimens were deformed in the tensile stage of the TEM. In all of the samples using *in-situ* straining, dislocation motion was readily observed, regardless of the impurity concentration, orientation, and thermal history. Figure 31 presents a series of photographs depicting a sequence of dislocation motion resulting from *in-situ* straining. Prior to the *in-situ* straining, the morphology of the pre-existing dislocations was examined in each case and the samples were mapped for possible reference points to check any movement of the dislocations. Figure 31 (a) represents an area with pre-existing dislocations (PED).

Motion of dislocations was typically characterized by clearly evident slip traces left in the wake of dislocations. In most cases, dislocations were generated at the foil edge and slipped into the material. Dislocations were also generated from sources deep within the foil (it was not possible to observe these sources, as the foil was too thick to observe) and moved in the tensile direction (figure 31 b). These dislocations, lying perpendicular to the foil, moved in slip bands and slipped through the pre-existing dislocations lying in the plane of the foil. With straining, dislocations were seen to move by rapid jumps towards the edge of the foil (figure 31 c). While the dislocations tend to move in relatively well-defined slip planes, some limited cross-slip was observed as evidenced by waviness in the slip traces. Because the slip traces are presumably surface steps, the end-on dislocations must have a screw component. Motion of dislocations lying nearly perpendicular to a foil will only leave surface steps if the dislocations have a screw component.

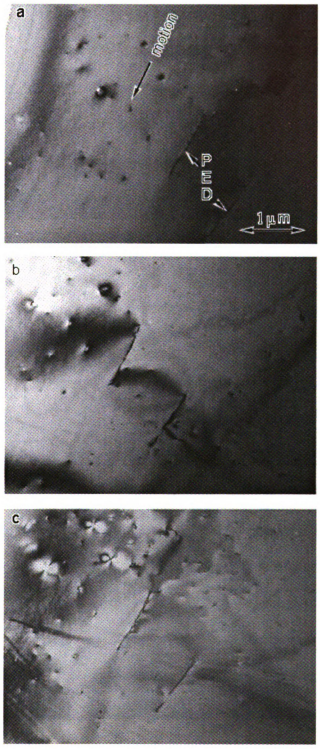


Figure 31. Dislocation motion in high purity slow-cooled [110] oriented NiAl. Sequence of events captured as (a), (b) and (c) revealed progressive movement of dislocations in the direction of the arrow. As a result of straining dislocations generated within the foil and starts moving towards the edge.

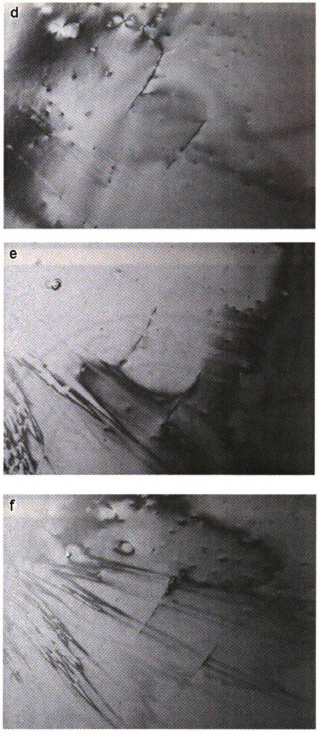


Figure 31 (contd.). Dislocations, almost perpendicular to the foil moved in the slip bands and cross-past pre-existing dislocations in the plane of the foil. Sequence of events (d), (e) and (f) revealed slight waviness in the slip bands that indicates cross-slip of such end-on dislocations. Figures (e) and (f) show development of dense slip bands.

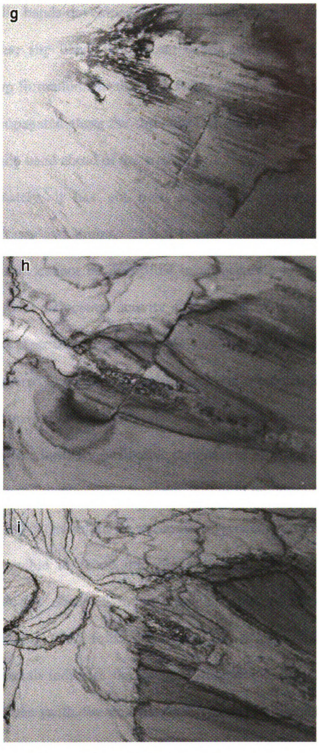


Figure 31 (contd.). Eventual crack initiation from the edge of the foil along the slip bands that produces avalanche of dislocations at its tip but the pre-existing dislocations stays sessile throughout the process.

Dense slip bands developed from the foil edges with further straining (figure 31 d). Within these slip bands, significant debris accumulated, resulting in dislocation pinning and loop formation. In the later stages of deformation, cracks developed at the foil edge and propagated along the slip bands, (figure 31 e through i), while dislocations piled up in the slip band ahead of the crack-tip.

Unfortunately, it has not been possible to relate the observed motion to macroscopic stresses and strains. This is because foil-to-foil variation in thickness and stress-concentration cannot be quantified in an accurate manner. The mobility of the dislocations and the dislocation activity at the onset of tensile straining were recorded dynamically and presented in the annexure as a digital video disc (DVD). Some static images were captured in between straining steps and presented here.

Dislocation velocities were also calculated. The values of the dislocation velocities provided a basis for qualitative comparison of dislocation mobility between the high and commercial purity single crystals. It should be noted that the absolute values of the dislocation velocities might be severely influenced by thin foil effects. Also, it is essentially impossible to relate the imposed strain rate of the tensile stage to the dislocation velocities observed in the complex state of stress generated around the thinning hole in the TEM foils. However, the relative difference in the velocities between the materials indicates significant differences in dislocation mobility. Thus, the measured velocities (with the constraints of the experimental conditions) reported in Table VII are used solely for the sake of comparison of dislocation behavior as a function of impurity concentration and cooling rates.

Table VII. Dislocation velocities measured at the onset of straining using CCTV camera

| Specimen | Thermal History | Tensile axis/ Orientation | Dislocation Velocity (μm/s) |
|---|---|---|---|
| Commercial Purity | 1600 K homogenization anneal and fast-cooled | <100> | 0.1 - 1.4 |
| Commercial Purity | 1600 K homogenization anneal and slow -cooled | <100> | 0.5 - 2 |
| Commercial Purity | 1600 K homogenization anneal and fast-cooled | <110> | 1.5 - 3 |
| Commercial Purity | 1600 K homogenization anneal and slow-cooled | <110> | 1 - 3 |
| High Purity | 1600 K homogenization anneal and fast-cooled | <100> | 5 - 25 |
| High Purity | 1600K homogenization anneal and slow-cooled | <100> | 4 - 20 |
| High Purity | 1600 K homogenization anneal and fast-cooled | <110> | 10 - 25 |
| High Purity | 1600 K homogenization anneal and slow-cooled | <110> | 13 - 17 |

Despite the significant differences in the dislocation velocities, it should be noted that as the deformation substructures developed, multiplication of the new dislocations within the slip bands was observed in all of the materials. Results from both commercial purity and high purity single crystals will be presented in the following sections. Some observations from the 3 mm disc straining of high purity specimens will be included in the last part of the results.

4.5.1 Commercial purity specimens

Dislocation motion studied in commercial purity specimens will be presented first. Tensile specimens were oriented such that the tensile axes of the specimens are near the 'hard' <001> or 'soft' <110> orientations of the single crystals. Studies were also conducted with specimens oriented to some arbitrary tensile axis such as [238]. Prior to *in-situ* straining, the morphology of the pre-existing dislocations was examined. Figure 32 shows a typical commercially pure sample with tangles of dislocations in slow-cooled condition. Many of the dislocations are extensively jogged and a few dipoles are also observed. Planar arrays of dislocations, which were observed in many parts of the foil prior to straining, remained immobile during the deformation.

Commercially Pure Air-Cooled [238]

Figure 33 shows dislocation activity in course of *in-situ* straining of commercially pure specimens. No movement of dislocations was noticed at the very start of the straining process. There may be some slop in the loading hole, which delayed the actual load on the specimen. The dislocations originated primarily from the edge of the foil with straining, and slipped in the tensile direction as well as at an angle to it. Distinct slip bands are observed in figure 33 (a). Figures 33 (b) and (c) show progressive movement

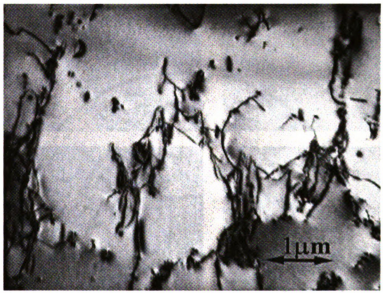


Figure 32. A representative microstructure of commercially pure NiAl single crystal exhibit tangles of dislocations. Many of the dislocations are extensively jogged and a few dipoles are also observed.

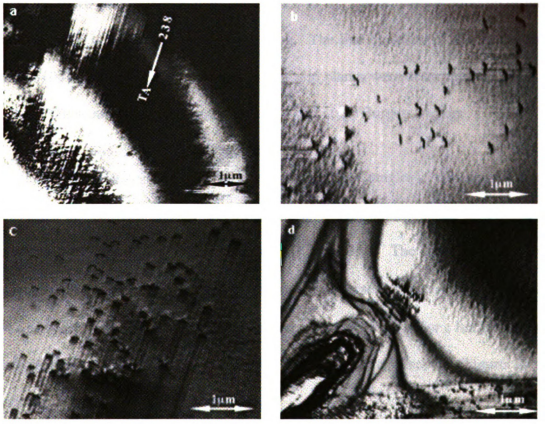


Figure 33. (a) Bright field image illustrating the nucleation of mobile dislocations at the edge (bottom left hand corner in the micrograph) of the foil in commercially pure air-cooled NiAl oriented to [238]. (b) and (c) Images showing the dislocation motion in two sl p bands displaying straight dislocation trails indicating no cross-slip. (d) Eventual cracking from the foil edge, propagating between slip bands.

of mobile dislocations slipping in two bands that developed from the same part on the foil edge. In the commercially pure samples, slip was very planar and the dislocations moved at a fairly constant, slow rate, rather than through quick jumps observed in high purity materials. Once significant slip occurred, cracks developed between the slip bands and punched out more dislocations at their tips (figure 33 d). There is some build up of loop debris in the slip bands after extensive straining. The line direction of the dislocations was near [100] in both of the slip planes, and the slip planes were determined to be (010) and (001). Consequently, the dislocations have <xy0> type Burgers vectors.

4.5.1.1 Commercially Pure Fast-Cooled [001]

This commercially pure material contained scattered tangles of dislocations along with straight dislocations prior to *in-situ* straining. With straining, the movement of dislocations was again slow and progressive (Figure 34). The average dislocation velocity was measured to be ~ 0.1 μm/s. However, in some cases, waviness in the slip traces was observed in addition to the straight trails (Figure 35 a). After a limited amount of deformation, extensive loops and debris formation were observed (Figure 35 b) particularly within the slip bands (Figure 35 a).

Figure 36 shows two images of the loop debris that formed over time within the slip bands in a different sample with similar thermo-mechanical history. As further dislocations pass through the area shown in figure 36, there was also evidence of some limited cross-slip away from the {110} planes as indicated by the wavy slip trails. This is the only condition under which any noticeable degree of cross-slip was observed in the commercially pure material. Dislocation motion was noticed in the bulk tensile direction (caused by rotation of the tensile axis) and in other directions as well. Dislocation motion occurred on both {010} and {110} planes and the line direction was <100>.

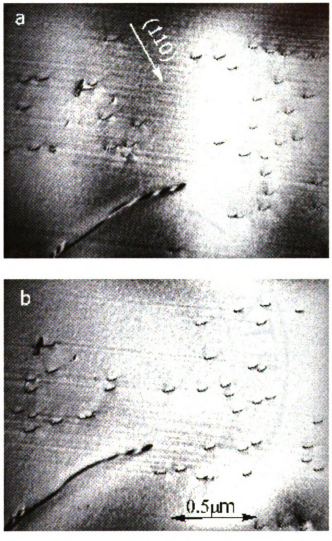


Figure 34. Dislocation motion in commercially pure fast-cooled [001] oriented NiAl. The mobile dislocations are referenced with the pre-existing dislocation lying in the plane of the foil and seen at the left side of the micrographs. Planar slip is evidenced with the slip-traces left in the wake of dislocations.

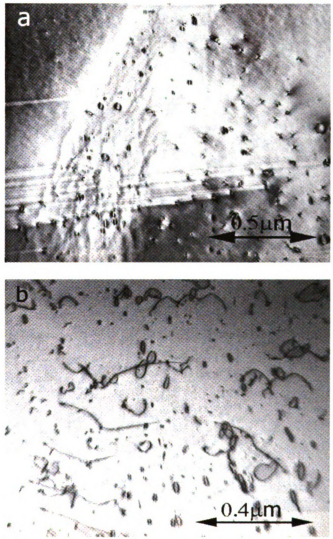


Figure 35. Images of dislocations generated via *in-situ* straining of air-cooled commercially pure single crystal oriented to [001] illustrating (a) both wavy and straight dislocation trails and (b) extensive accumulation of dislocation debris following straining.

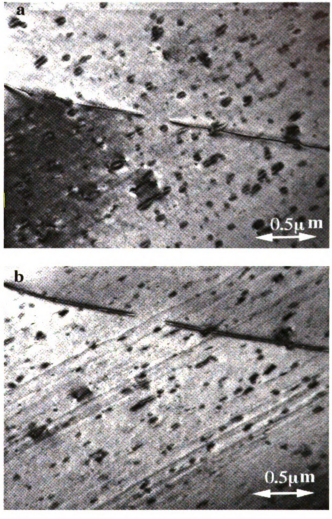


Figure 36. Limited cross-slip was observed in commercially pure fast cooled [001] oriented NiAl; loops and debris formed over time with straining.

4.5.1.2 Commercially Pure Slow-Cooled [001]

Commercially pure specimens cooled slowly within the furnace through the critical temperature region of embrittlement (673 K to 473 K) exhibited somewhat mixed dislocation structures prior to deformation. Heavily tangled pre-existing dislocations were observed in some areas, whereas straight isolated dislocations were pre-dominant in others. Again, none of these pre-existing dislocations were seen to move. In most cases the stress induced mobility of the dislocations ceases when they interact with the tangles.

In some instances the mobile dislocations moved within narrow channels of slip bands and through the pre-existing tangles with relative ease. Figure 37 (a) shows an example of dislocations being able to channel through such tangles during straining. Once the mobile dislocations overcome the interaction with the pre-existing tangles, newly generated dislocations migrate relatively easily through the pre-existing dislocations (figure 37 b and c). Dislocation motion with planar slip was noticed in a different commercially pure slow-cooled material as shown in figure 38, where mobile dislocations are referenced with a pre-existing dislocation lying in the plane of the foil.

Figure 39 shows two sequential images of the same area of a different slow-cooled [001] oriented commercially pure specimen. In this case, dislocations lying in the plane of the foil have moved as noted by the numbers. Like the other commercially pure materials, extensive loop debris have developed in the slip bands with strain and the dislocations were bowed out, generating additional dislocations through the operation of single-ended Frank-Reed sources (figure 40). While the dislocation motion was again slow and deliberate in this material, the measured average velocity was slightly higher than 0.1 μm/s.

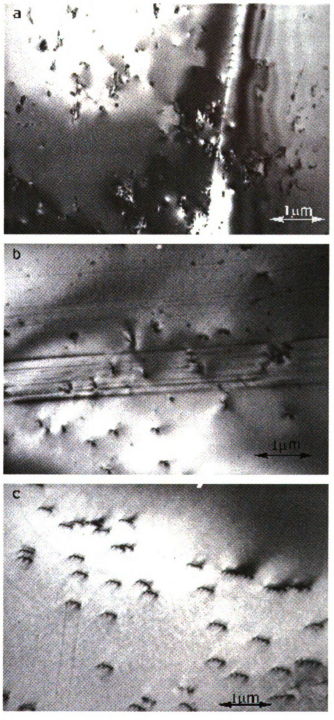


Figure 37. Prior to deformation, heavily tangled dislocations were observed in many areas of the commercially pure [001] orientated furnace-cooled material. At the onset of straining, dislocations channeled through the tangles (a). With continued deformation, newly generated dislocations slipped through the pre-existing dislocations with relative ease (b) and (c).

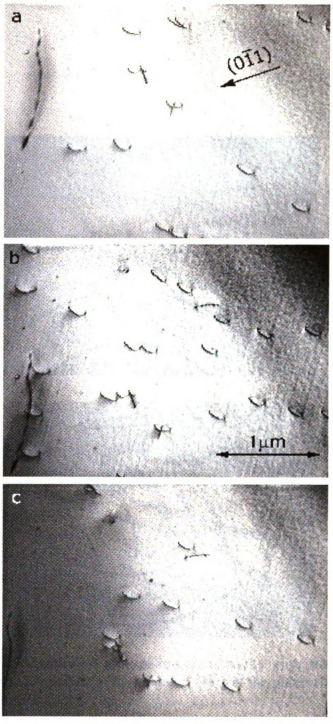


Figure 38. Dislocation motion in commercially pure [001] oriented NiAl. The mobile dislocations are referenced with the pre-existing dislocation lying in the plane of the foil and seen at the left side of all the micrographs. Planar slip is evidenced with the slip-traces left in the wake of dislocations. Most of the mobile dislocations seen in (b) were not present in (a) and left the field of view in (c).

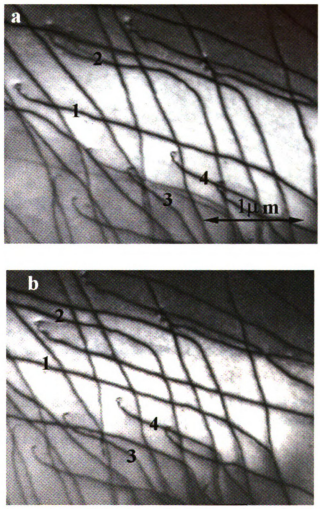


Figure 39. Sequence of dislocation motion in commercially pure slow cooled [001] oriented NiAl. Dislocations (marked with numbers) lying in the plane of the foil move in a slow and uniform manner.

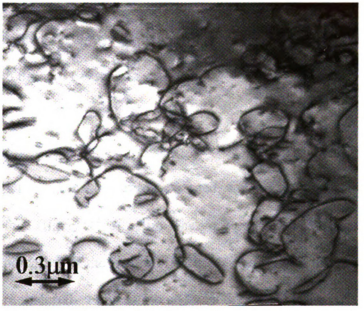


Figure 40. Loops and debris formation is evident in slow-cooled commercially pure [001] oriented NiAl. Dislocation multiplication by operation of single-ended Frank-Read sources takes place in the substructure.

Although a few wavy slip traces were noticed, straight slip traces were predominant in all commercially pure materials. Loops and debris were also observed early in the deformation process. In this case, similar to the previously discussed air-cooled sample, the slip planes of the mobile dislocations appeared to be {100} and {110}. The line directions of the glissile dislocations were near [100]. No significant difference in the dislocation behavior of micro-tensile specimens was observed between the slow and fast cooled specimens, although the bulk mechanical properties differed significantly for such thermal treatments.

4.5.1.3 Commercially Pure Fast-Cooled [110]

Dislocation movement in this material was very slow with an average velocity less than 0.1 μm/s. Dislocations appear to be pinned, and slipped by bowing out from the ends at the foil surface (figure 41 a). Slip was very planar and cross-slip was seldom observed. This is indicative of the nature of difficulty lying with dislocation movement in commercially pure material. Figure 41 b shows a dark-field image of the pre-existing dislocations lying in the plane of the foil. These dislocations again only impeded further dislocation movement to a limited degree. With continued straining loops and debris developed in the microstructure as well as dislocation multiplication took place (figures 41 c and d).

Figure 42 shows a series of images characterizing the initial stages of dislocation motion. This is clearly evident that the movement rate was sluggish at the onset of straining and it required an increased deformation for continuous generation and motion of dislocations. Again, pre-existing dislocations did not significantly inhibit the mobile dislocations that glided on well-defined {110} planes. A similar situation was observed

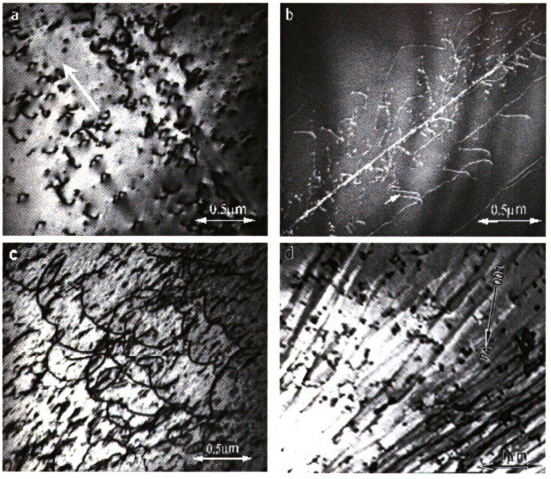


Figure 41. Commercially pure fast-cooled [110] oriented NiAl. (a) Dislocations slip in the marked direction in slip bands by bowing out from the dislocation ends at the foil surface. (b) A dark-field image showing a few mobile dislocations (arrowed) and planar arrays of pre-existing dislocations. (c) Dislocation multiplication is taking place. (d) Loops and debris are also evident.

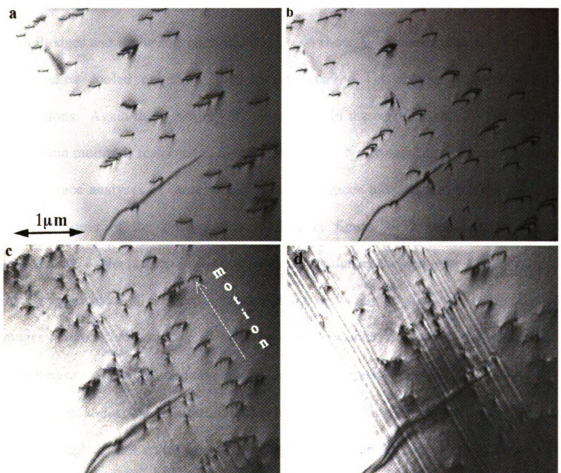


Figure 42. Series of images in commercially pure fast-cooled [110] oriented NiAl characterizing the initial stages of dislocation motion. Figures (c) and (d) show subsequent slip in well-defined narrow slip bands.

in another sample (figure 43) where dislocation movement rate was not identical in all areas of observation. The slip plane was identified as {110} and the line directions of the mobile dislocations were close to <001>.

4.5.1.4 Commercially Pure Slow-Cooled [110]

As with other samples, application of strain led to dislocations being generated at the foil edges and in the foil interiors. Figure 44 shows a sequence of dislocation motion in the slow cooled material. Dislocations marked 1-4 display the motion of the dislocations. Again the slip was very planar, and in the early stages of deformation the dislocation motion is restricted to narrow slip bands. No cross-slip has been observed.

Trace analyses of these well-defined slip traces indicate that the slip planes are {110}. Some of the dislocations, marked in figure 44 b, appear doubled as a consequence of the portion of dislocations moving during the exposure of the plate. The small increment of slip, over the length of the dislocations, displayed by these double images is consistent with overall mobility of dislocations in this material. The average measured rate of dislocation movement was approximately 1.3 μm/s.

With strain, the dislocation interactions within the slip bands increased and they became tangled; as a result of which extensive loop debris accumulated. These debris inhibited further dislocation motion as new dislocations gliding in the bands had to bow out from local pinning points caused by debris (figure 45). While these debris did impede further dislocation motion, it could not eliminate it. The bowed out dislocations were able to break free from the obstruction in many cases. Additionally, many new dislocations were produced in slip bands through the bowing-out or pinching-off of the dislocations.

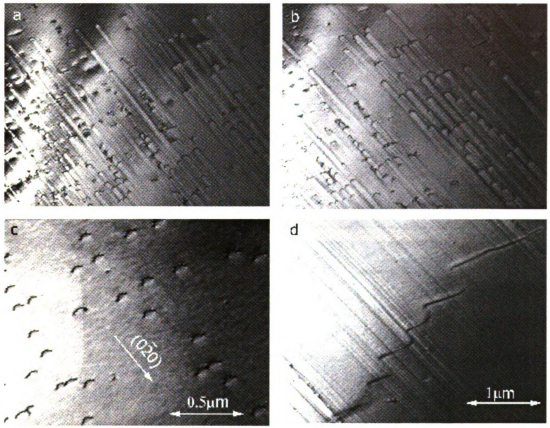


Figure 43. Dislocation motion in commercially pure fast-cooled [110] oriented NiAl. Series of images (a) through (d) reveal dislocation mobility with planar slip and relative difference in the velocity of the dislocations.

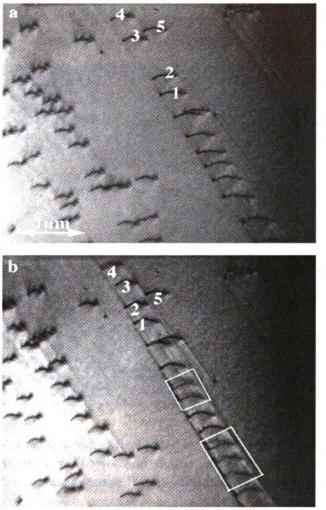


Figure 44. Sequence of dislocation motion in commercially pure slow-cooled [110] oriented NiAl. Dislocations marked 1-5 display the relative motion of the mobile dislocations. Note the very planar slip confined in narrow slip bands. Dislocations marked in figure (b) appear doubled as a consequence of portions of dislocations moving during exposure of film.

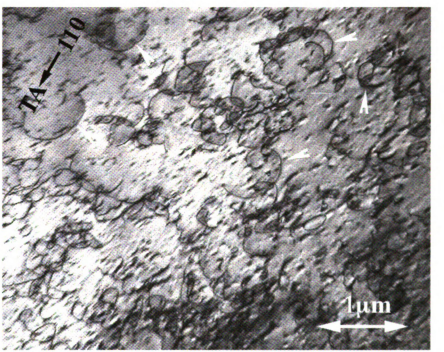


Figure 45. Commercially pure slow-cooled [110] oriented NiAl. With increasing strain dislocations became tangled and loops and debris accumulated. Bowing out of the dislocations show that the motion was not totally inhibited by the debris.

Figure 46 shows an example of this phenomenon in a sequence of images captured using the video system. Figure 46 a-c show a dislocation loop (arrowed) expanding under the applied stress. (The contrast of the dynamic image was enhanced using Adobe PhotoShop.) In figure 46 d, the loop has pinched-off and was set to expand again, while a neighboring loop has expanded under the applied stress. It is interesting to note that despite being heat treated in an embrittling fashion, dislocation generation, motion and multiplication were possible in all of the slow cooled commercially pure material. The difference in bulk mechanical behavior of the commercial purity material is not well correlated with the dislocation behaviors in the micro-tensile specimens.

4.5.2 High purity specimens

In general the pre-existing dislocation density was much lower for the high purity specimens than for the commercially pure specimens as shown in figure 47 a. Prior to *in-situ* straining, planar isolated dislocations were observed in different regions of the foil (figure 47 a and b). In general figure 47 shows presence of a few loops with some pinched-off dipoles in slow cooled high purity material. With straining, dislocations began to nucleate from the foil edge and slip into the material; dislocations were also generated from deep within the foil but the sources could not be observed due to foil thickness. Both planar slip and cross-slip was observed in high purity materials; cross-slip is evidenced by waviness of slip-traces left by the mobile dislocations as they change slip planes [100, 101].

The most significant difference between the observed behavior of the high and commercial purity materials was the observed dislocation velocities. The observed velocities (as reported in Table V) in the high purity materials were at least an order of

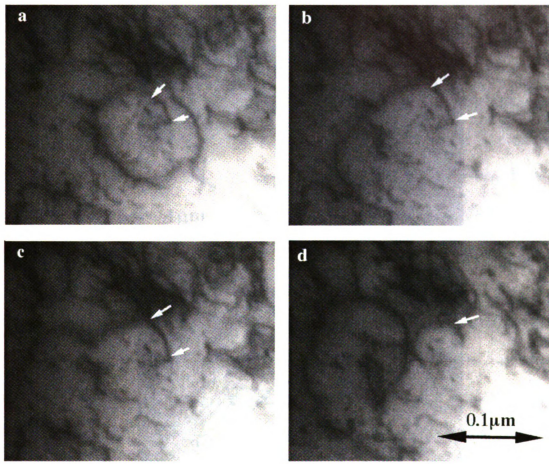


Figure 46. Multiplication of dislocations through operation of single-ended Frank-Read sources in commercially pure slow-cooled [110] oriented NiAl. Images captured dynamically with a video system showed the arrowed dislocation loop expanding under the applied stress (a-c). The next image (d) shows that the loop has pinched-off and is set to expand again while a neighboring loop has also expanded. (Quality of the picture is regretted and Adobe PhotoShop was used to enhance the contrast of a dynamic image)

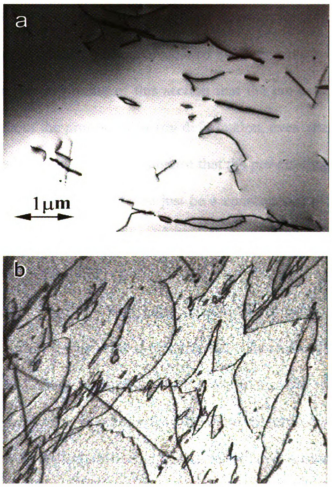


Figure 47. Pre-existing dislocation morphology in high purity slow-cooled NiAl showed mostly isolated dislocations; a few loops were also seen along with some pinched-off dipoles. (a) A typical area of [110] oriented single crystal with much lower dislocation density compared to commercial purity specimens. (b) An area with unusually higher concentration of dislocations in a slow-cooled [001] oriented specimen before straining.

magnitude greater than in the commercial purity materials and indicate significant differences in dislocation mobility. Sometimes dislocations were seen to move at a speed where the critical flicker frequency of human eye was not adequate to capture the progressive movement of the dislocations. In comparison, for commercially pure materials, it was possible to track movement of isolated line segments.

As mentioned at the beginning of this section that the pre-existing dislocations remained sessile throughout the process of *in-situ* deformation, even after the passage of cracks physically divided the foil. This may suggest that the pre-existing dislocations are immobile or pinned. However, this may also just be a consequence of the pre-existing dislocations being in orientations disadvantageous for slip in the *in-situ* studies.

4.5.2.1 High Purity Fast-cooled [001]

Motion of dislocations in the high purity NiAl was typically characterized by clearly evident slip traces left in the wake of dislocations. The dislocations were seen to move at a variety of rates. Many dislocations were found to move at much higher rates relative to other observations for commercially pure materials in this study. The very high velocity of the mobile dislocations could not be determined accurately because the mobile dislocations could not be captured in two successive frames, but is estimated in the range of 5 – 25 μm/s.

It may be mentioned that the dislocation velocity was calculated from the TV screen where images are seen at the rate of thirty-two (32) frames per second. Critical Flicker/fusion frequency (CFF) for normal human vision is determined to be in the range of 40 – 90 Hz depending on the intensity of the light [106]. This implies that if any dislocation moves between two successive frames, human eye may or may not capture it

depending on the speed at which the object moves and also the intensity of light at the screen. Therefore, dislocation velocity was estimated to the closest approximation for instances where dislocation velocity could not be calculated precisely.

Figure 48 shows both planar slip and development of loop debris at different part of the same foil. In some cases orthogonal slip was observed for dislocations with line direction perpendicular to the foil surface (figure 49). Dislocations lying in the plane of the foil (figure 50) were also seen to move quite rapidly. There must be high, local residual stress developed due to straining of the thin foil causing movement of such dislocations that have zero Schmid factor. The slip plane and the line directions of the mobile dislocations were identified as {112} and <110> respectively.

4.5.2.2 High Purity Slow-cooled [001]

Dislocations were seen to move with ease by rapid jumps. The velocity of the mobile dislocations was measured in the range 4 – 20 μm/s. Dislocations were generated in the thicker parts of the foil and the movement of the dislocations was assisted by cross-slip. The direction of motion (not to be confused with the slip direction) of the mobile dislocations had changed from [001] to [111]. The observed slip traces in figure 51 show a dislocation cross slipping past its neighboring dislocations on its way to exiting the foil at the edge. In some other cases dislocations were also seen to generate at the foil edge and move towards the thicker part of the foil; it was very difficult to follow the dislocation activity in those thicker areas.

Some of the samples exhibited a very different response with the applied load and very slow and deliberate movement of dislocation was observed (figure 52). Increased deformation resulted in the development of loops and debris in slip bands, along with

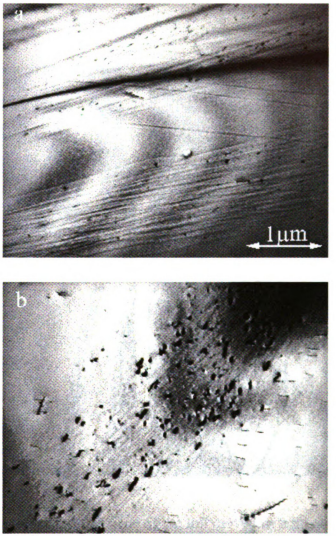


Figure 48. Dislocation motion at the onset of straining in high purity [001] oriented fast-cooled material. Micrographs were captured at two different parts of the foil when dislocation generation and movement were noticed from the edge of the foil. While slip was mostly planar and debris were not readily formed in one part of the foil (a), the other part shows a significant amount of dipole debris in well-defined slip bands (b).

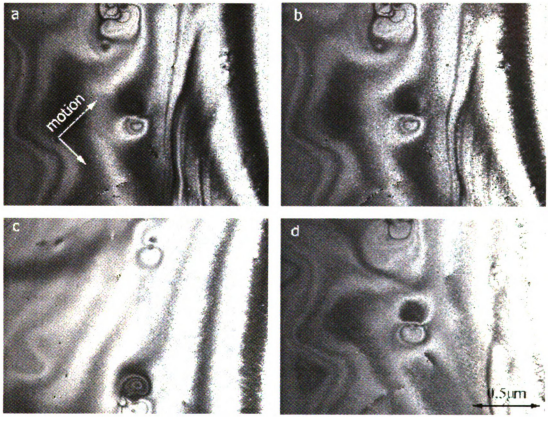


Figure 49. Dislocations normal to the plane of the foil moved in orthogonal directions in high purity [001] oriented fast-cooled material. The contrast from the slip traces of such end-on dislocations was not as sharp as observed for dislocations lying at some angle to the plane of the foil. The disturbance created on the oxide layer was less pronounced for being captured as well-defined slip traces during the exposure time of still photographs.

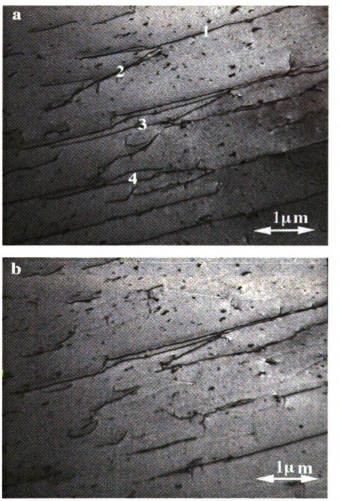


Figure 50. Dislocations that are lying near the plane of the foil (marked 1, 2, 3, and 4) in figure (a) were found to move quite rapidly in high purity [001] oriented fast-cooled material and not seen in figure (b).

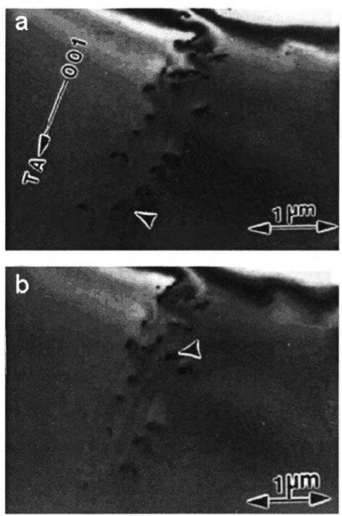


Figure 51. High purity slow-cooled [001] oriented NiAl. (a) Dislocations generated within the foil and moved towards the edge. (b) The arrowed-dislocation cross-slipped past its neighbors.

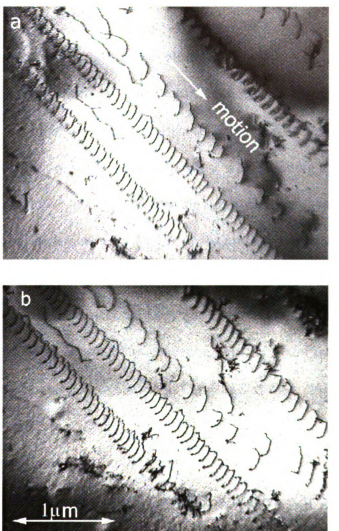


Figure 52. Slow movement rate noticed with dislocations generated in high purity slow-cooled [001] oriented NiAl. Dislocations moved at such a low rate that movement of individual segments of dislocations were apparent.

activation of single-ended Frank-Read sources. Figure 53 shows a sequence of such loop and debris formation. Orthogonal slip was also observed (figure 54). The slip planes were identified as {112} and {110} with [101] line directions of the mobile dislocations.

4.5.2.3 High Purity Fast-cooled [110]

Figure 55 (a) shows an area in the high purity fast cooled NiAl, which possessed uncharacteristically high numbers of pre-existing dislocations. Most of the pre-existing dislocations were nearly straight and isolated; a few loops were also seen. In high purity material dislocations began to move at a very rapid rate with straining and glide past all of the pre-existing dislocations. It appeared that the pre-existing dislocations could not inhibit the slip of the mobile dislocations. Mobile dislocations have escaped the field of view in figure 55 b leaving wavy slip traces.

Similar to [001] oriented fast cooled material, dislocations moved at a very high rate for [110] orientation also. The mobile dislocation velocity could not be determined with acceptable uncertainty and approximated in the range of 10 – 25 μm/s. The slip planes were identified as {001}.

4.5.2.4 High Purity Slow-cooled [110]

Dislocation motion was characterized by clearly evident slip traces left in the wake of dislocations (figure 56 a). With straining, dislocations moved by rapid jumps and dense slip bands developed from the foil edges. Dislocations, which are normal to the foil, moved in slip bands and slipped through the pre-existing dislocations lying in the plane of the foil (figure 56 b).

Pre-existing dislocations did not seem to inhibit the motion of such end-on mobile dislocations. The mobile dislocations were found to move on {112} planes and had

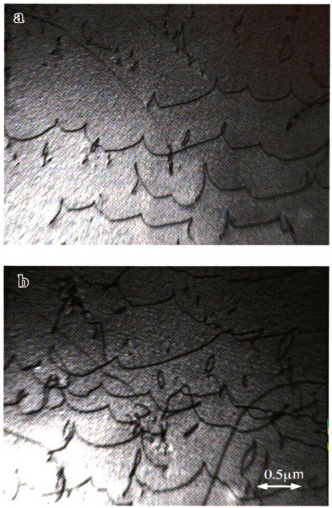


Figure 53. (a) Dislocations generated within the foil in high purity slow-cooled [001] oriented NiAl. (b) Mobile dislocations developed loops and debris as a result of dislocation motion and interactions.

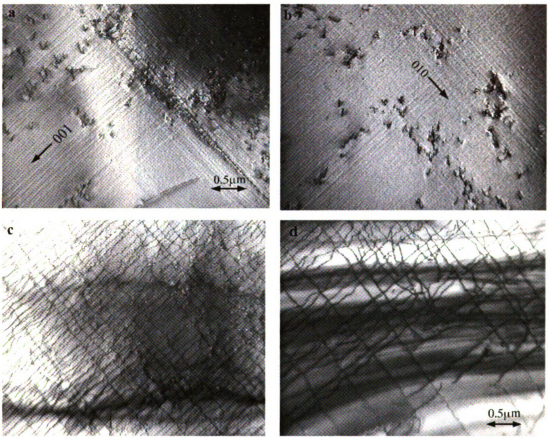


Figure 54. Dislocations moving in the foil leaving well-defined trails of planar slip in high purity slow-cooled [001] oriented NiAl (figures a and b). Line directions of the mobile dislocations were close to the foil normal. Debris were developed at a slower rate and orthogonal slip takes place. Figures (c) and (d) reveal orthogonal dislocations lying in the plane of the foil after *in-situ* straining. The dislocation density decreased as the foil edge was approached.

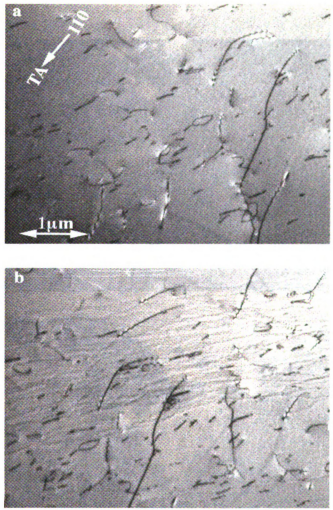


Figure 55. High purity fast-cooled [110] oriented NiAl. (a) The pre-existing dislocation morphology shows high number of nearly straight, isolated dislocations with a few loops. (b) Dislocations moved at a very rapid rate with straining and have slip past all pre-existing dislocations. Cross-slip of the dislocations is evident from the wavy slip trails.

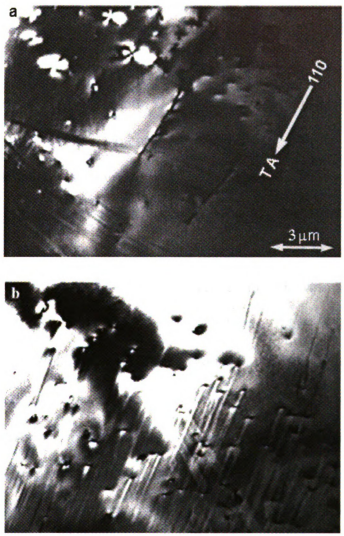


Figure 56. Evolution of dislocation slip in high purity [110] oriented slow-cooled NiAl. (a) Pre-existing dislocations lying in the plane of the foil did not move while newly generated dislocations (lying normal to the plane of the foil) glided leaving visible slip trails. (b) Slip bands were more evident after further deformation.

<111> line directions. In a different sample dislocation motion was observed (figure 57) in different parts of the foil at the onset of straining. Dislocations that were generated from the foil-edges moved readily into the foils, often moving through or past the pre-existing dislocations. Figure 57 a shows the dislocations, which were generated at the nearby foil edge migrating into thicker areas of the foil. Note that the dislocations were bowed out to a degree in the direction of motion with the ends (at the top and bottom of the foil) lagging somewhat behind. Figure 57 b shows not only dislocations that had slipped, but also slip trail, left in the wake of dislocations. These trails are the consequence of the dislocations disturbing the top and bottom of the foils as they pass.

The slip trails in the present case are wavy, indicating that cross-slip is taking place, and the dislocations must be screw in nature. Trace analysis of the dislocations shows the line directions were near <111> and the average slip plane was near {112}.

The dislocations were seen to move at a variety of rates. Many dislocations were found to move at high rates (relative to other observations in this study) with a measured velocity of approximately 13–17 μm/s. Other dislocations were found to move at slower rates, in particular in association with dislocation pile-ups. With continued straining, significant levels of tangles developed in the slip bands (figure 58). Unlike commercially pure material, dislocation tangles did not seem to inhibit further dislocation motion. As the dislocation tangles continued to develop, dislocation multiplication took place within the slip bands, by operation of single ended Frank-Read sources. With time, extensive loop debris formed in the bands (figure 59).

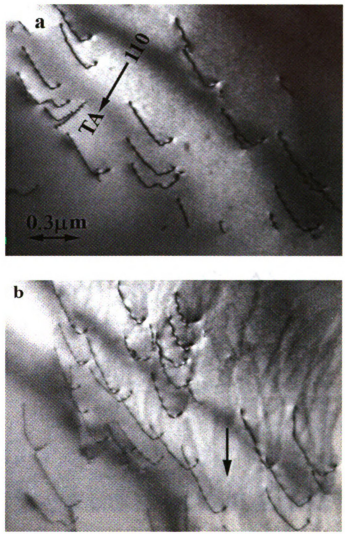


Figure 57. Images of dislocation motion in high purity slow-cooled [110] oriented NiAl. (a) Dislocations generated at nearby foil edge gliding into thicker areas of the foil. The direction of motion is marked on the figure (b) that was different than the tensile deformation axis (TA) marked on figure (a). (b) Wavy slip trails left in the wake of the dislocations indicate a variation in the slip planes of the slipping dislocations.

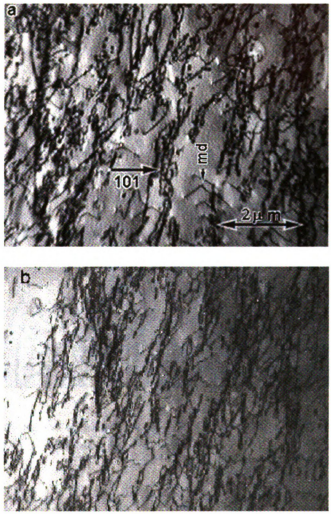


Figure 58. With increasing deformation, dislocation tangles developed in the high purity [110] oriented slow-cooled NiAl. Unlike commercial purity material dislocation tangles did not inhibit movement of the mobile dislocations (marked md in figure 58 a) in high purity specimens.

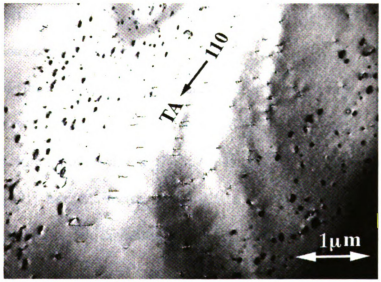


Figure 59. With increasing deformation, loops and dipole debris developed in the slip bands in the high purity [110] oriented slow-cooled NiAl.

4.5.3 Disc-Straining of High Purity Specimens

A few selected 3 mm disc samples from high purity single crystals were deformed in the tensile stage as described in the experimental section (3.7). The straining was never continued through the failure of the samples and always stopped after a noticeable extent of dislocation activity. Samples were transferred to a double-tilt holder following straining. Thus, all three primary zone axes could be utilized with increased flexibility of tilting to the desired angles; also difficulty of using invisibility criterion to characterize mobile dislocations could be minimized.

Mobile dislocations in figure 60 were observed in reference to the pre-existing dislocations shown at the bottom-left corner of the micrograph (figure a). The dislocations are close to invisibility in figure (b) and visible with weak-contrast in figure (c) suggesting [001] Burgers vector. Similarly, in a different fast-cooled high purity single crystals sample, mobile dislocations with [100] Burger's vector observed in narrow slip bands in figure 61. Several pre-existing dislocations were seen in the field of observation on both sides of the slip bands. As an example, dislocations marked '1' and '2' were identified to have [010] Burgers vector.

Figure 62 reveals a complex situation for mobile dislocation characterization in a different high purity slow-cooled NiAl sample where complete invisibility could not be achieved utilizing three different zone axes such as [001], [011] and $[\bar{1}\,\bar{1}1]$. There may be two different types of mobile dislocations. Dislocations somewhat confined in slip bands may have $[10\bar{1}]$ Burgers vectors for being in weak contrast in figure (b) and and complete invisibility in figure (c). Mobile dislocations, to the right of the slip bands, may have $[11\bar{1}]$ Burgers vectors for being out of contrast in (c) and weak contrast in (d).

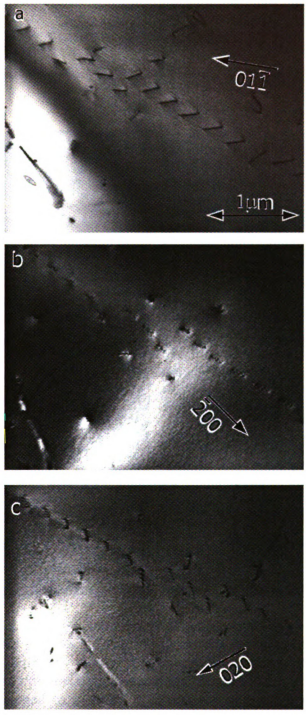


Figure 60. Mobile dislocation characterization in high purity slow-cooled NiAl. The mobile dislocations are referenced with the pre-existing dislocation lying in the plane of the foil. Dislocations with good contrast in (a) are observed with weak-contrast in (b) and become invisible in (c) suggesting [001] Burgers vector.

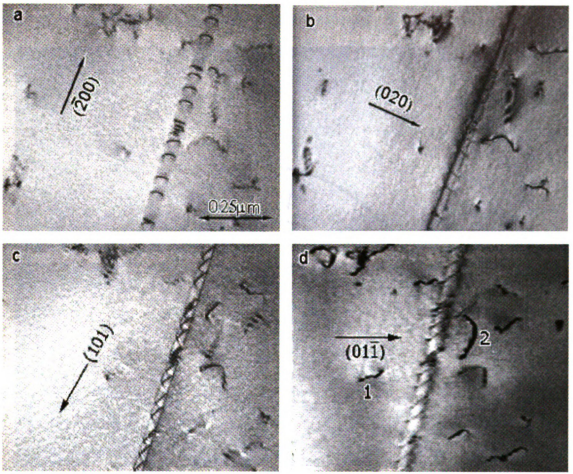


Figure 61. Dislocation mobility was observed within a narrow slip band. Mobile dislocations were visible in good contrast in figures a) and c) and appeared with weak contrast for figures (b) and (d). These dislocations were characterized to have [100] Burgers vector. Likewise pre-existing dislocations (marked 1 and 2 on both sides of the slip-bands in d) are seemed to have [010] Burgers vector for becoming invisible in figures (a) and (c).

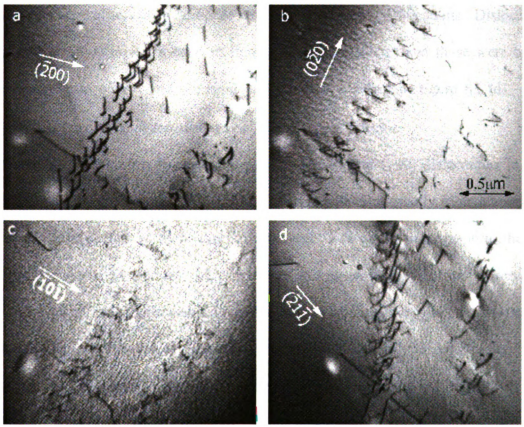


Figure 62. Mobile dislocations in high purity slow-cooled NiAl. In absence of complete invisibility, the Burgers vector could not be conclusively determined. Two types of mobile dislocations were present. The ones somewhat confined in the slip bands have $[10\bar{1}]$ Burgers vectors from figures (b) and (c) whereas dislocations to the right side of the slip band may be of $[11\bar{1}]$ type from figure (c) and (d). The line direction of the pre-existing dislocations lying in the plane of the foil was determined to be [010] from figures (a) and (c).

Unlike *in-situ* straining of tensile specimens, no cross-slip was observed during disc straining of high purity specimens.

Although observation of <111> dislocations is not very likely for <110> orientation, the same type of dislocations was found to be mobile in other samples too. Figure 63 reveals dislocation mobility in high purity fast-cooled specimens. Mobile dislocations were observed in reference with two pre-existing dislocations. Dislocations were seen to move in a slip band in figures 63 (a) and 63 (c) and those were out of contrast in figure 63 (b) and observed with residual contrast in figure 63 (d). This suggests that the mobile dislocations have $[1\,\bar{1}\,\bar{1}]$ Burger's vector.

Figure 64 shows a sequence of micrographs to find [100] dislocations in high purity fast-cooled specimens. The field of view contains unusually high numbers of mobile dislocations that were moving from the right side of the micrograph to the left. The slip was planar as seen from the slip traces and no cross-slip has been observed in this case. All of the mobile dislocations may not be of the same type or there may be localized stress, which reveal dislocations at different contrast level using the same diffracting vector. Mobile dislocations in high purity fast-cooled NiAl (figure 65), seen in contrast in figures 65 (a) and 65 (b), were found to have $[10\bar{1}]$ Burgers vectors for being in weak contrast in figures 65 (c) and 65 (d).

Figure 66 shows an area with unusually high dislocation density in fast cooled high purity single crystal. Dislocations were seen to be mobile in slip bands while some loops and deformation substructure were also evidenced. Mobile dislocations were identified as [111] type. In another slow-cooled high purity material [101] dislocations were found to be mobile as seen in figure 67. Dislocations were found to be mobile in

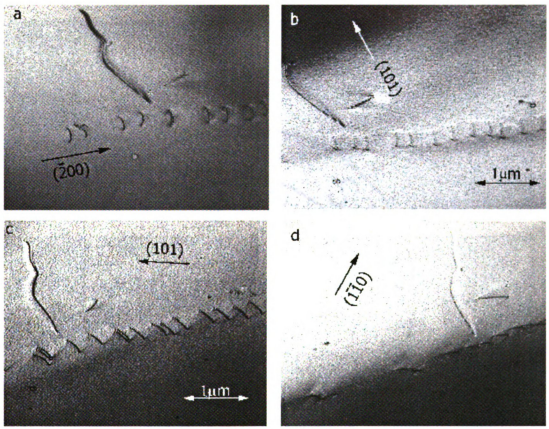


Figure 63. Pre-existing dislocations lying in the plane of the foil are used as reference in high purity fast-cooled single crystal. Dislocations seen in good contrast in (a) and (c) were observed with weak contrast in (b) and (d) and determined to have $[1\,\bar{1}\,1]$ Burgers vector.

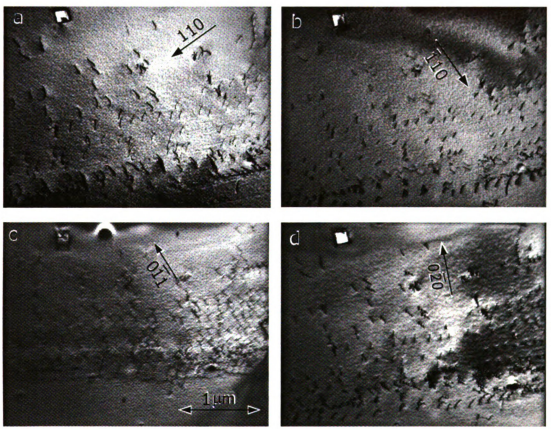


Figure 64. Mobile dislocation characterization in high purity fast-cooled single crystal. Dislocations, those were seen in good contrast in (a) and in (b) became invisible in (c) and were observed with weak-contrast in (d) suggesting [100] Burgers vector.

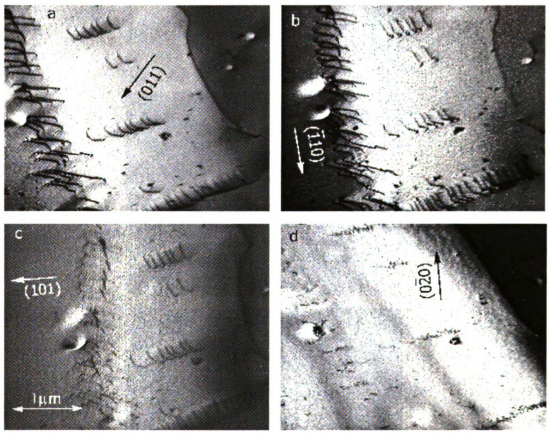


Figure 65. The mobile dislocations in high purity slow-cooled single crystals are referenced with the pre-existing dislocation seen in the right side of the micrographs. Dislocations seen in good contrast in (a) and in (b) were observed with weak contrast in (c) and became invisible in (d) implying $[10\bar{1}]$ Burgers vector.

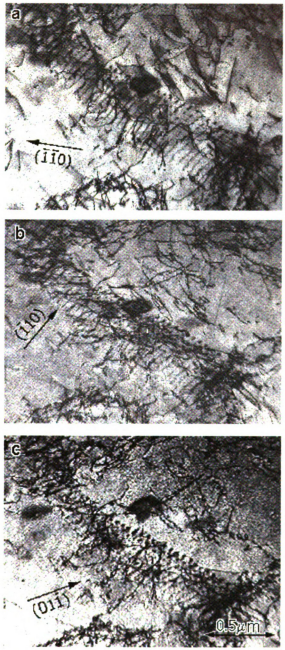


Figure 66. Images from slow-cooled high purity NiAl shows mobile dislocations in slip bands. A significant amount of deformation substructure has been formed and some dislocation loops are also observed in the substructure. The dislocations within the slip bands are in extinction in figure (c) and in very weak contrast in figure (b) indicating mobility of [111] dislocations.

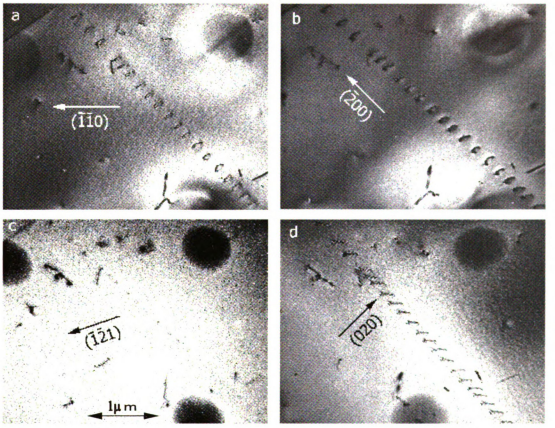


Figure 67. Dislocations moving in narrow slip bands in slow-cooled high purity NiAl. The dislocations are in extinction in figure (c) and in very weak contrast in figure (d) suggesting mobile dislocations [101] mobile dislocations.

narrow slip bands and contrast analyses was performed utilizing the pre-existing dislocations as well as some stains in the sample. Figure 68 shows an area very much similar in appearance like figure 66 except for slow-cooled specimens. Mobile dislocations were identified as [101] type whereas some of the deformation-induced dislocations and loops were [010] type.

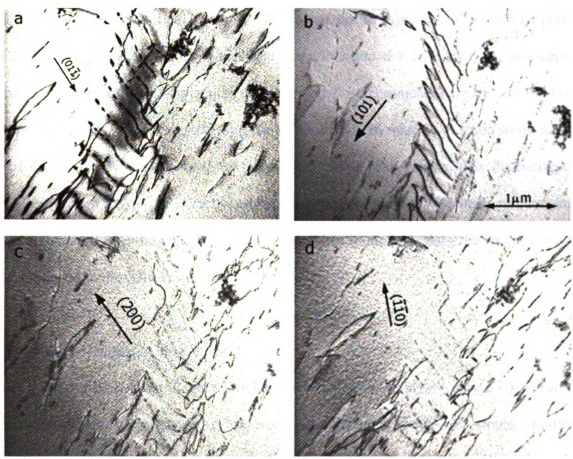


Figure 68. Images from slow-cooled high purity NiAl show mobile dislocations in slip bands. The mobile dislocations were in extinction in figure (c) and in very weak contrast in figure (d), suggesting [101] mobile dislocations. Similarly, some of the pre-existing dislocations or loops may be of [010] type for being in extinction and weak contrast in figures (b) and (c) respectively.

# 5.0 **DISCUSSION**

The behavior of the NiAl single crystals studied in the current investigation varied depending on the impurity concentrations and the imposed cooling rates. The final cooling rates from elevated temperatures influenced the yield stress significantly in the commercially pure material, but the influence was not so pronounced in the high purity material. The differences in mechanical behaviors and the differences in dislocation morphology following compression deformation of the commercially pure and the high purity single crystals are explained in the present study in relation to static strain aging. The dislocation behavior consequent to tensile straining also varied widely depending on the alloy chemistry, which can also be explained in light of dynamic strain aging. Important findings from these observations described in the preceding results section will be discussed in the following subsections.

## 5.1 Structure-Property Correlations

Dislocation substructures and the response to cooling rate varied significantly between the deformed and undeformed conditions of the NiAl single crystals. Undeformed specimens exhibited isolated and widely spaced dislocations throughout the structure; few loops and tangles were observed. The overall dislocation density was lower for high purity (HP) materials than for commercially pure (CP) materials and within the same purity single crystals the dislocation densities were similar for both the fast and the slow-cooled condition in the undeformed state. Reheating at intermediate temperatures had no apparent effect on this structure, as was shown in figure 16 for the

commercially pure material. This observation for undeformed NiAl single crystals provides evidence that the effect of cooling rate on existing dislocation morphology was not so pronounced when the dislocation density was low in the substructure. In absence of any barriers or dislocation tangles, isolated dislocations exhibited some mobility as a result of stresses generated from beam heating. The slip plane of these mobile dislocations was identified as {001}, and both <110> and <001> dislocations were present in the microstructure, with the majority being <001>. The presence of <001> dislocations has been reported in almost all such previous works except in <001> oriented single crystals [6 and 7].

High purity and commercially pure NiAl single crystals responded differently to the compression deformation tests as shown by their yield-stress values reported in Table III and IV. This difference is most likely due to the difference in the impurity concentrations of the commercial purity and the high purity materials, as detailed in Table II. As such, the solid solution hardening effect (a function of the solute concentration) of any commercial purity material will always be expected higher than for any high purity material. Impurity atoms such as carbon and oxygen occupy the interstitial sites and induce solid-solution hardening in NiAl that is reflected in the higher yield stress of the commercial purity NiAl than the high purity NiAl single crystals. Weaver et al. [87] concluded that carbon and oxygen are the key contributors to the solid solution strengthening and their contribution is ~ 2500 MPa/at% in commercially pure NiAl relative to high purity NiAl. The increase in yield stress resulting from alloying element additions has been extensively dealt by several researchers [6, 7] in the past and will not be discussed here.

As noted in the Literature Review (section 2.2), the mechanical properties of NiAl at ambient temperature are strongly influenced by impurity concentration, pre-stress, thermal-history, and the presence of any gettering agent/s. Thermal treatments prior to deformation of commercial purity single crystals impacted the yield-stress determined in this present investigation to similar levels as the fracture-toughness properties measured by Hack et al. [18-20]. For example, the yield-stress was more than doubled by changing the cooling rate from the fast (1 K/s) to the slow (0.1 K/s) rate following a 1600 K homogenization anneal, whereas the fracture-toughness decreases by almost 85% for the same change. Similarly, for the samples reheated at 673 K, the fracture-toughness decreases by 65%, with a concurrent 57% increase in the yield-stress when the cooling condition is changed from fast to slow rate. Figure 12 shows that if the terminal cooling rate is slow, the ductility decreases and the yield stress increases, regardless of prior processing parameters for commercial purity specimens. Conversely, even if a sample is slow-cooled from higher temperature, but then reheated at intermediate temperatures followed by fast cooling, the fracture toughness increases while the yield stress decreases.

There is not much fracture-toughness data available in the literature for high purity single crystals. No work has been reported replicating experimental conditions in line with Hack et al. [18-20] for high purity NiAl single crystals similar to those used in the present work. Johnson et al. [107] reported fracture-toughness values in the range of 10-12 $MPam^{1/2}$ for high purity single crystals. But as the influence of prior thermal treatment on yield properties was not found to be very significant, it may be anticipated that the fracture-toughness properties are not largely impacted by the thermal treatments in high-purity NiAl single crystals.

In case of the post deformation TEM studies, the deformation substructures, like the mechanical properties, of both the high and the commercial purity materials, depended largely on the prior thermal history. Based on the final cooling rate from elevated temperatures the deformation substructure displayed significant differences. Heavily tangled dislocations were observed (figures 18 – 20) after deformation of the slow-cooled commercially pure materials; strong interactions between the pre-existing dislocations and the newly created dislocations facilitate such tangle formation. The isolated dislocations, as shown in figure 21, gliding under beam heating conditions, exhibited limited mobility and ceased movement when they encountered tangled or piled-up dislocations. The dislocation substructures and the restricted mobility of individual dislocations imply removal of a good proportion of dislocations from the pool of mobile dislocations by slow cooling. As a result, during subsequent deformation, larger stresses were required to propagate newly generated dislocations through the forest of entangled and pinned dislocations, giving rise to a higher yield stress and limiting the toughening mechanisms.

Post deformation TEM examination of the fast cooled commercial purity material did not reveal any dislocation tangles (figures 22 – 24) in comparison to the slow cooled material. The pre-existing dislocations were not subjected to pinning in this case, as the cooling rate was sufficient to retain the solutes in solution. As a consequence, during subsequent deformation, freshly generated dislocations encountered fewer obstacles, resulting in lower yield stresses and higher fracture toughnesses. Also, it was observed that the motion of the isolated dislocations by beam heating was not hindered nor restricted in the fast cooled commercially pure material.

In contrast to the commercially pure specimens, mobility of dislocations did not vary between the fast and the slow cooled high purity samples. In both cases <001> type dislocations were found to be mobile as a result of beam heating. In most cases isolated dislocations were observed even after deformation, and the substructures contained few tangles and very poorly defined dislocation cells. Similar to the commercially pure material, some <110> dislocations were also observed in the high purity material, as shown in figure 27 for fast cooled specimens. Dislocation analyses of the slow-cooled high purity material revealed <111> as the mobile dislocations (figure 28) in addition to <001> and <110> dislocations. There is no mention in the literature of <111> dislocations in NiAl other than in <001> oriented single crystals. The mobility of these <111> dislocations will be discussed in the *in-situ* deformation studies section.

## 5.2 Static Strain Aging

The observed differences in dislocation morphology and mechanical behaviors and their correlation are best explained in relation to strain aging. Strain aging is a time dependent strengthening phenomenon where a plastically deformed metal or alloy hardens as a result of elastic interaction of solute atoms with the strain fields of dislocations. Thus, any alloy system in which interstitial or substitutional atoms are able to pin the active dislocations and their sources is susceptible to strain aging; low carbon steel is the most studied and ideal example of this phenomenon [109]. Depending on the way (prior to or during plastic deformation) the solute atom atmosphere forms around the dislocations, strain aging may be classified into two distinct types, static and dynamic. Dynamic strain aging, which becomes more significant when diffusing solute atoms

interact with mobile dislocations, will be discussed at greater length in section 5.4 with *in-situ* deformation results.

Static strain aging (SSA) is associated with the return of a sharp yield-point, increase in yield-stress, and decrease in ductility. Generally, pre-straining, unloading, aging, and reloading at the same rate of the pre-strain precede SSA. Several theories explaining the mechanisms of SSA in BCC metals and alloys have been discussed at length in the literature [108, 109]; they will be summarized here in view of the similarities between the BCC crystal structure and the B2 system.

There are four different processes that describe SSA, namely, the Snoek effect, formation of the Cottrell atmosphere, Suzuki locking, and precipitate formation. Suzuki locking and precipitate formation are not pertinent to the discussion of the present investigation. Suzuki locking originates from the chemical interaction between stacking faults and solute atoms. Suzuki locking is prevalent in metals and alloys with wide stacking fault widths and low stacking fault energies, such as FCC or HCP systems. It is unlikely that Suzuki locking is a possible mechanism of SSA in NiAl, which has no evidence of any stacking faults and is a high stacking fault energy system. Precipitate formation is expected in any alloy system supersaturated with solute atoms. Precipitation on dislocations during aging results in pinning and gives rise to strengthening, although overaging causes coalescence of the precipitates to take place by Oswald ripening and induces softening. Since no gettering elements are used and no precipitates of any second phase have been observed in the present investigation, precipitation can be ruled out as the mechanism of SSA in this investigation.

The Snoek effect involves the strain-induced ordering of interstitial atoms around dislocations when the interstitial atoms (typically occupying the octahedral sites at the center of the cube edge or cube face) jump from one position to another in the lattice [110-111]. Application of any external stress along one direction of the unit cell results in enlargement of the interstitial sites along that axis and an associated decrease in the size of the openings perpendicular to that particular axis of elongation. Thus, the atoms, which have no favorable site occupancy in an otherwise strain-free lattice, are forced to move/jump to new positions in the slightly deformed and tetragonal lattice. This type of strain induced ordering gives rise to interaction between dislocations and solute atoms, resulting in an increase in yield stress.

The Cottrell atmosphere [112] is a solute environment around dislocations that forms during static strain aging and grows depending on the time and temperature of the aging process. The solute atmosphere is formed by elastic interaction between interstitial atoms and the strain fields of dislocations. In fact, this elastic interaction is the driving force for diffusion of solute atoms to the strain-fields of dislocations and results in decreasing total energy of the system. Thus, the dislocations are locked by solute atoms requiring additional stress to move them. Cottrell atmosphere formation increases the yield stress by a higher magnitude than the Snoek effect [113].

Impurities, such as carbon and silicon, play an important role in controlling the strain-aging response of Ni-Al alloys. It was observed by Weaver et al. [85] that the strain aging effect of carbon is more pronounced in presence of silicon than without it. Weaver [80] carried out a systematic study of several different polycrystalline NiAl alloys to find out the species responsible for strain aging. This study found carbon to be

the primary element responsible for strain aging rather than nitrogen or oxygen. This strain aging response was illustrated by development of yield-point phenomenon as carbon doping was increased in high purity NiAl alloys. Noebe and Garg [114] made a similar observation using powder processed NiAl. They found no sharp change in the yielding pattern in the stress-strain curves of a nitrogen-doped alloy (904 ppm N, 347 ppm O and 57 ppm C) as opposed to a sharp change in the yield stress and load drop for a carbon-enriched alloy (143 ppm C, 6 ppm N and 227 ppm O). Interestingly, high purity alloys aged for longer times exhibited serrations in the stress-strain curves [81, 83], which were presumably a result of the lower concentration of interstitials requiring longer diffusion distances to effect pinning of dislocations.

The commercial purity material used in this present study is also enriched with carbon (Table II), and in the presence of silicon a strong strain aging response is expected [85]. The presence of silicon could not be avoided in the commercial purity materials as silicon gets picked up by the growing single crystals from the alumina-silicate shell molds in the Bridgeman process. The increase in yield stress associated with slow cooling is consistent with all earlier findings, including those of Hack et al. [18-20]. Presumably the mechanisms responsible for strain aging are both the Snoek effect and the Cottrell atmosphere, as the other two SSA mechanisms are ruled out in the present case. As the Snoek effect is not associated with long-range diffusion and gets completed within the time interval of one atomic jump of the species responsible for pinning, it is expected that the Snoek effect precedes the Cottrell atmosphere formation. It has been reported that two plateaus are observed in a plot of increase in yield stress as a function of aging time [113]. These plateaus are consistent with a combination of Snoek effect and Cottrell

atmosphere formation. Weaver [80] observed that the time required for one interstitial atom to make one jump corresponds to the first inflection point between the two stages of the above-mentioned plot.

In contrast to slow cooling, fast cooling trapped the interstitial elements in solution and the solute atoms did not have ample time to come out of the solution to interact with the dislocations. That is, there was very little Cottrell atmosphere formation during fast cooling, resulting in lower yield stresses in these samples. This observation is also in conformance with the findings of Hack et al. [18-20] who found that it is possible to minimize the effect of strain aging by faster cooling. It should be noted that if the cooling rate is so rapid that vacancies are entrapped, the yield stress could increase, resulting in additional resistance to dislocation motion [38]. It is important to realize that the vacancy hardening effect acts in addition to the solid solution hardening effect. However, the fast cooling rate applied in the present study is much lower than the cooling rate of quenching necessary for vacancy entrapment. In some cases a few faceted voids are observed in the substructure [33]. These voids are more common in the quenched materials. During subsequent reheating of the quenched specimens, entrapped supersaturated vacancies can coalescence with each other to form these voids and result in decreasing yield stress and lower work hardening rates [7]. (Examples of such void formation in the present study are shown in figures 62, 64 and 69.) As the cooling rate increases, the degree with which solute atoms interact with the dislocations decreases, which most likely is the cause of the decrease in yield stress for faster cooled materials.

As mentioned earlier, the response of the high purity material to static strain aging was quite different from the commercially pure material. This difference in response, as

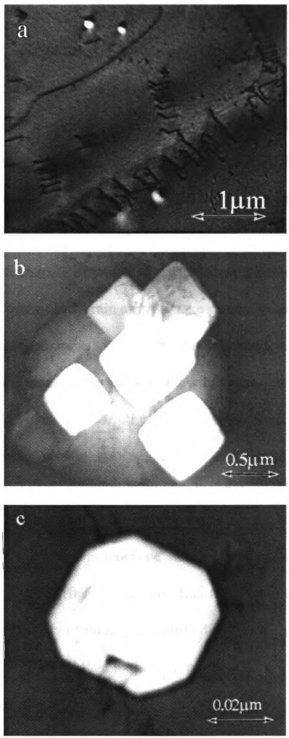


Figure 69. Voids observed in the substructure of high purity [110] oriented material reheated to 673 K following homogenization anneal of 1600 K. Three different samples of the same material revealing isolated and cluster of voids at different magnifications.

measured by the mechanical behavior, was reflected in the resulting dislocation substructures. The high purity material was less susceptible to strain aging primarily due to less intense interaction of the solute atoms with the pre-existing dislocations that stems from a lack of ample solute atoms to provide pinning. This weak interaction is also the root cause for the lower yield stress in high purity materials. As the concentration of solute atoms was low in the high purity material, more time and longer diffusion distances were required to pin the existing dislocations to cause strain aging.

It has been discussed that solute segregation to dislocation cores is one of the mechanisms for strain aging. For strain aging to take place, the local solute concentration 'c' at the core of the dislocation has to be higher than the bulk solute concentration '$c_0$' of the crystal and the two concentrations are related by the following equation [115]:

$$c = c_0 \exp\left(\frac{-W_m}{RT}\right) \qquad (1)$$

where $W_m$ is the dislocation solute binding energy, R is the universal gas constant, and T is the temperature. Therefore, for a constant temperature, the solute enrichment at the core of a dislocation is directly proportional to the bulk solute concentration or $c_0$. According to Fick's Law of Diffusion, the mass flux is proportional to the concentration gradient. Thus, the probability of pinning a mobile dislocation by solute atoms is higher in the commercially pure material than in the high purity material.

Some effect of strain aging is still observed in the high purity material as evidenced by the fact that when these specimens were heated to an intermediate temperature of 673 K and slow cooled, the yield stress increased in comparison to the fast cooled samples (Table IV). In such situations the slower cooling rate provided sufficient time for the diffusing atoms, particularly carbon, to travel longer distances and

lock some of the pre-existing dislocations. However, the availability of solute atoms is inadequate to pin a good proportion of pre-existing dislocations in the high purity material at the cooling rate provided by the slow cooling used in the current investigation.

Thus, the solute atom concentration and the cooling rate complement each other to provide the static strain aging effect. The underlying mechanism of strengthening is the same in both purity alloys; only the degree of hardening differed due to the lesser availability of impurity atoms to interact with the pre-existing dislocations in the high purity material. Hence, the difference in mechanical behavior between the commercial and high purity materials stems directly from the difference in the concentration of the impurities.

In a related study on dislocation structures of NiAl single crystals, B-C. Ng [104] found that the influence of cooling rate on mechanical properties could also be explained with the help of electron channeling contrast imaging (ECCI). He observed fewer dislocations ahead of crack tips in slow-cooled materials and suggested that solute pinning made it difficult to generate or emit fresh dislocations at the crack tip. Generation of fewer dislocations at the crack-tip resulted in a smaller plastic zone, and effective crack-tip blunting could not occur. Instead, cracks continued to propagate in a brittle manner, resulting in failure. In contrast to slow cooled commercially pure NiAl, Ng et al. [116] have observed large numbers of dislocations ahead of crack-tips in fast cooled samples, resulting in more ductility in the fast cooled material. For high purity NiAl, ready emission of dislocations from crack-tips was observed for both slow and fast cooling rates [117]. Thus, size of the plastic zone was not a function of the cooling rate for high purity NiAl single crystals as opposed to commercially pure material.

All of these observations lead to an understanding of the higher ductility in the high purity NiAl single crystals. Levit et al. [26] reported elongations as high as 25% in high purity materials. This extensive straining was facilitated by predominantly <001> dislocations. However, in the present study, which used similar purity material, <111> dislocations are observed in addition to <001> and <110> dislocations. This may make the slip process easier, which in turn may increase the ductility in high purity materials. Strain aging was not so pronounced in the high purity material, even after reheating to intermediate temperatures. Although in this study the material was not deformed to failure and the tensile ductility was not determined, considering the source of the single crystals and their impurity concentrations, the high purity NiAl alloys would be expected to have a higher ductility than the commercially pure NiAl alloys.

### 5.3 *In-situ* Straining TEM and Dislocation Behavior

As a consequence of tensile strain, new dislocations were generated both at the foil edges and in the foil interiors (in areas too thick to image) in the specimens. These freshly generated dislocations moved irrespective of thermal treatment, orientation, and alloy purity in all specimens tested *in-situ* in the current investigation. Even though NiAl is plagued with low room temperature ductility, dislocation multiplication took place in all cases. Significant differences in the dislocation velocities and manner of movement were observed between the high and the commercial purity materials. The observed differences in dislocation behaviors were presented in the results section (4.5). Some of these differences in the dislocation behaviors of the materials were heavily dependent on the alloy purity and will be discussed at a greater length.

Prior to deformation, the high purity (HP) specimens contained a lower dislocation density than the commercially pure (CP) specimens. Planar arrays of pre-existing dislocations, like those shown in figures 16 and 47, were observed in many parts of the foils and remained sessile throughout the straining process even after the passage of cracks physically divided the foil (figure 31). These dislocations, lying in the plane of the foil, were sessile due to their orientation with respect to the load-axis and plane of the foil, which implies that the pre-existing dislocations, being in orientations disadvantageous for slip in the *in-situ* studies, had resolved shear stresses equal or close to zero and could not move. Sometimes dislocations lying in the plane of the foil (such as figure 50) moved very rapidly in the high purity material. Such observations are considered to be special cases. There are two conditions that may have resulted in movement of such dislocations with apparent zero Schmid factor (if their glide plane is the same as the foil or parallel to the loading axis). First, the rotation of the tensile axis during straining, or second, high localized residual stresses developed around the dislocations as a result of tensile deformation of the thin-foil specimens. Regardless, movement of dislocations lying in the plane of the foil is considered an exception, and in general such dislocations did not show any activity/mobility throughout the *in-situ* straining process.

Because of the thin foil sample geometry, the magnitude of the localized residual stress in the thin-foil was not constant. As a result, the resolved shear stress on all the mobile dislocations was not uniform and dislocation movement rate was different at different parts of the foil. Figure 51 shows such an example, where one of the mobile dislocations cross-slipped past its neighbors on its way to the foil edge. Other

dislocations generated from similar sources took longer times to exit the field of view as well as the sample edge. Non-uniform distributions of the pre-existing dislocations and variation of the foil-thickness at different areas are thought to be responsible for such behaviors. In other words, in a typical thin foil all the edges of the foil are not equally effective in generating dislocations. Thus, due to the complex state of stress in the thin foils, the observed dislocation motion unfortunately could not be related to the macroscopic stress and strain.

The most significant observation in the high purity material was the velocity of the dislocations at which they moved during *in-situ* straining. In fact, the rate was always an order of magnitude higher in the high purity material than the commercial purity material. In the high purity material, dislocations primarily moved by rapid jumps, regardless of whether the movement initiated from the foil-edge or from the inner part of the foil. Cross-slip was evident in almost all cases of dislocation motion in the high purity NiAl, making it easier for the deformation process to take place by gliding screw dislocations. In some cases the rapid jumps of the dislocations were nearly instantaneous with the application of strain that following the motion of individual dislocations was difficult.

Sometimes dislocations were seen to move with a burst phenomenon in the high puriy material (figure 55), with the mobile dislocations escaping the field of view and gliding through all pre-existing dislocations lying in the plane of the foil. This illustrates that pre-existing dislocations were not able to inhibit the slip of mobile dislocations to any significant degree. In all such cases cross-slip and movement of dislocations took place in less than a second. As the probability of cross-slip is proportional to the

dislocation length in screw orientations, it may be a fair approximation that all of the rapidly moving dislocations were screw-type, and the activation energy of such cross-slip was very low.

With continued straining, significant levels of tangles developed in the slip bands in the high purity material. Unlike in the commercial purity material, these tangles did not inhibit movement of the mobile dislocations (figure 58). Thus, the entangled dislocations that formed in the high purity material may not be totally pinned. However, in contrast to the observation of Nagpal et al. [101], no well-defined cell structure development was observed in the current study. The reason may be that continued mobility and rapid cross-slip of dislocations through the pile-ups prevented formation of dislocation cells. Also, as the dislocation tangles continued to develop, dislocation multiplication by operation of single ended Frank-Reed sources was observed in the slip bands. Thus, dislocation mobility never ceased in the high purity material with straining.

Although the commercial purity material exhibited sharp differences in the bulk mechanical properties based on the final cooling rate, no significant difference was observed in the dislocation behavior during *in-situ* straining. It was discussed that the morphology and substructure of the pre-existing dislocations influenced the mobility of the newly generated dislocations. Heavily tangled pre-existing dislocations observed in many parts of the foil did not show any activity during the tensile deformation. These tangles are the product of previously explained static strain aging and hindered the dislocation mobility in the commercially pure materials. In general, dislocations associated with pile-ups were found to move at slower rates; mobile dislocations generated either from the foil edge or from the foil interior often ceased to move when

interacting with these dislocations tangles. While the pre-existing dislocation tangles inhibited the movement of mobile dislocations in commercially pure materials, they did not stop it completely. One such example is shown in figure 37 for a slow-cooled [001] oriented commercially pure specimen. Heavily tangled pre-existing dislocations were observed in many parts of the foil prior to straining. With straining, the mobile dislocations, which were confined in narrow slip bands, were able to channel through such tangles. Once the slip band was established through the tangles, newly generated dislocations migrated with relative ease through the pre-existing dislocations. Similarly, dislocation multiplication was observed in slow-cooled commercially pure NiAl alloys (figure 40) by operation of single-ended Frank-Reed sources. Therefore, the brittleness exhibited by the commercially pure alloys may not be related to the inability to generate additional dislocations through multiplication.

Slip in the commercial purity material was mostly planar and confined to narrow slip bands. There was some build-up of loop debris in the slip bands after extensive straining. Cross-slip was observed in limited cases. With continued straining it was sometimes found that the deformed specimens developed cracks from the foil edge, propagating between slip bands (figure 33 d). This sort of crack generation between slip bands is a specific example; in general cracks generated in slip bands with continued deformation. The planar slip and eventual cracking are examples of limited plasticity in the commercially pure material, where the dislocations were always seen to move at a fairly constant, slow rate and in a wiggling manner, rather than through quick jumps observed in high purity materials. The slow movement of the dislocations in commercial purity material is consistent with the solute drag of the dynamic strain aging effect.

Sometimes, dislocations appeared to be bowed out from the ends at the foil surface (see figure 41). The long line lengths of the dislocations are divided into several segments bowed out to a degree in the direction of motion. The radius of curvature of these bowed out segments, R is inversely proportional to the applied shear stress, $\tau$. The pinning is associated with the surface drag-stress or traction produced by the frictional resistance of the oxide layer, which in turn influences the line tension, t, of the dislocation. For a bowed-out segment this line tension creates a restoring force, which acts on the dislocation to straighten the length. The line tension can be approximated [118] as:

$$t = \frac{Gb^2}{2} \tag{2}$$

where G is the shear modulus and has a value of approximately 70 GPa for NiAl single crystals [6, 7] and **b** is the magnitude of the Burgers vector. Based on a lattice parameter of 0.2887 nm for NiAl, the line tension of a [110] dislocation is 2.9 nano Pa. Vailhe et al. [119] computed the detailed shapes of such curved/arched dislocations and calculated the local shear stress in NiAl by using the following relationship between line tension, local radius of curvature and shear stress:

$$R = \frac{t}{b\tau} \tag{3}$$

Combining equations 9 and 10, line tension independent local shear stress can be obtained:

$$\tau = \frac{Gb}{2R} \tag{4}$$

In the present study, the radii of curvature of the bowed-out dislocations were approximated between 0.15 to 0.2 $\mu$m. It should be noted that the bowed out segments,

which are in the form of ogival arches, are more elliptical than circular. In order to measure the radius of curvatures, the dislocations were conceived to bow out from the pinning points and the distances between the pinning points are measured as the diameter of the curvature. The distance was measured in two ways. First, calibrating a known distance on the micrograph such as the magnification marker using the Scion Program [120]. Second, the curvatures were fitted to any known geometric shape such as a circle or an ellipse. Then the included angle, $\theta$, from the two pinning points was measured at the center as shown in figure 70. The diameter of curvature, l, was calculated by the following equation:

$$l = 2r \sin(\theta/2) \tag{5}$$

where, r is the radius of the fitted circle or the average of the major and minor axis if the shape of the curve is elliptical. The local shear stress of such bowed [110] dislocations were calculated using equation 4 and found to be 67 MPa and 50 MPa for l-values 0.15 μm and 0.2 μm respectively. Equation 3 also implies that the smaller the applied shear stress, the larger the radius of curvature of the dislocations with other factors remaining constant. The calculated values of shear stress fall close to the critical resolved shear-stress values (45 – 60 MPa) measured by Vailhe et al. [119] in NiAl single crystals. These values are in close conformance with the macroscopic critical resolved shear stress (63.6 MPa for {110}<111> slip system and 67.5 MPa for {110}<111> slip system) for slow cooled hard oriented HP single crystals. It may be noted that the macroscopic critical resolved shear stress values were calculated using the Schmidt's Law [118]:

$$\tau = \frac{P}{A}\cos\lambda\cos\phi \tag{6}$$

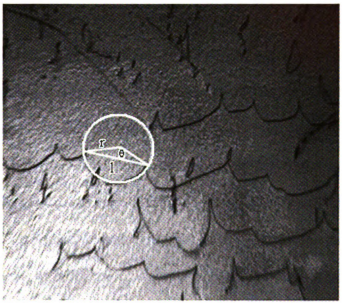


Figure 70. An illustration of measuring the radius of curvature for bowed-out dislocations in figure 53 (a) using the Scion program [120].

where P is the applied load acting on a cross section of area A and $\lambda$ and $\phi$ are the angles of the slip plane and slip direction with the tensile axis.

Dipole formation occurred in NiAl alloys by interaction of cross slipping screw dislocations on different planes. Vailhe et al. [119] described such formation at successive steps. According to their model, when a gliding dislocation interacts with small obstacles, the dislocation is divided into two parts and starts gliding on two parallel slip planes. Thus, a dipole is formed which closes up when the two parallel slip surfaces interact with each other to release the dislocation.

The presence of loop debris impeded further dislocation movement, but many new dislocations were generated when the dislocations broke free from the obstacles (figure 45). Figure 53 b shows several loops that have been left behind by the mobile dislocations at their point of interaction, as shown in figure 53 a. Figure 71 shows such loops at different stages of formation in slow cooled high purity [001] oriented NiAl. Figure 71 a shows how two curved dislocations separated by a jog starts forming a loop, while figure 71 b shows pinched-off loops and formation of others in progression as a result of interaction between bowed out segments of dislocations. Shi et al. [121] proposed a model for dipole and loop formation in NiAl that is schematically shown in figure 72. This model is consistent with the current study.

The dislocation multiplication process and loop and debri formation in the high purity material can be explained based on the model of Koehler [122]. According to the model, screw dislocations cross-slip from the primary glide plane to a second plane, but eventually cross-slip back to a plane that is parallel to the primary plane. Depending on the excursion distance between the primary glide planes, trailing dipoles or pinning

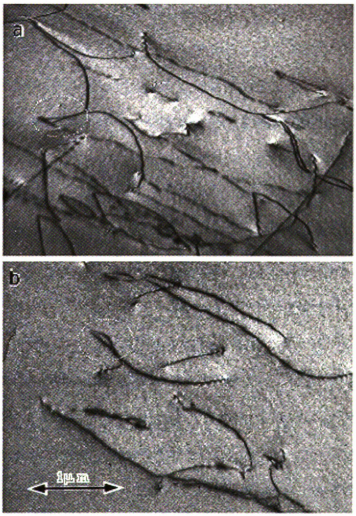


Figure 71. Loop formation at its different stages in high purity slow-cooled [001] oriented NiAl. Figure (a) shows dislocations separated by jogs are coming close together to start forming loops and figure (b) shows progression and finally pinched off loops.

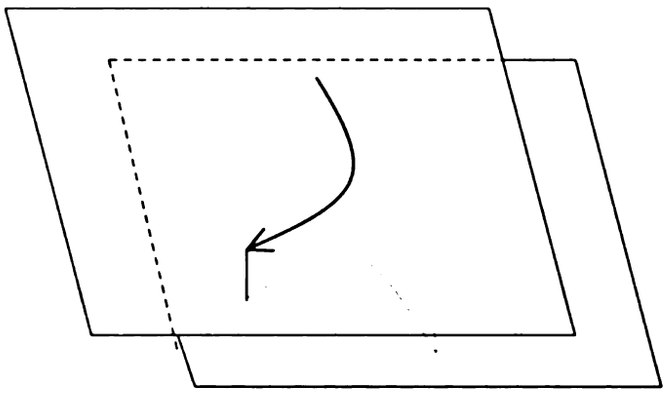

(a) Bowing out of screw segments separated by a jog.

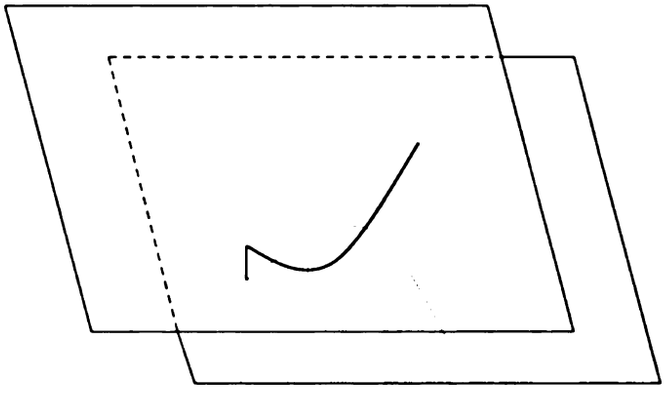

(b) Formation of a dipole

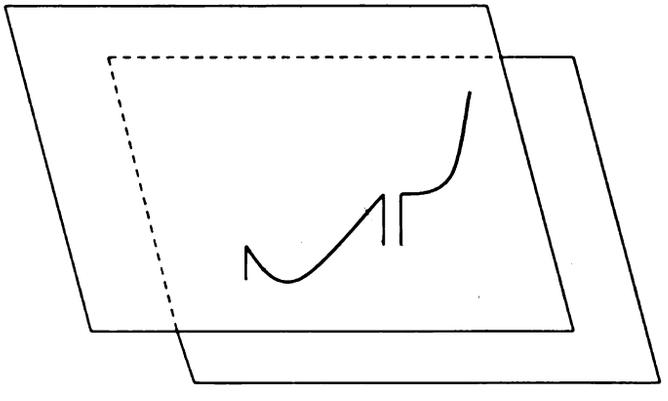

(c) Pinching-off of a loop

Figure 72. Schematic view of loop and dipole formation after Shi et al. [121].

points result, which can act as Frank-Read source [123]. Koehler also described that multiple cross glide is possible as a consequence of collisions of moving screw dislocations [122]. In such a situation, the velocity vector, v, and the jogs created on the secondary plane both lie perpendiculars to the Burgers vector, **b**, of the dislocation. These jogs are essentially edge dislocations, which cannot move out of the secondary glide plane. The edge dislocations can form a dipole depending on the separation distance between the primary glide planes and the applied stress. Therefore, dislocation multiplication by cross-glide and dipole formation are not mutually exclusive events, instead can occur simultaneously.

The dislocation behavior observed during *in-situ* straining electron microscopy was found to be independent of the tensile axis of the specimens. The soft oriented commercially pure material behaved similar to the hard oriented material during *in-situ* straining. Like the fast cooled hard oriented samples, limited cross-slip was observed in the slow cooled materials. Also, similar to the slow cooled hard oriented commercially pure material, dislocation multiplication was evident in the soft oriented slow cooled CP material (figure 45). The same situation was observed for the high purity material. The observed dislocation velocities did not differ significantly with tensile axes of the specimens. As mentioned earlier, thin foil conditions and localized rotation of the tensile axes made it difficult to correlate the dislocation behavior with the bulk tensile axis.

## 5.4 Dynamic Strain Aging

The influence of cooling rate in altering the mechanical behavior and dislocation characteristics of the high and the commercial purity NiAl single crystals was explained

before in light of static strain aging. In this section, the dislocation behavior observed during *in-situ* straining will be assessed in relation to dynamic strain aging.

Dynamic strain aging (DSA) is associated with the active formation and migration of the solute environment around mobile dislocations during plastic deformation. Serrations, jerkiness, or other discontinuities found in the stress-strain curves determined in the constant elongation rate compression or tensile tests are indicative of DSA. An initial low mobile dislocation density and a low sensitivity of dislocation velocity to stress are considered to be the two major contributing causes for the appearance of discontinuity in the stress-strain curve [124, 125]. It has been proposed [126, 127] for materials susceptible to dynamic strain aging that the dislocation velocity (V) is related to the applied resolved shear stress ($\tau$) as:

$$V = \tau D^m \tag{7}$$

where D is the diffusivity of the solute and m is the strain hardening exponent. As D and m are constants within reasonable limits, dislocations with low resolved shear stress would exhibit limited mobility. Depending on the strain rate, DSA occurs over a wide temperature range. For constant rate tensile or compression tests, the strain rate ($\dot{\varepsilon}$) consists of two components, elastic ($\dot{\varepsilon}_e$) and plastic ($\dot{\varepsilon}_p$). Weaver [80] described that for a load drop to occur, the plastic strain rate has to exceed the imposed strain rate. It was assumed that the plastic strain rate is governed by the Orwan equation for gliding dislocations:

$$\dot{\varepsilon}_p = \rho_m b V \tag{8}$$

where $\rho_m$ is the mobile dislocation density, **b** is the Burgers vector of the dislocation, and V is the dislocation velocity. A sudden increase in $\rho_m$, V, or both can result in serrations or a decrease in stress in the stress-strain curves. Repeated locking and unlocking of dislocations will increase $\rho_m$ instantaneously. If the solute atoms repetitively diffuse to dislocations to form dynamic solute atmospheres, serrations occur on stress-strain curve.

Thus, Weaver [80] concluded that dynamic strain aging would become enhanced when the drift velocity of the solute atoms in the stress fields of dislocations equals V. In other words, at low temperatures and high strain rates, dynamic strain aging becomes insignificant as the dislocation velocity largely exceeds the solute velocity; at elevated temperatures and low strain rates, solute migration rate either exceeds or keep pace with the dislocation velocity, resulting in negligible dynamic strain aging or no serrations. Dynamic strain aging can occur between these extremities.

Like SSA, there are several theories explaining the mechanism of DSA. The Cottrell model [128, 129] predicts that serrated flow takes place when mobile dislocations, moving at less than a critical velocity, drag along the solute environment around them. The critical dislocation velocity, $V_c$, above which dislocations break free from the solute atmosphere, is given as:

$$V_c = 4\frac{D}{l} \tag{9}$$

where D is the diffusivity of the solute and $l$ is the effective radius of the solute atmosphere, which is a function of the solute concentration. The diffusivity, D, is given by:

$$D = D_0 \exp\left(\frac{-Q}{RT}\right) \tag{10}$$

where $D_0$ is the pre-exponential coefficient or frequency factor, Q is the activation energy (varying between 66 to 115 kJ/mol [85, 86] for carbon diffusion in NiAl alloys), and R and T carry their usual meanings.

In order to make comparison between the effective radii of the solute atmospheres in HP and CP alloys, it is important to have an estimate of D for carbon diffusion in NiAl alloys at ambient temperature. Diffusivity was not measured in the current investigation. D was estimated to be $3X10^{-22}$ $cm^2/s$ at 300 K by extrapolating the experimental values determined by Weaver [80] and using Microsoft Excel (figure 73). No directly measured $D_0$ data was found in the literature and $D_0$ was calculated to be $1X10^{-8}$ $cm^2/s$; the activation energy derived from figure 73 has a value of 78 kJ/mol for C diffusion in NiAl alloys. In comparison, the activation energy for C diffusion in Fe lattice varies between 84 and 142 kJ/mol [130, 131]. Although the activation energy values for interstitial C diffusion in Fe and NiAl lattice are similar, the $D_0$ determined from Weaver's [80] result does not match the order of magnitude for C diffusion in Fe lattice, which has a value between 0.02 and 2.2 $cm^2/s$ [130, 131]. In general, substitutional elements are expected to diffuse slower than the interstitial elements in any lattice by virtue of the higher activation energy associated with substitutional diffusion. For example, a substitutional element like Ni has $D_0$ value of 0.77-4 $cm^2/s$ for diffusion in Fe lattice with activation energy in the range of 240 to 280 kJ/mol [132]. Likewise, $^{63}Ni$ has a $D_0$ value of 4.5 $cm^2/s$ for diffusion in stoichiometric NiAl alloys with activation energy of 307 kJ/mol [90]. Thus $D_0$, like activation energy, is expected to have similar values for interstitial C diffusion in Fe and NiAl lattices. Therefore, the D value for C diffusion in NiAl alloys, based on the $D_0$ data derived from Weaver's [80] result, is off by few orders of magnitude

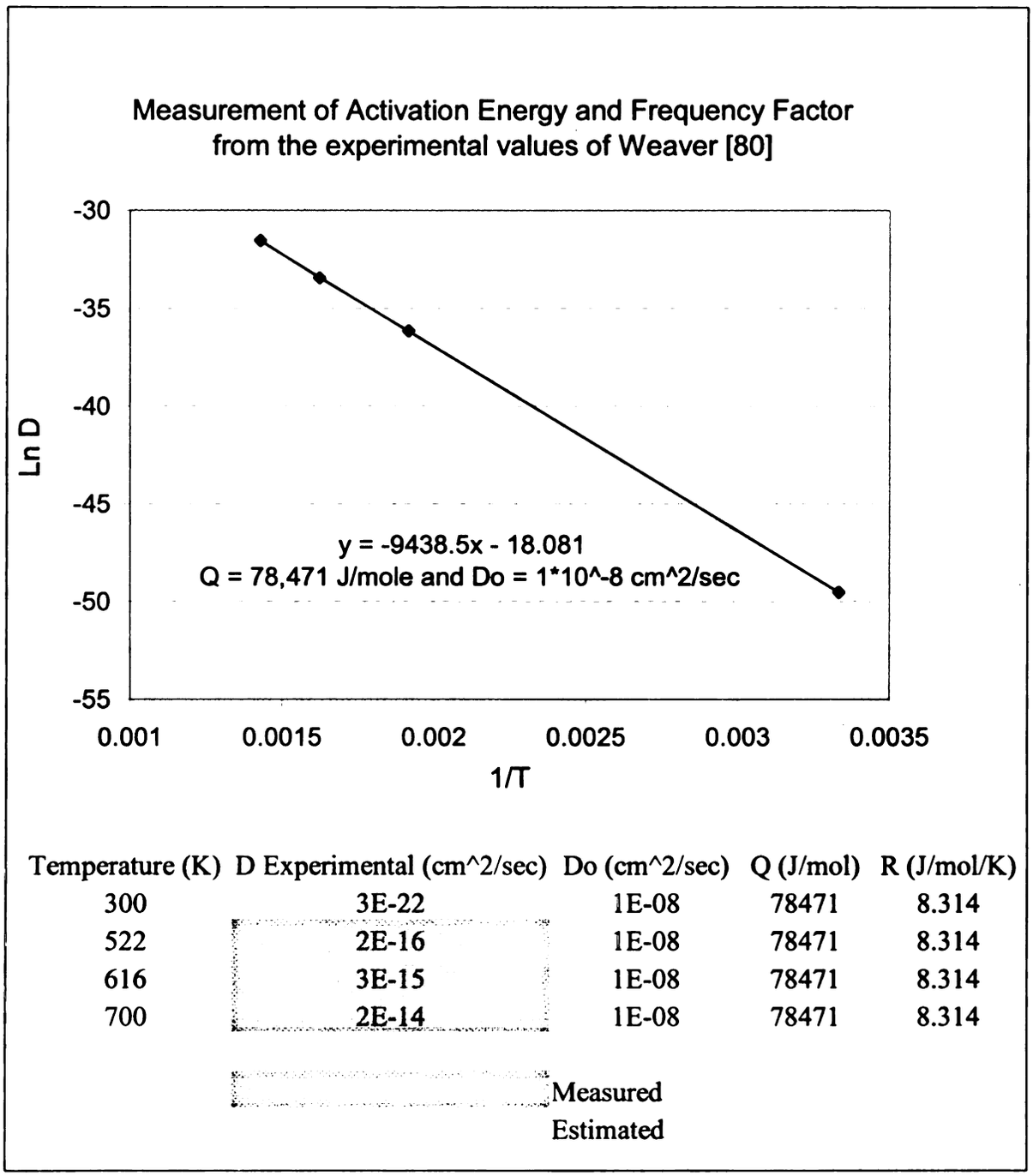


| Temperature (K) | D Experimental (cm^2/sec) | Do (cm^2/sec) | Q (J/mol) | R (J/mol/K) |
|---|---|---|---|---|
| 300 | 3E-22 | 1E-08 | 78471 | 8.314 |
| 522 | 2E-16 | 1E-08 | 78471 | 8.314 |
| 616 | 3E-15 | 1E-08 | 78471 | 8.314 |
| 700 | 2E-14 | 1E-08 | 78471 | 8.314 |

Figure 73. Plot of diffusivity with temperature after Weaver [80] and extrapolation of elevated temperature diffusivity values to 300 K. The frequency factor, $D_0$ and the activation energy, Q were calculated from the equation of the straight line obtained using Microsoft Excel.

and the $D_0$ value of $1.4X10^{-8}$ $cm^2/s$ is not consistent with what would be expected for interstitial carbon diffusion in NiAl alloys. Weaver also agreed on such inconsistency in private communication. In spite of the problems in determining the D value, the effective radii, *l* may be qualitatively compared in the two alloys based on the relationship of equation (9).

According to equation (9), the dislocation velocity is inversely proportional to the effective radius of the solute atmosphere. This equation is very important in understanding the difference in dislocation velocities with alloy purity. Above a threshold of $V_c$, the drag stress on the dislocations decreases with an increasing dislocation velocity. As the high purity alloy has a lower global concentration of solute atoms than the commercial purity alloy, the local solute atom concentration at dislocations in the HP alloy will be lower compared to the dislocations in the CP alloy. Therefore, the effective radius of the dynamic solute atmosphere interacting with the dislocations is also smaller in the HP material compared to the CP material. Based on the average measured dislocation velocity for the high and the commercial purity NiAl, there exists an order of magnitude difference between the effective radii of the solute atmospheres.

The observed dislocation motion was not continuous in the present study. McCormick [133, 134] developed a model for DSA based on the assumption of discontinuous dislocation motion and proposed that the interaction of solute atoms with mobile dislocations takes place when the dislocations wait at obstacles. McCormick's model equates the dislocation velocity, v, to the average obstacle spacing, L:

$$v = \frac{L}{t_w + t_f} \tag{11}$$

where $t_w$ is the mean waiting time at an obstacle, and $t_f$ is the mean flight time between obstacles. The dislocation velocity can be simplified in cases when the time of flight, $t_f$, is negligible and v is expressed as:

$$v = \frac{L}{t_w} \text{ or } t_w = \frac{L}{v} \tag{12}$$

With this kind of linear relationship between obstacle spacing and waiting time, it is evident that $t_w$ is higher for the commercial purity material than for the high purity material. For example, with a dislocation velocity of 10 μm/sec and average obstacle spacing of 0.25 μm, $t_w$ becomes 25 milliseconds for the high purity alloys compared to 500 milliseconds for the commercial purity alloys with the same obstacle spacing (figure 45) but a velocity of 0.5 μm/sec. This higher value of $t_w$ in the commercial purity alloys provides more time for the solute atoms to pin the mobile dislocations. The higher probability of pinning mobile dislocations is consistent with the sluggish movement of dislocations in the commercial purity alloys.

According to McCormick, yield serrations will occur when $t_a$, the aging time becomes equal or close to $t_w$. Based on the available models [112, 115], McCormick described $t_a$ as the time required to lock mobile dislocations:

$$t_a = \left\{\frac{C_l}{\alpha C_0}\right\}^{2/3} \left\{\frac{kTb^2}{3DU_m}\right\} \tag{13}$$

where $C_l$ is the critical solute concentration to lock a dislocation, $C_0$ is the bulk solute concentration of the alloy, $U_m$ is the binding energy as defined by $W_m$ in equation (1), D is the diffusivity of the solute, and α is a constant with a value of 3. For the commercially pure material with a higher $C_0$, $t_a$ will be lower if everything else remains unaltered, resulting in enhanced pinning compared to the high purity material. The *in-*

*situ* tensile straining process in the current investigation was intermittent. There was always a pause or momentary stop after each increment of straining to watch and record the dislocation activity. During this time stress relaxation took place and mobile dislocations waiting at any obstacle could be locked. When the aging time exceeds the waiting time ($t_a > t_w$), dislocations waiting at obstacles will not be locked, causing free flow, which is the case for the high purity alloys. Also, it takes a longer aging time to lock the mobile dislocations when the temperature of the process limits the diffusivity of the solutes. The availability of more solute atoms provided a decreased $t_a$ in the commercially pure alloys and consequently DSA resulted in restricted mobility of dislocations.

Manifestation of DSA in the high purity alloys was not evident in the dislocation behavior. As discussed earlier, long-range diffusion is required for dynamic strain aging to be effective in the high purity material. One of the conditions for long-range diffusion to take place is enhanced thermal activation. However, the thermal activation for the DSA process was controlled by the thermal energy of the electron beam heating and strain aging could not take place in a dynamic manner with low solute concentration and slightly elevated temperature. The microscope was always operated at 200 kV and the physical characteristics, including the thickness of the samples, were similar for both purity samples. Therefore, the heating effect, and thus the temperature of the dynamic strain aging process, must be in close conformance for both purity alloys, which implies that the solute concentration played the major role to influence the intensity of the dynamic strain aging.

There were situations (figures 35 and 36) when limited cross-slip of <001> dislocations was observed for the fast cooled CP material, and dislocations were seen to change slip planes between {110} and {001}. The activity of the mobile dislocations was not sluggish during cross-slip as opposed to planar slip. So the intensity of DSA in locking the dislocations in the fast cooled commercial purity alloys was definitely not as strong as in the slow cooled alloys. In the case of cross-slipping dislocations, the pre-existing dislocations were of mixed types; scattered tangles of dislocations were observed along with straight dislocations. As such, the effect of static strain aging was not also pronounced for the fast cooled commercial purity material.

Kocks [135] proposed temporary arrest of mobile dislocations at forest dislocations during dynamic strain aging. The solute atmosphere, which forms on the forest dislocations, drains by pipe diffusion to the mobile dislocations during their waiting. Thus, Kocks assumed that a dislocation may not be locked along its entire length, but instead the solute atoms may lock only the pinned portion of the line-length at forest dislocation junctions. This mechanism may be valid for the commercially pure alloys in the current investigation where the presence of pre-existing tangles and their interaction with mobile dislocations were observed. It was almost always possible to watch and follow the movement of individual dislocation line segments. This segmental movement may be a result of partial locking of mobile dislocation lines where the rate of locking and unlocking is controlled by pipe diffusion of the interstitial solute atoms during *in-situ* straining.

There are other theories of dynamic strain aging based upon the critical strain at the onset of yielding and elevated temperature serrations. Those theories for high

temperature dynamic strain aging are not applicable here because the type of dynamic strain aging witnessed in the current investigation is a low-temperature ($T \cong 0.17\ T_M$) phenomenon.

The difference in mechanical behavior can be further elucidated with consideration of the activation area and its dependence on impurity concentration. Based on the thermodynamic and kinetic model thermally activated dislocation motion developed by Kocks, Argon, and Ashby [136], the apparent activation area, $\Delta a$, is related to the Burgers vector, **b** by:

$$\Delta a = V^*/\mathbf{b} \tag{14}$$

where $\Delta a$ is defined as the area on the slip plane associated with the configuration of a dislocation and $V^*$ is the apparent activation volume, which is related with the applied shear stress ($\tau$), Boltzman's constant (k), shear stain rate ($\dot{\gamma}$) and the temperature of deformation (T) by:

$$V^* = kT(\partial \ln \dot{\gamma} / \partial \tau) \tag{15}$$

Therefore, for a constant temperature, the activation volume depends on the change of shear strain rate with shear stress. Kocks et al. [136] also defined the apparent activation volume for dislocation-impurity interaction in a dilute solution as:

$$V^* = \mathbf{b}L\Delta y \tag{16}$$

where, L is areal density of the interstitial atoms on the slip plane, which can be approximated as $\mathbf{b}/\sqrt{c}$. Here, 'c' is the atomic fraction of impurities and $\Delta y$ is the activation distance over which the gliding dislocations interact with interstitial elements. When $\Delta y = \mathbf{b}$, equation (16) can be re-written and the activation volume becomes:

$$V^* = \mathbf{b}^3/\sqrt{c} \qquad (17)$$

Thus, the activation volume becomes a strong function of the impurity concentration of the deforming material. As carbon is the primary element responsible for the strain aging behavior in NiAl, it is also expected to impact the activation volume to the highest extent. Based on the total carbon concentration of the investigated alloys (Table II), the activation volume of the commercially pure material is around $60\mathbf{b}^3$ as opposed to $176\mathbf{b}^3$ for the high purity material. The values for commercially pure materials are well in conformance with measured ($59 - 60\mathbf{b}^3$) and calculated activation volumes ($55\mathbf{b}^3$) from strain rate change experiments of Kitano et al. [137 and 138]. Kitano and Pollock [138] measured the activation volumes in commercially pure and high purity NiAl single crystals. Table VIII shows the chemistry and the activation volumes calculated for the NiAl single crystals used in the current study in comparison with those determined by Kitano and Pollock [138]. Interestingly, Kitano and Pollock have used the total impurity (carbon + oxygen + nitrogen + sulfur) concentration in their calculation to determine the activation volumes, although the efficacy of any of these elements other than carbon has been shown to be insignificant [80]. The activation volumes are calculated to be $45\mathbf{b}^3$ and $72\mathbf{b}^3$ respectively for commercial and high purity materials if total impurity levels are considered for the alloys used in the current investigation. For such a calculation, the activation volume is assumed to be impacted in equal proportion by carbon and other elements. However, based on the dramatic differences observed in the dislocation behaviors of high and commercial purity materials in the present study and in previous studies [139, 140] that is not expected to be the case.

Table VIII. Comparison of calculated and measured [138] activation volume for NiAl single crystals

| Material | Measured Activation Vol. ($V^*b^3$) (Ref. 138) | Calculated $V^*b^3$ (Ref. 138) | Calculated Activation Vol. ($V^*b^3$) (Present Study) |
|---|---|---|---|
| CP – NiAl (210 ppm C and 91 ppm O) | 59 and 60 | 55 | |
| CP – NiAl (79 - 272 ppm C and 380 ppm O) | | | 60 |
| HP – NiAl (18 ppm C and 16 - 29 ppm O) | 83 and 90 | 130 | |
| HP – NiAl (32 ppm C and 160 ppm O) | | | 176 |

The disparity between the experimentally measured ($83\mathbf{b}^3$ – $90\mathbf{b}^3$) and the theoretically calculated ($130\mathbf{b}^3$) values of activation volumes for the high purity material needs some review. Two conditions may lead to this difference. There may be a threshold limit of impurity concentration, below which the impurities are not effective in developing efficient barriers to dislocation motions at room temperature. Two, as proposed by Kitano and Pollock, some other intrinsic short-range barriers to dislocation motion, such as a large Peierls stress, may exist [138]. As significant cross-slip is observed during *in-situ* straining of the high purity material [139, 140], dislocation motion may not be restricted by limited mobility of screw dislocations, as is the case for BCC metals. The presence of a large Peierls barrier or requirement of a large shear stress to move dislocations is not consistent with extensive cross-slip.

In spite of the difference in activation volume values, it may be concluded that the flow behavior of the NiAl single crystals studied here was strongly influenced by differences in the activation volumes between the high purity and the commercially pure materials which in turn was dependent on the solute concentrations, regardless of how the activation volume was calculated.

Difference in dislocation behavior between high purity and commercial purity materials may also be addressed from the lack of dislocation multiplication in the commercial purity material by multiple cross glide mechanism. According to Gilman [123], collision of mobile dislocations induces self-excited oscillations that result in multiple cross-glide. One of the pre-condition to have self- excited oscillations is minimum damping, which is a function of crystal purity. The damping coefficient is higher for the commercial purity material than the high purity material and this in turn

influences the drag forces more on the dislocations in the commercial purity material. Also, movement of dislocations during multiple cross-glide processes is always accompanied by collisions with randomly distributed shear-strain fluctuations on primary and secondary planes. This kind of fluctuations has its origin in the difference between the line tensions of the dislocations, which increases with the rate of dislocation multiplication [123]. Therefore, with slow rate of movement in commercially pure materials, dislocation multiplication is also slower that results in decreased plasticity than high purity materials.

Although the bulk mechanical properties varied widely depending on the cooling rate, the dislocation behavior during *in-situ* straining did not reflect the same pattern. The *in-situ* straining seems to be less susceptible to changes in cooling rate or static strain aging. The strain-aging effect observed during *in-situ* deformation involves both static and dynamic strain aging. The SSA takes place during slow cooling from elevated temperatures prior to deformation; the DSA occurs during *in-situ* straining. The probability of strain aging taking place in a dynamic manner at room temperature under constant load might be considered negligible due to the following reasons. There is not enough thermal activation for the solute atoms to form dynamic atmospheres around the dislocations, and it is very difficult for the solute atoms to keep up with the freshly generated dislocations due to limited diffusion at room temperature.

Thus, the only differentiating factor in the extent of strain aging between the two alloys is the intensity by which the pseudo-dynamic solute atmosphere forms around the dislocations or in their vicinity during their migration or waiting at obstacles. Therefore, any impediment to the freshly generated dislocations was a function of the availability of

solute atoms, the waiting time, and their diffusion. Pre-existing dislocation substructures and the extent of their interactions during SSA do not seem to influence the mobile dislocation characteristics, including slip processes, velocities and multiplication.

Mobile dislocation characteristics did not vary with the condition (un-deformed, post-deformed, or *in-situ*) of the specimens. Dislocations generated during *in-situ* studies of tensile specimens were confirmed with 3 mm disc straining. Both pre-existing and mobile dislocations were characterized as <001> type (figure 61, 62, 65). The majority of dislocation characterization studies in NiAl identified <001> as the mobile dislocations, except for the cases when single crystals were oriented to the <001> orientation. Figures 66, 68 and 69 are examples that show <101> mobile dislocations whereas, figures 63, 64 and 67 show <111> mobile dislocations. Mobility of <111> dislocations was found in both post-deformed observation as well as *in-situ* strained specimens. There are several reports of <111> dislocations in hard oriented samples [6, 7], but mobility of <111> dislocations was not mentioned.

Dislocations that were characterized as <111> screw dislocations found to move on {112} planes in slow-cooled soft oriented high purity specimens. These observations are consistent with earlier findings of Veyssiere and Noebe [47] that <111> slip in NiAl occurs on {112} planes. In contrast with the present study however, they found <111>{112} slip in hard oriented samples deformed at room temperature in compression. One of the possible reasons for this difference may be the localized rotation of the tensile axis during thin-foil straining in the present investigation. It may be recalled that the thin area and the hole in a TEM foil create a complex state of stress. Field et al. [40] also suggested activity of <111> dislocation on {112} planes below the DBTT. It is

interesting to note that Morris et al. [102] did generate <111> dislocations in NiAl by hardness indentation but failed to observe any mobility of the same. In hard oriented high purity samples, <110> dislocations were found to be mobile both on {110} and {112} planes and cross-slip was almost always evident. In order for any material to exhibit plastic flow, it is essential that Von Mises criterion is satisfied in polycrystalline condition. Von Mises criterion, which requires a minimum of five independent slip systems, accommodates any arbitrary shape change. Thus, the presence of <111> mobile dislocations has important implications on plastic deformation and mechanical behavior of NiAl alloys.

In spite of having significant dislocation mobility and multiplication, the question remains why NiAl ultimately fails in a brittle manner at room temperature. One of the reasons may be the immobilization of screw dislocations. The screw dislocations were much more mobile than the edge dislocations, and a good proportion of those screw dislocations were eventually immobilized during *in-situ* straining by the development of jogs or zigzag configuration. Brittleness results when such immobilization is not compensated for by generation of fresh dislocations that can overcome the interactions of the existing dislocations [141]. The brittleness of the B2 NiAl alloy systems may also be associated with the inability to relieve the stress concentrations developed during deformations as a result of inadequate number of operative slip systems [142].

# 6.0 CONCLUSIONS

*In-situ* straining in transmission electron microscopy has been used to characterize the dislocation generation and motion in NiAl single crystals. Depending on the impurity concentrations and the imposed cooling rates the behavior of the NiAl single crystals varied. The yield stress values of the NiAl single crystals varied due to the difference in response to the static strain aging, which was a function of the impurity concentrations in the single crystals. The yield stress was inversely related to the final cooling rates from elevated temperatures. For commercially pure material the yield stress increased from 150 MPa to 450 MPa with a decrease in cooling rate from 1 K/sec to 0.1 K/sec. The influence of cooling rate was not so pronounced in the high purity material and the maximum increase was two-fold (from 135 MPa to 274 MPa) when the cooling was decreased from faster to slower rate. The differences in the yield characteristics of the NiAl single crystals were explained by the Cottrell Atmosphere formation.

Deformed slow cooled commercially pure materials showed predominantly tangled dislocations, whereas only a few dislocation tangles were observed in the fast cooled condition, reflecting less intense interaction between dislocations and solute atoms. No discernible difference has been observed between the dislocation behaviors of the high purity specimens depending on the final cooling rate, implying that there may be a critical impurity concentration and/or an extreme slow cooling rate required to impart such changes that were not provided in the current investigation.

Dislocation motion was observed in all of the NiAl samples, regardless of sample purity and thermal treatment. However, no movement of any of the pre-existing

dislocations was observed. The rate of movement of the dislocations varied inversely with the impurity concentration. The range of velocities of dislocations in the high purity material was 4 – 25 μm/sec in contrast to a range of 0.1 – 3 μm/sec for the commercially pure material. Dislocations in the high purity material moved by quick jumps and extensive cross-slip, in contrast to the slow and progressive movement associated with planar slip in the commercially pure material. Cross-slip of screw dislocations was typically followed by the formation of loops and dipole debris. The order of magnitude higher velocity of dislocations in the high purity material indicated less severe strain aging compared to the commercially pure material.

The difference in dislocation mobilities was found to be consistent with different models of dynamic strain aging. The mobile dislocations could not be pinned in the high purity single crystals because of the low concentration of solute atoms. The time required to pin mobile dislocations in the high purity single crystals was higher than the waiting time of the dislocations at different obstacles and thus, no significant dynamic strain aging was observed. The waiting time was ample for the solute atoms to lock the mobile dislocations in the commercially pure single crystals due to higher solute concentrations. The high solute concentration in the commercially pure single crystals resulted in enhanced damping, and dislocation multiplication could not take place at the equivalent rate as in the high purity single crystals.

The cooling rate did not influence the dislocation substructures developed by *in-situ* straining in the commercially pure material. In both slow and fast cooled samples, dislocations were seen to move in a wiggling manner and dislocation multiplications took place by the operation of single-ended Frank-Reed sources. In all cases, both <001> and

<110> dislocations were found to move, confirming that no significant differences were observed in the types of mobile dislocations with cooling rate variation. As the change in cooling rate impacts only the population of the mobile dislocations prior to *in-situ* straining, the characteristics of freshly generated dislocations did not vary significantly.

In addition to <001> and <110> mobile dislocations, mobility of <111> dislocations was observed in both post-deformation studies, as well as during *in-situ* straining of the high purity single crystals. The <111>{110} and <111>{112} slip systems have important implications for polycrystalline deformation, since these satisfy the Von Mises criterion requiring five or more independent slip systems to be able to obtain a general homogeneous strain. Moreover, the frequent mobile dislocation multiplication observed with straining increased the ability to undergo plastic deformation in the high purity single crystals.

No particular difference in mobile dislocation behavior was observed during *in-situ* straining as a result of changing the bulk tensile axes; strict adherence to the bulk tensile axis during deformation was neither possible nor guaranteed due to the thin-foil conditions and localized rotation of the tensile axis.

The computed local shear stress of the curved and bowed-out dislocations (50 – 67 MPa) corresponded well with the theoretical shear stress (45 – 60 MPa) of the NiAl single crystals. Theoretically calculated ($55\mathbf{b}^3$) and experimentally measured ($59\text{-}60\mathbf{b}^3$) values of activation volumes [118] were in close conformance for the commercially pure material ($60\mathbf{b}^3$) in the present investigation. Similar validation could not be obtained for the high purity material.

# APPENDIX

Digital video disk of clippings from *in-situ* TEM Studies

## REFERENCES


1. R. Darolia, Journal of Metals, **43**, 44-49, 1991.

2. High Temperature Ordered Intermetallic Alloys IV, MRS Proceedings, **213**, editors L. A. Johnson, D. P. Pope and J. O. Steigler, 1991.

3. High Temperature Aluminides and Intermetallics, Materials Science and Engineering A, **152-153**, editors S. H. Whang, D. P. Pope and C. T. Liu, 1992.

4. Structural Intermetallics, Proceedings of the First International Symposium, editors R. Darolia, J. J. Lewandowski, C. T. Liu, P. L. Martin, D. B. Miracle and M. V. Nathal, TMS, 1993.

5. High Temperature Ordered Intermetallic Alloys V, MRS Proceedings, **288**, editors I. Baker, R. Darolia, J. D. Whittenberger and M. H. Yoo, 1993.

6. D. B. Miracle, Acta Metallurgica et Materialia, **41** (3), 649-684, 1993.

7. R. D. Noebe, R. R. Bowman and M. V. Nathal, International Materials Reviews, **38**, (4), 193 -232, 1993.

8. M. H. Yoo, S. L. Sass, C. L. Fu, M. J. Mills, D. M. Dimiduk and E. P. George, Acta Metallurgica et Materialia, **41** (4), 987-1002, 1993.

9. High Temperature Ordered Intermetallic Alloys VI, MRS Proceedings, **364**, editors I. Baker, R. D. Noebe, D. S. Schwartz, S. Hanada, and J. A. Horton, 1995.

10. Deformation and Fracture of Ordered Intermetallics III, Proceedings, editors W. O. Soboyejo, T. S. Srivatsan and S. L. Fraser, TMS, 1996.

11. D. P. Pope and R. Darolia, MRS Bulletin, **21** (5), 30-36, May 1996.

12. High Temperature Ordered Intermetallic Alloys VII, MRS Proceedings, **460**, editors C. C. Koch, C. T. Liu, N. S. Stolof, A. Warner, 1997.

13. Structural Intermetallics, Proceedings of the second international symposium, editors R. Darolia, R. Wagner, M. Yamaguchi, C. T. Liu, P. L. Martin, D. B. Miracle and M. V. Nathal, TMS, 1997.

14. G. Bozzolo, C. Amador, J. Ferrante and R. D. Noebe, Scripta Metallurgica et Materialia **33** (12), 1907-1913, 1995.

15. C. T. Liu, and J. A. Horton, Materials Science and Engineering A, **192/193**, 170-178, 1995.

16. B. Zeumer, W. Wunnike-Sanders, G. Sauthoff, Materials Science and Engineering A, **192/193**, 817-823, 1995.

17. D. F. Lahrman, R. D. Field and R. Darolia, High Temperature Ordered Intermetallic Alloys IV, MRS Proceedings, **213**, editors L. A. Johnson, D. P. Pope and J. O. Steigler 603-608, 1991.

18. J. E. Hack, J. M. Brzeski and R. Darolia, Scripta Metallurgica et Materialia **27** (10), 1259-1263, 1992.

19. J. E. Hack, J. M. Brzeski, R. Darolia and R. D. Field, High Temperature Ordered Intermetallic Alloys IV, MRS Proceedings, **288**, editors I. Baker et al., 1197-1202, 1993.

20. J. M. Brzeski, J. E. Hack, R. Darolia and R. D. Field, Materials Science and Engineering A, **170**, 11-18, 1993.

21. R. Darolia, D. Lahrman and R. Field, Scripta Metallurgica et Materialia, **26** (7), 1007-1012, 1992.

22. R. Darolia, D. Lahrman and R. Field, High Temperature Ordered Intermetallic Alloys V, MRS Proceedings, **288**, editors I. Baker, R. Darolia, J. D. Whittenberger and M. H. Yoo, 423-428, 1993.

23. R. W. Margevicius and J. J. Lewandowski, Scripta Metallurgica et Materialia, **25** (9), 2017-2022, 1991.

24. R. W. Margevicius and J. J. Lewandowski, Acta Metallurgica et Materialia, **41** (2), 485-496, 1993.

25. R. W. Margevicius, I. E. Locci and J. J. Lewandowski, Structural Intermetallics, Proccedings of the first international symposium, editors R. Darolia, J. J. Lewandowski, C. T. Liu, P. L. Martin, D. B. Miracle and M. V. Nathal, TMS, 577-584, 1993.

26. V. I. Levit, I. A. Bul, J. Hu and M. J. Kaufman, Scripta Metallurgica et Materialia, **34** (12), 1925-1930, 1996.

27. T. Hughes, E. P. Lautenschlager, J. B. Cohen and J. O. Brittain, Journal of Applied Physics, **42** (10), 3705-3716, 1971.

28. E-T. Henig and H. L. Lukas, Z. Metallkde, **66**, 98-106, 1975.

29. P. Nash, M. F. Singleton and J. L. Murray, "Phase Diagrams of Binary Nickel Alloys", **1**, editor P. Nash, ASM International, Metals Park, Ohio, 1991.

30. H. Jacobi and H. J. Engell, Acta Metallurgica, **19** (3), 701-711, 1971.

31. R. J. Wasilewski, Transactions of the Metallurgical Society of AIME, **236**, 455-457, 1966.

32. R. J. Wasilewski, S. R. Butler and J. E. Hanlon, Transactions of the Metallurgical Society of AIME, **239**, 1357-1364, 1967.

33. A. Parthasarathi and H. L. Fraser, Philosophical Magazine A, **50** (1), 89-100, 1984.

34. P. Nagpal and I. Baker, Metallurgical Transaction, **21**A, 2281-2282, 1990.

35. R. J. Wasilewski, Journal of Phys. Chem. Solids, **29**, 39-49, 1968.

36. G. W. West, Philosophical Magazine A, **9**, 979-991, 1964.

37. X. Ren and R. Otsuka, Philosophical Magazine A, **80**, 467-491, 2000.

38. N. Rusovic and E-T. Henig, Phys. Status Soilidi. A, **57**, 529-540, 1980.

39. H. L. Fraser, M. H. Loretto, R. E. Smallman and R. J. Wasilewski, Philosophical Magazine A, **32**, 873-875, 1975.

40. R. D. Field, D. F. Lahrman, and R. Darolia, High Temperature Ordered Intermetallic Alloys IV, MRS Proceedings, **213**, editors L. A. Johnson, D. P. Pope and J. O. Steigler, 255-260, 1991.

41. C. H. Lloyd and M. H. Loretto, Phys. Status Soilidi. A, **39**, 163-170, 1970.

42. W. J. Yang, F. Lin and R. A. Dodd, Scripta Metallurgica, **12** (3), 237-241, 1978.

43. G. W. Marshall and J. O. Brittain, Metallurgical Transactions, **7**A, 1013-1020, 1976.

44. D. Farkas, R. Pasianot, E. J. Savino and D. B. Miracle, High Temperature Ordered Intermetallic Alloys IV, MRS Proceedings, **213**, editors L. A. Johnson, D. P. Pope and J. O. Steigler, 223-228, 1991.

45. M. H. Loretto and R. J. Wasilewski, Philosophical Magazine A, **23**, 1311-1328, 1971.

46. M. J. Mills and D. B. Miracle, Acta Metallurgica et Materialia, **41** (1), 85-95, 1993.

47. P. Veyssiere and R. Noebe, Philosophical Magazine A, **65** (1), 1-13, 1992.

48. W. J. Yang, R. A. Dodd and P. R. Strutt, Metallurgical Transactions, **3**, 2049-2054, 1972.

49. M. Yamaguchi, D. P. Pope, V. Vitek and Y. Umakoshi, Philosophical Magazine A, **43** (5), 1265-1275, 1981.

50. A. Ball, Philosophical Magazine A, **20**, 113-124, 1969.

51. J. Bevk, R. A. Dodd and P. R. Strutt, Metallurgical Transactions, **4**, 159-166, 1973.

52. A. Ball and R. E. Smallman, Acta Metallurgica, **14**, 1517-1526, 1966.

53. M. H. Yoo, T. Takasugi, S. Hanada and O. Izumi, Materials Transactions JIM, **31** (6), 435-442, 1990.

54. R. T. Pascoe and C. W. A. Newey, Phys. Status Soilidi. A, **29**, 357-366, 1968.

55. R. D. Field, D. F. Lahrman and R. Darolia, Acta Metallurgica et Materialia, **39** (12), 2951-2959, 1991.

56. H. L. Fraser, R. E. Smallman and M. H. Loretto Philosophical Magazine A, **28**, 651-665, 1973.

57. R. R. Bowman, R. D. Noebe, S. V. Raj and I. E. Locci, Metallurgical Transactions, **23**A, 1493-1508, 1992.

58. E. P. Lautenschlager, T. C. Tisone and J. O. Britain, Phys. Status Soilidi. A, 20, 443-450, 1967.

59. D. I. Potter, Materials Science and Engineering A, **5**, 201-209, 1969.

60. M. G. Mendiratta and C. C. Law, Journal of Materials Sciences, **22**, 607-611, 1987.

61. J. T. Kim and R. Gibala, High Temperature Ordered Intermetallic Alloys IV, MRS Proceedings, **213**, editors L. A. Johnson, D. P. Pope and J. O. Steigler, 261-266, 1991.

62. I. Baker, Materials Science and Engineering A, **192/193**, 1-13, 1995.

63. R. D. Field, D. F. Lahrman and R. Darolia, Acta Metallurgica et Materialia, **39** (12), 2961-2969, 1991.

64. R. T. Pascoe and C. W. A. Newey, Metal Science Journal, **2**, 138-143, 1968.

65. K. H. Hahn and K. Vedula, Scripta Metallurgica et Materialia, **23** (1), 7-12, 1989.

66. E. P. George and C. T. Liu, Journal of Materials Research, **5** (4), 754-762, 1990.

67. E. P. Lautenschlager, D. A. Kiewit and J. O. Britain, Transaction of AIME, **233**, 1297-1302, 1965.

68. K. Vedula and J. R. Stephens, High Temperature Ordered Intermetallic Alloys II, MRS Proceedings, **81**, editors N. S. Stolloff, C. C. Koch, C. T. Liu and O. Izumi, 381-391, 1987.

69. A. G. Rozner and R. J. Wasilewski, Journal of Institute of Metals, **213**, 169-175, 1966.

70. R. D. Noebe and R. Gibala, Scripta Metallurgica et Materialia, **20**, 1635-1640, 1986.

71. R. D. Noebe, R. R. Bowman, C. L. Cullers and S. V. Raj, High Temperature Ordered Intermetallic Alloys IV, MRS Proceedings, **213**, editors L. A. Johnson, D. P. Pope and J. O. Steigler, 589-596, 1991.

72. K-M. Chang, R. Darolia and H. A. Lipsitt, High Temperature Ordered Intermetallic Alloys IV, MRS Proceedings, **213**, editors L. A. Johnson, D. P. Pope and J. O. Steigler, 597-602, 1991.

73. M. H. Yoo and C. L. Fu, Scripta Metallurgica et Materialia, **25** (10), 2345-2350, 1991.

74. S. V. Raj, R. D. Noebe, and R. R. Bowman, Scripta Metallurgica et Materialia, **23** (12), 2049-2054, 1989.

75. P. Nagpal, I. Baker, F. Liu and P. R. Munroe, High Temperature Ordered Intermetallic Alloys IV, MRS Proceedings, **213**, editors L. A. Johnson, D. P. Pope and J. O. Steigler, 533-538, 1991.

76. S. Reuss and H. Vehoff, Scripta Metallurgica et Materialia, **24** (6), 1021-1026, 1990.

77. K. S. Kumar, S. K. Mannan and R. K. Viswanadham, Acta Metallurgica et Materialia, **40** (6), 1201-1222, 1992.

78. K-M. Chang, R. Daroilia and H. A. Lipsitt, Acta Metallurgica et Materialia, **40** (10), 2727-2737, 1992.

79. K-M. Chang, R. Daroilia and H. A. Lipsitt, High Temperature Ordered Intermetallic Alloys IV, MRS Proceedings, **213**, editors L. A. Johnson, D. P. Pope and J. O. Steigler, 597-602, 1991.

80. M. L. Weaver, "Investigation of Strain Aging in the Ordered Intermetallic Compound β-NiAl", A Dissertation, University of Florida, Gainesville, FL, 1995.

81. M. L. Weaver, R. D. Noebe, and M. J. Kaufman, Intermetallics, **4**, 593-600, 1996.

82. J. M. Brzeski, J. E. Hack, and R. Darolia, High Temperature Ordered Intermetallic Alloys VI, MRS Proceedings, **364**, editors I. Baker, R. D. Noebe, D. S. Schwartz, S. Hanada, and J. A. Horton, 419-424, 1995.

83. M. L. Weaver, R. D. Noebe, J. J. Lewandowski, B. F. Oliver, and M. J. Kaufman Materials Science and Engineering A, **192/193**, 179-185, 1995.

84. D. Golberg and G. Sauthoff, Intermetallics, **4**, 143-158, 1996.

85. M. L. Weaver, M. J. Kaufman and R. D. Noebe, Metallurgical Transactions, **27**A, 3542-3557, 1996.

86. J. E. Hack, J. M. Brzeski, and R. Darolia, Materials Science and Engineering A, **192/193**, 268-276, 1995.

87. M. L. Weaver, M. J. Kaufman and R. D. Noebe, Scripta Metallurgica et Materialia, **29**, 1113-1118, 1993.

88. P. Wynblatt, Acta Metallurgica, **15**, 1453-1460, 1967.

89. A. Lutze-Birk and H. Jacobi, Scripta Metallurgica, **9**, 761-765, 1975.

90. G. F. Hancock and B. R. McDonnell, Physica Status Solidii, A, **4**, 143-150, 1971.

91. R. S. Polvani, W-S. Tzeng and P. R. Strut, Metallurgical Transactions, **7** A, 33-40, 1976.

92. A. Prakash and M. J. Pool, Journal of Materials Science, **16** (9), 2495-2500, 1981.

93. P. R. Strut, R. S. Polvani, and B. H. Kear, Scripta Metallurgica, **7**, 949-954, 1973.

94. M. Rudy and G. Sauthoff, Materials Science and Engineering, **81**, 525-530, 1986.

95. W. J. Yang and R. A. Dodd, Metal Science Journal, **7**, 41-47, 1973.

96. W. R. Kane Jr., P. R. Strutt and R. A. Dudd, Transaction of AIME, **245**, 1259-1267, 1969.

97. J. Doychak, J. L. Smialek and T. E. Mitchell, Metallurgical Transactions, **20A**, 499-518, 1989.

98. R. Hutchings and M. H. Loretto, Journal of Metal Sciences, **12**, 503-510, 1978.

99. J. Jedlinski and S. Mrowec, Materials Science and Engineering, **87**, 281-287, 1987.

100. I. Baker, P. Nagpal, S. Guha and J. A. Horton, Sixth Japanese International Symposium on Intermetallics, The Japan Institute of Metals, Sendai, 603-607, 1991.

101. P. Nagpal, I. Baker and J. A. Horton, Intermetallics, **2**, 23-29, 1994.

102. M. A. Morris, J-F. Perez and R. Darolia, Philosophical Magazine A, **69** (3), 485-506, 1994.

103. A. K. Head, P. Humble, L. M. Clarebrough, A. J. Morton and C. T. Forwood, Defects in Crystalline Solids, **7**, editors S. Amelinckx, North-Holland Publishing Company, 1973.

104. B-C. Ng, "Examination of Dislocation Structures in B2 Stoichiometric NiAl Alloys using TEM and SEM Techniques", An M. S. Thesis, Michigan State University, 1997.

105. C. S. Barrett, "Structure of Metals", McGraw-Hill, New York, 39, 1943.

106. Duke Elder, "Critical Flicker Frequency and Television or Motion Pictures", C. V. Mosby, **4**, 602, 1968.

107. D. R. Johnson, S. M. Joslin, B. F. Oliver, R. D. Noebe and J. D. Whittenberger, "First International Conference on Processing Materials for Properties, editors H. Henin and T. Oki, TMS, Warrendale, PA, 865-870, 1993.

108. W. C. Leslie, editor Quench and Strain Aging, **5**, MIT Press, Cambridge, MA, 1986.

109. J. D. Baird, Metallurgical Review, **16**, 1-18, 1971.

110. J. Snoek, Physica, **6**, 591-592, 1939.

111. J. Snoek, Physica, **8**, 711-733, 1941.

112. A. H. Cottrell and B. A. Bilby, "Proceedings of the Physical Society of London", **A 62**, 49-62, 1949.

113. H. E. Rosinger, G. B. Craig and W. J. Bratina, Materials Science and Engineering, **5**, 163-169, 1969/70.

114. R. D. Noebe and A. Garg, Scripta Metallurgica et Materialia, **30**, 815-820, 1994.

115. J. Friedel, "Dislocations", Pergamon Press, Oxford, Addison-Wesley Publishing Company Inc., Reading, MA, 1964.

116. B-C. Ng, B. Simkin and M. A. Crimp, Deformation and Fracture of Ordered Intermetallic Materials III, TMS Proceedings, editors W. O. Soboyejo, T. S. Srivatsan and H. L. Fraser, 337-348, 1996.

117. B-C. Ng, B. Ghosh and M. A. Crimp, Interstitial and substitutional solute effects in intermetallics, TMS Proceedings, editors I. Baker, R. D. Noebe and E. P. George, 163-176, 1998.

118. G. E. Dieter, "Mechanical Metallurgy", McGraw Hill, London, 1988.

119. C. Valihe, J. Douin and D. Caillard, High Temperature Ordered Intermetallic Alloys VI, MRS Proceedings, **460**, editors C. C. Koch, C. T. Liu, N. S. Stolof, and A. Warner, 455-460, 1997.

120. Scion Image, http:/www.scioncorp.com, Scion Corporation, Frederick, MD 217001.

121. X. Shi, T. M. Pollock, S. Mahajan and V. S. Arunachalam, High Temperature Ordered Intermetallic Alloys VI, MRS Proceedings **460**, editors C. C. Koch, C. T. Liu, N. S. Stolof, and A. Warner, 493-498, 1997.

122. J. S. Koehler, Physical Review, **86**, 52-59, 1952.

123. J. J. Gilman, Philosophical Magaazine A, **79**, 329-336, 1997.

124. W. G. Johnston, Journal of Applied Physics, **33**, 2716 – 2730, 1962.

125. G. T. Hahn, Acta Metallurgica, **10**, 727 – 738, 1962.

126. W. G. Johnston and J. J. Gilman, Journal of Applied Physics, **30**, 129-147, 1959.

127. W. G. Johnston and J. J. Gilman, Journal of Applied Physics, **31**, 687 –692, 1960.

128. A. H. Cottrell, "Dislocations and Plastic Flow in Crystals", Oxford Press at the Clarenden, London, 1953.

129. A. H. Cottrell, "Vacancies and Other Point Defects in Metals and Alloys", Institute of Metals, London, 1, 1958.

130. P. G. Shewmon, "Diffusion in Solids", TMS, Warrendale, PA, 1989.

131. J. P. Schaffer, A. Saxena, S. D. Antolovich, T. H. Sanders Jr. and S. B. Warner, "The Science and Design of Engineering Materials", WCB McGraw-Hill, Boston, 1999.

132. H. Oikawa, "lattice Self-Diffusion in Solid Iron; A Critical Review", Technical Report, Tohoku University, **46**, 67-77, 1982.

133. P. G. McCormick, Acta Metallurgica, **19**, 463-471, 1971.

134. P. G. McCormick, Acta Metallurgica, **20**, 351-354, 1972.

135. U. F. Kocks, Metallurgical Transaction, **16A**, 2109 – 2129, 1985.

136. U. F. Kocks, A. S. Argon and M. F. Ashby, Thermodynamics and kinetics of slip, Progress in Materials Science, edited by B. Chalmers, J. W. Christian and T. B. Massalski, **19**, 1975.

137. K. Kitano, T. M. Pollock and R. D. Noebe, Scripta Metallurgica et Materialia, **31** (4), 397-402, 1994.

138. K. Kitano and T. M. Pollock, Structural Intermetallics, editors R. Darolia et al., Proceedings of the First International Conference, TMS, 591-599, 1993.

139. B. Ghosh and M. A. Crimp, High Temperature Ordered Intermetallic Alloys VII, MRS Proceedings, **460**, editors C. C. Koch, C. T. Liu, N. S. Stoloff, S. Hanada, and A. Wanner, 467-472, 1997.

140. B. Ghosh and M. A. Crimp, Materials Science and Engineering A **239-240**, 142-149, 1997.

141. X. Shi, S. Mahajan, T. M. Pollock, and V. S. Arunachalam, Philosophical Magazine A, **79**, 1555-1566, 1999.

142. V. I. Levit and M. J. Kaufman, Proceedings of the International Symposium on "Structural Intermetallics", TMS, editors M. V. Nathal, R. Darolia, C. T. Liu, P. L. Martin, D. B. Miracle, R. Wagner, and M. Yamaguchi, 683-690, 1997.